



BELGIAN RESEARCH PROGRAMME ON THE ANTARCTIC  
SCIENTIFIC RESULTS OF PHASE III (1992-1996)

**VOLUME III**

**GLACIOLOGY  
AND  
CLIMATOLOGY**

EDITED BY S. CASCHETTO



BELGIAN RESEARCH PROGRAMME ON THE ANTARCTIC  
SCIENTIFIC RESULTS OF PHASE III (1992-1996)

VOLUME III

**GLACIOLOGY  
AND  
CLIMATOLOGY**

EDITED BY S. CASCHETTO

FEDERAL OFFICE FOR SCIENTIFIC, TECHNICAL AND CULTURAL AFFAIRS

1997

# LEGAL NOTICE

Neither the OSTC nor any person acting on behalf of the Office is responsible for the use which might be made of the following information.

No responsibility is assumed by the Publisher for any injury and/or damage to persons or property as a matter of products liability, negligence or otherwise, or from any use or operation of any methods, products, instructions or ideas contained in the material herein.

No part of this publication may be reproduced, stored in a retrieval system, or transmitted in any form or by any means, electronic, mechanical, photocopying, recording, or otherwise, without the prior written permission of the Publisher.

Additional information on the Belgian Research Programme on the Antarctic is available on Internet  
(<http://www.belspo.be/antar>)

---

D/1997/1191/23

Published by the Federal Office for  
Scientific, Technical and Cultural  
Affairs (OSTC)  
Brussels, Belgium

Cover photograph : J.-L. Tison

**Serial number ANTAR/97/5**

# FOREWORD

This volume presents the scientific results of research projects in the area of Glaciology and Climatology funded under the Third Phase of the Belgian Research Programme on the Antarctic (1992-1996). Achievements of research projects in the other areas of the Programme form the subject of two separate volumes (Volume I : Marine Biogeochemistry and Ecodynamics; Volume II : Part A - Hydrodynamics, Part B - Marine Geophysics)

The Programme, which was initiated by the Belgian Government in 1985, is funded, managed and co-ordinated by the Federal Office for Scientific, Technical and Cultural Affairs (OSTC). The money allocated to the Third Phase was 160 MBEF. Research-work was implemented by means of 3-years projects undertaken by university- or federal scientific institute-based scientists.

All research costs (personnel, equipment, travel, working and overheads) were financed by the OSTC.

Such research effort aimed at contributing to the development of the knowledge required for a science-based conservation and management of the Antarctic environment and to the assessment of the mechanisms through which the Antarctic and the global climate interact. Emphasis was given on a multi-disciplinary approach of the dynamics of the global functioning of Antarctic main natural systems and of their evolution and interactions. Seven research lines were selected under three priority areas :

- ECODYNAMICS OF THE SOUTHERN OCEAN AND INTERACTIONS WITH THE CLIMATE :
  - Biogeochemical fluxes and cycles in the main trophic compartments
  - Modelling the global dynamics of ecosystems
  - Assessment of the role of " new production " in the burial of atmospheric CO<sub>2</sub> by the Southern Ocean
  
- EVOLUTION AND PROTECTION OF MARINE ECOSYSTEMS :
  - Application of predictive ecological models to simulate ecosystem responses to man-made climatic disturbances
  - Study of hydrocarbons spills dispersion
  
- ROLE OF THE ANTARCTIC IN GLOBAL CHANGES :
  - Ocean-Cryosphere-Atmosphere interactions.
  - Sedimentary palaeoenvironment.

Belgium's commitment in scientific research on the Antarctic is currently covered by the Fourth Phase of the Programme (1997-2000). The overall budget of this new phase amounts to 236 MBEF. In addition the OSTC contributes a sum of 20 MBEF to the operational costs of the European Project for Ice Coring in Antarctica (EPICA).



# CONTENTS

## 1

### FORMATION OF THE TERRA NOVA BAY POLYNYA AND CLIMATIC IMPLICATIONS

H. GALLÉE

- ABSTRACT ..... 1
  - INTRODUCTION ..... 2
  - THE MODEL ..... 5
    - The Atmospheric Model ..... 5
    - The polynya model ..... 6
  - ICE BREEZE SIMULATIONS ..... 10
    - Atmospheric Response ..... 11
    - Polynya Response ..... 20
  - SIMULATION OF THE TERRA NOVA BAY POLYNYA ..... 21
    - Polynya Response ..... 22
    - Air-Sea Interactions over Terra Nova Bay ..... 26
  - CONCLUSION ..... 29
- 

## 2

### DYNAMICS OF THE ANTARCTIC ICE SHEET AND ENVIRONMENTAL CHANGE

F. PATTYN, H. DECLEIR and D. WILLAERT

- ABSTRACT ..... 1
  - RESEARCH GOALS ..... 2
    - Understanding ice sheet systems . 3
    - Paleo-reconstruction and modeling ..... 5
  - MATERIALS AND METHODS ..... 7
    - The ice sheet system model (ICE2D) ..... 7
    - Glacier surface velocity from sequential SPOT imagery ..... 15
  - RESULTS ..... 19
    - Data sampling and environmental forcing ..... 19
    - Ice stream dynamics I: basal motion and cyclicity ..... 22
    - Ice stream dynamics II: Shirase Glacier ..... 28
    - Dynamics of the ice sheet in East Dronning Maud Land ..... 34
    - Surface glacier velocities of Gjelbreen ..... 46
  - DISCUSSION ..... 51
    - Ice stream dynamics ..... 51
    - Paleo ice sheet in east Dronning Maud Land ..... 52
  - CONCLUSION ..... 55
  - ACKNOWLEDGEMENTS ..... 56
  - REFERENCES ..... 57
  - APPENDIX ..... 63
    - Deformation model I ..... 63
    - Deformation model II ..... 63
    - Deformation model III ..... 64
-

# 3

## CHEMICAL AND ISOTOPIC COMPOSITION OF ICE FROM ANTARCTIC ICE SHELVES : IMPLICATIONS FOR GLOBAL CHANGE

R. SOUCHEZ, J.-L. TISON and R. LORRAIN

- ABSTRACT ..... 1
- INTRODUCTION ..... 2
- MATERIALS AND METHODS .... 2
- A CASE STUDY OF PROCESSES OCCURRING NEAR A GROUNDING LINE ..... 4
  - Generalities ..... 4
  - $\delta D$ - $\delta^{18}O$  characteristics of basal ice ..... 6
  - Texture-isotope relationships in the marine ice ..... 9
  - Conclusion ..... 15
- A CASE STUDY OF ICE SHELF-OCEAN INTERACTION FOR A SMALL ICE SHELF ..... 15
  - Generalities ..... 15
  - Characteristics of Ross Sea Waters in the Terra Nova Bay area .... 17
  - Sea Water Characteristics in Front of Hell's Gate Ice Shelf ... 18
  - Marine ice characteristics ..... 21
  - Evidence for dilution at the ice-ocean interface ..... 25
  - Behaviour of the K/Mg ratio ... 29
  - "Orbicular" versus "Banded" frazil 37
  - Conclusion ..... 41
- GENERAL CONCLUSION ..... 42
- ACKNOWLEDGEMENTS ..... 43
- REFERENCES ..... 43

---

## Contents of VOLUME I

### **MARINE BIOGEOCHEMISTRY AND ECODYNAMICS**

#### **SPATIAL AND SEASONAL VARIABILITY OF NEW PRODUCTION AND EXPORT PRODUCTION IN THE SOUTHERN OCEAN**

F. DEHAIRS, M. SEMENEH,  
M. ELSKENS and  
L. GOEYENS

---

#### **ECOLOGICAL MODELLING OF THE PLANKTONIC MICROBIAL FOOD-WEB**

Ch. LANCELOT, S. BECQUEVORT,  
P. MENON, S. MATHOT and  
J.-M. DANDOIS

---

#### **ROLE OF THE MEIOBENTHOS IN ANTARCTIC ECOSYSTEMS**

S. VANHOVE, J. WITTOECK,  
M. BEGHYN, D. VAN GANSBEKE,  
A. VAN KENHOVE, A. COOMANS and  
M. VINCX

---

## Contents of VOLUME II

### Part A: **HYDRODYNAMICS**

#### **OIL SPILL MODELLING IN THE WEDDELL SEA**

B. PETIT

---

### Part B: **MARINE GEOPHYSICS**

#### **BELANTOSTRAT BELGIAN CONTRIBUTION TO THE "ANTARCTIC OFFSHORE ACOUSTIC STRATIGRAPHY PROJECT (ANTOSTRAT)"**

M. DE BATIST, P.-J. BART and  
K. VANNESTE

---





**FORMATION OF THE TERRA NOVA BAY  
POLYNYA AND CLIMATIC  
IMPLICATIONS**

H. GALLÉE<sup>1</sup>

UNIVERSITÉ CATHOLIQUE DE LOUVAIN  
INSTITUT D'ASTRONOMIE ET  
DE GÉOPHYSIQUE G. LEMAÎTRE  
Chemin du Cyclotron, 2  
B-1348 Louvain-la-Neuve  
Belgium

<sup>1</sup> Corresponding author E-mail : [gallee@astr.ucl.ac.be](mailto:gallee@astr.ucl.ac.be)



## Contents

<b>1</b>	<b>ABSTRACT</b>	<b>1</b>
<b>2</b>	<b>INTRODUCTION</b>	<b>2</b>
<b>3</b>	<b>THE MODEL</b>	<b>5</b>
3.1	The Atmospheric Model . . . . .	5
3.2	The polynya model . . . . .	6
3.2.1	Frazil ice . . . . .	7
3.2.2	Consolidated ice . . . . .	8
<b>4</b>	<b>ICE BREEZE SIMULATIONS</b>	<b>10</b>
4.1	Atmospheric Response . . . . .	11
4.2	Polynya Response . . . . .	20
<b>5</b>	<b>SIMULATION OF THE TERRA NOVA BAY POLYNYA</b>	<b>21</b>
5.1	Polynya Response . . . . .	22
5.2	Air-Sea Interactions over Terra Nova Bay . . . . .	26
<b>6</b>	<b>CONCLUSION</b>	<b>29</b>



## 1 ABSTRACT

In this paper one presents a preliminary simulation of the Terra Nova Bay polynya by a coupled atmosphere-polynya model. The atmospheric model is a hydrostatic primitive equations model that has been validated previously by a simulation of the strong katabatic winds observed in this area. The polynya model includes a representation of the free drift of frazil ice, and simple sea-ice dynamics and thermodynamics. Two-dimensional and three-dimensional experiments have been performed under polar night conditions. Two-dimensional experiments show that an open (warm) water area influences significantly the atmospheric circulation in the antarctic coastal zone: an additional ice-breeze effect is simulated and is responsible for the strengthening of the katabatic winds near the coast. Because of the important temperature difference (up to 40°C) between the continental air and the ice-free ocean, strong heat fluxes from the polynya surface are simulated. Finally a three-dimensional experiment has been performed including Terra Nova Bay. The polynya observed in this region is well reproduced. It is found that heat losses from the polynya surface are stronger than previously estimated but are probably constrained by the idealized representation of frazil ice, which is assumed to be uniform in each grid box. This stresses the need for having a better knowledge of frazil ice evolution in large polynyas.

A consequence of the strong heat losses from antarctic coastal polynyas like that of Terra Nova Bay is that they have an impact on the energy and momentum budgets of the atmosphere around Antarctica and influence subsequently the atmospheric general circulation and the Earth's climate. Another consequence of the strong heat release from the ocean in antarctic coastal polynyas is an enhanced sea-ice formation and a subsequent salt rejection in the water column. For example, sea-ice formation in the Terra Nova Bay polynya could contribute to roughly 10% of the total sea-ice formation in the region of the Ross Sea continental shelf. Rejected salt could contribute to the formation of coastal dense water and ultimately to the formation of the antarctic bottom water.

## 2 INTRODUCTION

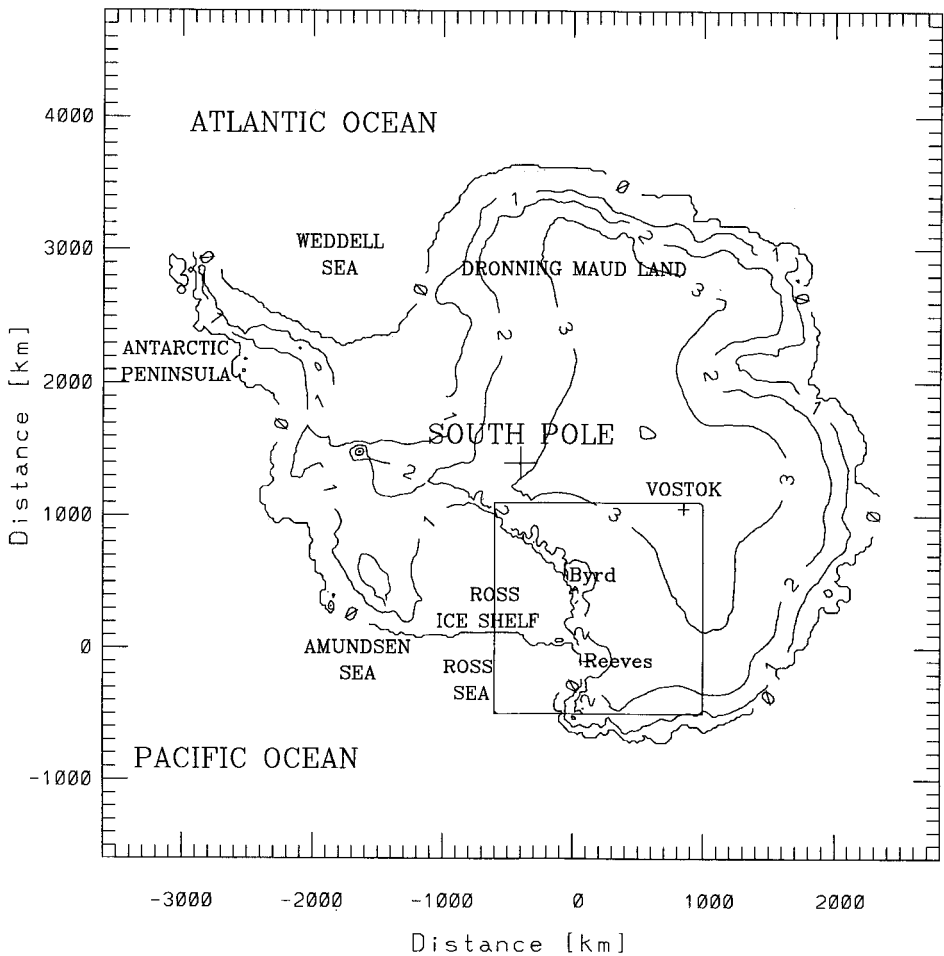
The aim of the present paper is to present a preliminary simulation of the Terra Nova Bay polynya made by a coupled mesoscale atmosphere–polynya model.

From a meteorological point of view, antarctic coastal polynyas influence significantly air–sea interactions in high southern latitudes, especially during winter. This is not so because large areas of open water are involved but rather because strong heat exchange occurs between the ocean and the atmosphere there, in conjunction with strong winds and a large air–sea temperature difference during winter. Indeed antarctic coastal polynyas are generally wind-driven polynyas which form when cold winds blow from the continent.

During the antarctic winter, the intense surface radiative cooling over the ice-sheet slopes is responsible for a temperature inversion in the lowest atmospheric layers. The resulting negative buoyant force generates strong katabatic winds. In addition the cold katabatic air could be drained by terrain confluence zones from large catchment areas through a restricted section of the coastline (Parish, 1988). Consequently the negative buoyant force intensifies, further accelerating the katabatic winds. Another consequence of such drainage is the limited section of these airflows, allowing katabatic air to spread laterally after reaching the coastline. This attenuates markedly the piling up of katabatic air over the ocean and the subsequent slowing down of the katabatic wind there (Gallée *et al.*, 1995b). The resulting airstream may then propagate for long distances over the ocean and may be sufficiently strong to advect sea ice out of the coastal zone. In fact a seaward wind component exceeding  $10 \text{ m s}^{-1}$  is sufficient to maintain a polynya in the coastal zone (Pease, 1987).

An example of the abovementioned katabatic regime is that frequently observed over Terra Nova Bay, downwind Reeves Glacier in Victoria Land (Figure 1). From thermal infrared satellite imagery it has been inferred that strong katabatic winds in the area of Terra Nova Bay can propagate horizontally for hundred of kilometers after passing the coast line (Bromwich, 1989). More precisely, it is believed that the presence of the stable, annually recurring Terra Nova Bay polynya is due to strong, persistent katabatic winds which blow far offshore (Kurtz and Bromwich, 1985). The Terra Nova Bay polynya is characterized by a mean area amounting to  $1300 \text{ km}^2$ , varying from near zero to  $5000 \text{ km}^2$ . In contrast with other antarctic coastal polynyas, its size is poorly correlated with the large scale wind forcing, suggesting that its main forcing is the katabatic wind.

Figure 1: The terrain topography of Antarctica (adapted from *Drewry, (1983)* and the model domain covering the southwestern Ross Sea, the western Ross Ice Shelf, including the Ross Island on its northwestern corner, and Victoria Land, including the Reeves and Byrd Glaciers. The contour interval is 1 km.





Katabatic air blowing from the antarctic continent may be very cold during winter, and the air-sea temperature difference may be as large as 40°C in the coastal region. Consequently heat fluxes from antarctic coastal polynyas are important (Zwally *et al.*, 1985). They have an impact on the energy and momentum budgets of the atmosphere around Antarctica and influence subsequently the atmospheric general circulation and the Earth's climate (Wendler *et al.*, 1983; Gordon, 1988). Another consequence of the strong heat release from the ocean in antarctic coastal polynyas is an enhanced sea-ice formation and a subsequent salt rejection in the water column. For example, sea-ice formation in the Terra Nova Bay polynya could contribute to roughly 10% of the total sea-ice formation in the region of the Ross Sea continental shelf (Kurtz and Bromwich, 1985). Rejected salt could contribute to the formation of coastal dense water and ultimately to the formation of the antarctic bottom water. Nevertheless the impact of salt rejection due to sea-ice formation in high southern latitudes is still debated (Toggweiler and Samuels, 1995).

Since the measurements by the Scott's Northern Party in 1912 (e.g. Priestley, 1962), wintertime observations in the Terra Nova Bay area have mainly been done using satellite imagery (e.g. Bromwich, 1989) and atmospheric data from Automatic Weather Stations (AWS, Bromwich *et al.*, 1993), providing a good data base for testing mesoscale atmospheric models. These observations have also allowed to study polynya-atmosphere interactions in the area of Terra Nova Bay (Kurtz and Bromwich, 1985). It has also been pointed out that the Terra Nova Bay polynya constitutes a good example for studying the atmosphere-ice-ocean interactions in the antarctic coastal zone, since it is close to an existing base (Weller, 1993).

It has been proved that mesoscale models are an useful tool for studying the atmospheric circulation over huge ice sheets such as those covering Antarctica (e.g. Parish, 1984, Bromwich *et al.*, 1990, Gallée and Schayes, 1994) and Greenland (e.g. Meesters *et al.*, 1994, Gallée *et al.*, 1995a). In the case of Terra Nova Bay, the typical length scale that has to be represented in such model must be a few ten of kilometers. For example, it has been shown that simulations of the katabatic flow in the area of Terra Nova Bay requires the use of an horizontal discretization of roughly 10 km (Gallée and Schayes, 1994). This remark also holds for the Terra Nova Bay polynya, since its horizontal extent is typically no more than a few tens of kilometers.

Up to now most of the study of the Terra Nova Bay polynya has been

performed through observational work (e.g. Kurtz and Bromwich, 1985) or by using a steady state polynya model (Darby *et al.*, 1995), which has been developed from the models of Pease (1987) and Ou (1988).

Here it is proposed to go a step further by coupling a more complete polynya model, although still simple, to a mesoscale atmospheric model. In particular the free drift assumption is made for the frazil ice dynamics while dynamical and thermodynamical processes are included for consolidated sea ice. Although the free drift assumption could also be made for consolidated ice when considering summer conditions (Kottmeier and Engelbart, 1991), it is preferable to take into account internal processes in consolidated sea ice for the winter situation. The simple cavitating fluid behavior is assumed for ice rheology (Flato and Hibler, 1992). This means that the ice pack does not resist divergence or shear, but resists convergence. Such assumption could be considered as rather crude in the coastal area, although the horizontal scale of shear in ice could not be represented explicitly with the coarse horizontal resolution ( $\Delta x = 10$  km) used in the present study (Overland and Pease, 1988). Furthermore the objective of this study is to get more insight into air-sea interactions resulting from the opening of the Terra Nova Bay polynya, not into the details of the opening itself.

The model is described in section 3. In section 4 the sensitivity of the atmospheric model to the size of a warm polynya in the cold coastal environment during winter is analyzed with a two-dimensional version of the atmospheric model. A three-dimensional simulation of the Terra Nova Bay polynya is discussed in section 5. Conclusion may be found in section 6.

### 3 THE MODEL

#### 3.1 The Atmospheric Model

The atmospheric model MAR (Modèle Atmosphérique Régional) is fully described in Gallée and Schayes (1994) and Gallée (1995a). A brief description is given here. MAR is a hydrostatic primitive equation model in which the vertical coordinate is the normalized pressure  $\sigma = \frac{p-p_t}{p_s-p_t}$  ( $p$ ,  $p_t = \text{constant}$  and  $p_s$  being the pressure, the model top pressure and the surface pressure respectively). The full continuity equation is taken into account.

The vertical subgrid scale fluxes are treated using the E- $\epsilon$  model of turbulence (Duynderke, 1988), allowing to represent the turbulent mixing length

as a function of the local flow characteristics. This is important because of the complex structure of the katabatic layer (Pettre and André, 1991; Gallée and Schayes, 1992).

The hydrological cycle includes a cloud microphysical model, with conservation equations for cloud droplet, rain drop, cloud ice crystal and snow flake concentrations. The representation of the cloud microphysical processes is essentially based on the Kessler (1969) parameterization.

Detailed solar and infrared radiation scheme are used. The solar radiation scheme is that of Tricot and Berger (1988) modified by Gallée *et al.* (1991). The longwave radiation scheme follows a wide-band formulation of the radiative transfer equation (Morcrette, 1984) and was designed for use in General Circulation Models (GCMs). Clouds properties are taken into account in the solar and infrared radiation scheme by computing the liquid water path in each model layer from the hydrometeor concentration.

In MAR, the lateral boundary conditions allow to take into account the large scale motions, and involve “relaxing” the model-predicted variables towards their large scale values, as in Anthes *et al.* (1989).

Continental ice is assumed to be covered with snow. In this area the atmospheric model is coupled to the snow model adopting the force-restore modeling formulation for soil, following Deardorff (1978). The soil surface parameters are replaced by those of snow, with an assumed snow density of  $330 \text{ kg m}^{-3}$ .

### 3.2 The polynya model

The polynya model used in this study includes simple thermodynamics-dynamics for frazil ice and consolidated ice.

Frazil ice dynamics are modeled using the free drift assumption and the representation of ice accretion in polynyas of Ou (1988). Heat exchanges between areas of open water and the atmosphere are determined assuming that sea surface temperature is at the freezing point. Because salt rejection associated with frazil ice production destabilizes the weak pycnocline in the Southern Ocean, an upward sensible heat flux originates from the deep oceanic layers and partly offset the surface cooling (Martinson, 1993). This contribution of the ocean sensible heat flux is also taken into account.

Consolidated ice dynamics are modeled as in Häkkinen (1986). The surface temperature of the ice pack and the vertical ice growth or decay rates are calculated using the “zero-layer” model of Semtner (1976). Snow on top of

the ice is taken into account.

### 3.2.1 Frazil ice

The frazil ice conservation equation is obtained by constraining its thickness  $h_F$  to respond to the atmospheric forcing  $H_a$ , and its concentration  $A_F$  to follow the evolution of the consolidated ice concentration  $A$ . Taking into account advection effects, the frazil ice conservation equation reads:

$$\frac{\partial A_F h_F}{\partial t} + \frac{\partial A_F h_F u_F}{\partial x} + \frac{\partial A_F h_F v_F}{\partial y} = A_F F - H_F \left. \frac{\partial A}{\partial t} \right|_c \quad (1)$$

with the constraints

$$\frac{\partial A_F}{\partial t} = -\frac{\partial A}{\partial t}$$

and

$$F = (1 - w) \times \frac{HS + HL + IR}{\rho L_{fi}}$$

where  $F$  is the frazil ice production resulting from the heat losses in the atmosphere (sum of the net longwave radiation  $IR$ , the sensible heat flux  $HS$  and the latent heat flux  $HL$ ), multiplied by a factor  $1 - w$  ( $0 \leq w \leq 1$ ) in order to include the sensible heat available from the ocean. As in Hibler (1984), a value of  $w = 0.25$  is chosen for the Ross Sea, although it could be smaller in the area of Terra Nova Bay (Kurtz and Bromwich, 1985).  $\rho$  is the ice density and  $L_{fi} = 2.67 \cdot 10^5 \text{ J kg}^{-1}$  is the latent heat of freezing of sea water. Note that polar night is assumed in the present study, so that the absorbed solar radiation is zero.

The two components  $u_F$  and  $v_F$  of the frazil ice velocity are determined using the free drift assumption:

$$u_F = 0.04 (u_a \cos \alpha - v_a \sin \alpha)$$

$$v_F = 0.04 (u_a \sin \alpha + v_a \cos \alpha)$$

with  $(u_a, v_a)$  the horizontal wind speed 10-m above the surface and  $\alpha = 20^\circ$  is a prescribed turning angle, indicating that the ice moves to the left of the wind stress in the Southern Hemisphere (Darby *et al.*, 1995).  $H_F$  is the frazil collection thickness. Because wind-generated waves and currents prevent ice from consolidating even for the large ice freezing rates in Terra Nova Bay (Bromwich and Kurtz, 1984), a large value  $H_F = 0.4 \text{ m}$  is chosen for the

present study. This assumption must be kept in mind when analyzing the model results.

$\left. \frac{\partial A}{\partial t} \right|_c$  is the rate of lateral accretion through the frazil collection process (Pease, 1987, Ou, 1988). It is parameterized assuming that in each grid box the sea-ice edge is perpendicular to the direction of the frazil ice velocity. The polynya length decrease in this direction is determined according Ou (1988):

$$\left. \frac{\partial L}{\partial t} \right|_c = -\frac{h_F V_F}{H_F - h_F}$$

Note that the consolidated ice drift is not taken into account here, as it is already included in the consolidated ice conservation equation (see below).

### 3.2.2 Consolidated ice

Consolidated ice dynamics are included in the polynya model through conservation equations for momentum and mass. The momentum-balance equation of consolidated ice reads (Häkkinen, 1986):

$$\rho A h \left( \frac{\partial u}{\partial t} + u \frac{\partial u}{\partial x} + v \frac{\partial u}{\partial y} \right) = \rho A h f v + A (\tau_a^x + \tau_w^x) + F_{I,x} \quad (2)$$

$$\rho A h \left( \frac{\partial v}{\partial t} + u \frac{\partial v}{\partial x} + v \frac{\partial v}{\partial y} \right) = -\rho A h f u + A (\tau_a^y + \tau_w^y) + F_{I,y} \quad (3)$$

where  $h$  is the ice thickness,  $u$  and  $v$  are respectively the  $x$  and  $y$  components of momentum vector  $\vec{V}$ ,  $t$  is time,  $f$  is the Coriolis parameter.

$(F_{I,x}, F_{I,y})$  is the divergence of the internal stress tensor  $\sigma_{ij}$ ,  $(i, j) = x$  or  $y$ . It is determined as in Semtner (1987) and Flato and Hibler (1992), and is a simplification of the Hibler (1979) formulation. Only a bulk viscosity  $\zeta$  is taken into account, whereby convergence is resisted in a plastic fashion but divergence is allowed to occur without resistance. With these assumptions the internal stress tensor reads:

$$\sigma_{ij} = \zeta (\epsilon_{11} + \epsilon_{22}) \delta_{ij}$$

where  $\epsilon_{ij}$  is the strain rate tensor ( $\epsilon_{11} + \epsilon_{22} = \nabla \cdot \vec{V}$ ). The bulk viscosity  $\zeta$  is zero for divergence, otherwise  $\zeta = \frac{P^*}{2|\nabla \cdot \vec{V}|}$ , with  $\frac{1}{2|\nabla \cdot \vec{V}|}$  not allowed to exceed  $2.5 \times 10^8 \text{sec}$ .  $\delta_{ij}$  is the Kronecker tensor. This rheology has been referred to as the cavitating fluid rheology by Flato and Hibler (1992).

The dependence of ice strength on ice thickness and compactness  $P^*$  is that of Hibler (1979):

$$P^* = P_0 h \exp(C(1 - A))$$

with  $P_0 = (2)^{1/2} 10^3 \text{ N m}^{-2}$  and  $C = 15$ , as in the mesoscale sea-ice model of Overland and Pease (1988).

The air/ice stress is:

$$(\tau_a^x, \tau_a^y) = \rho_a u_*^2 \left( \frac{u_a}{V_a}, \frac{v_a}{V_a} \right)$$

where  $\rho_a$  is the air density,  $u_*$  is the friction velocity and  $V_a$  is the wind speed computed in the atmospheric model.

The water/ice stress is:

$$(\tau_w^x, \tau_w^y) = \rho_w C_D V (u \cos \beta - v \sin \beta, u \sin \beta + v \cos \beta)$$

where  $V$  is the momentum,  $\rho_w$  is the density of sea water,  $C_D = 1.2 \cdot 10^{-3}$  is a drag coefficient,  $\beta = 20^\circ$  is the angle between the water stress and  $\vec{V} - \vec{V}_w$  (Kottmeier and Engelbart, 1991).

Note that, as in Lynch *et al.* (1995), the assumption of a stagnant mixed layer ocean (i.e.  $\vec{V}_w = 0$ ) has been made and the so-called "sea surface tilt" terms are not included in this version of the momentum equations.

Conservation of mass is included by using conservation equations for ice compactness  $A$  and thickness  $h$ :

$$\frac{\partial A}{\partial t} + \frac{\partial Au}{\partial x} + \frac{\partial Av}{\partial y} = S_A \quad (4)$$

$$\frac{\partial Ah}{\partial t} + \frac{\partial Ahu}{\partial x} + \frac{\partial Ahv}{\partial y} = S_h A \quad (5)$$

where  $S_A$  and  $S_h$  are source terms including the effect of thermodynamic and subgrid scale dynamical processes.  $S_h$  is calculated using the "zero-layer" model of Semtner (1976) and

$$S_A = \Psi + \left. \frac{\partial A}{\partial t} \right|_c$$

where  $\Psi$  is a redistribution function describing changes in sea ice caused by ridging and opening and is related to the internal ice stress. It is determined

for the cavitating fluid rheology by using the method proposed by Shinohara (1990):

$$\Psi = \exp[-C(1 - A)] \nabla \cdot \vec{V}$$

The Arakawa C-finite difference formulation is chosen for the discretization of the polynya model. The momentum equation for consolidated ice is solved explicitly and the first order accurate positive definite conservative scheme of Bott (1989) is used for solving the conservation equations. The time step of the polynya model is the same as in the atmospheric model.

## 4 ICE BREEZE SIMULATIONS

In order to analyze air-sea interactions in conjunction with the presence of a warm polynya in the cold antarctic environment during winter, two-dimensional sensitivity tests are performed by prescribing a coastal polynya with various fixed sizes.

For these two-dimensional simulations, the idealized antarctic topography of Parish (1992) is adapted:

$$z_s(r) = 4000.0 \left(1 - \frac{r}{2 \times 10^6}\right)^{0.45} \quad (6)$$

where  $z_s$  is the terrain height in meters at a distance  $r$  in meters from the center of the ice plateau, located 2000 km far from the ice-sheet margin. After discretizing  $z_s$ , a moving average is performed, giving a maximum ice-sheet slope amounting to 2.2%. Over the ocean, a coastal polynya is included and has a fixed size. A 5% lead fraction is assumed over the other oceanic grid boxes. The surface temperature in the areas of open water is fixed at the freezing temperature (271.2 K).

The roughness length  $z_0$  over the ice sheet is that of snow (0.0001 m). Over the ice-free ocean and sea ice, the values of  $z_0$  have been chosen taking into account the strong winds blowing in the Terra Nova Bay area. Values of 0.001 m and 0.01 m are taken respectively for the areas of open water and for sea ice, assumed to be rough (Guest and Davidson, 1991).

The horizontal grid size is 10 km, with 100 grid points over the ocean and 200 grid points over the ice sheet. There are 18 unequally spaced levels in the atmosphere, with the finest resolution near the surface, as in Gallée (1995a).

Simulations are performed under polar night conditions and a zero large scale wind forcing. The initial vertical temperature profile is that observed by

Table I: Description of the Two-Dimensional Sensitivity Experiments to the Polynya Size. Results are given after 4-days time integration:  $u_a$  is the downslope wind component, in  $\text{m s}^{-1}$ ;  $T_a$  is the air temperature in  $^{\circ}\text{C}$ ; distances indicated between brackets are measured from the coastline over the ocean. The frazil ice flux  $F$  over the first polynya grid point and the corresponding Pease width  $L = H_F u / F$  are also indicated (see text). The experiments are performed with an initial 5% lead fraction, except experiment 1b, in which it is 20%.

E X P	Polyn. Extent (km)	$u_a$ ( $\text{m s}^{-1}$ )			$T_a$ ( $^{\circ}\text{C}$ )			Frazil Flux ( $\text{m day}^{-1}$ )	Pease Width (km)
		(55km)	(25km)	(5km)	(55km)	(25km)	(5km)		
1	0	2.6	4.1	9.8	-46.3	-47.6	-50.8		
1b	0	3.6	5.3	11.6	-37.6	-43.3	-48.8		
2	10	2.7	4.1	13.0	-40.3	-41.8	-42.5	0.56	14.2
3	20	3.2	5.1	14.7	-36.9	-36.6	-43.0	0.60	15.7
4	50	3.9	10.5	17.7	-30.7	-31.6	-42.9	0.67	17.9
5	100	6.4	11.6	18.6	-26.8	-30.2	-40.2	0.67	18.8
6	50	-2.7	5.1	3.8	-27.7	-22.1	-33.6		

Schwerdtfeger (1984, his Figure 6.9 p. 225, the Vostok sounding of July), with temperatures in the lowest level extrapolated downward from the temperature profile above the inversion. This gives an initial temperature of 245 K at the mean sea level (see also Gallée, 1995a).

The experiments are conducted over 4 days. A summary is given in Table I. In experiments 1, 2, 3, 4 and 5 the extent of the coastal polynya is fixed and corresponds to 0, 10, 20, 50, and 100 km respectively. A 6<sup>th</sup> experiment is conducted with a zero ice-sheet surface topography and a 50 km-wide coastal polynya. As no katabatic winds are generated in experiment 6, it is possible to infer the strength of the thermal breeze caused by the temperature contrast between the cold ice surfaces and the warm ocean.

#### 4.1 Atmospheric Response

Results indicate that, as expected, the tremendous heat fluxes from the polynya to the atmosphere are responsible for an important air temperature rise in the katabatic airstream after it has passed the coastline. Total surface heat fluxes as large as  $210^3 \text{ W m}^{-2}$  are simulated from the coastal polynya grid point. The heat flux increases by roughly 10% there when the size of the coastal polynya is increased from 10 to 50 km, in relation with an increase of the katabatic wind speed. In experiment 5 (with a 100-km wide polynya), the



air temperature increases by  $15^{\circ}\text{C}$  between the coast and 105 km farther on sea.

The katabatic wind speed is also larger as the prescribed polynya size is larger. The physical mechanisms responsible for the increase of the katabatic wind speed are probably similar to those due to the presence of leads in the ice pack (see Gallée, 1995b), although they are more marked and their relative importance may differ in the present experiments. It is possible that the atmospheric turbulence which is generated when cold katabatic air comes in contact with the warm polynya surface is responsible for a stronger coupling between the surface atmospheric layer and the overlying atmosphere, allowing a more efficient downward transfer of momentum from the katabatic layer core towards the surface boundary layer. A cold katabatic airflow arriving over the ocean may also be viewed as a gravity current which better conserves its identity in a warmer maritime environment. Furthermore an ice-breeze effect between the cold continent and the warmer ocean may also be considered.

An examination of the results of experiment 6 (in which the ice-sheet topography is assumed to be flat) reveals that the ice breeze generated by the model is significant, even when the polynya width is only 50 km. This indicates that the temperature difference between the cold ice surfaces and the warm polynya surface could be an important factor controlling the katabatic wind speed in the coastal area.

The physical mechanisms responsible for the increase of the katabatic wind speed are analyzed by comparing the results of experiments 1 (no polynya) and 4 (polynya extent = 50 km). Although the prescribed polynya extent in experiment 4 may be overestimated when considering the atmospheric circulation simulated by the two-dimensional version of the model, its impact is well marked and allows an easy analysis. Furthermore the prescribed polynya size of experiment 4 is comparable to the size of the Terra Nova Bay polynya. The potential temperature field after 4-days time integration is shown in Figures 2a (experiment 1) and 2c (experiment 4). Figure 2c exhibits the formation of a warm neutral layer up to 500 m height, due to the heating from the polynya surface. The maximum mixed layer height is simulated above the sea-ice edge. A more detailed analysis of the results (not shown) indicates that the pressure gradient force associated with this neutral layer is in the same direction as the katabatic force, so that in this area an acceleration of the flow in the offshore direction results.

Figure 2: Panel (a): potential temperature in the vertical plane of integration, after 4-days time integration, for experiment 1 (no polynya, 5% lead fraction) as a function of distance to the ice-sheet margin (positive distances are on the ice sheet) and altitude. Contour interval of 2 K.

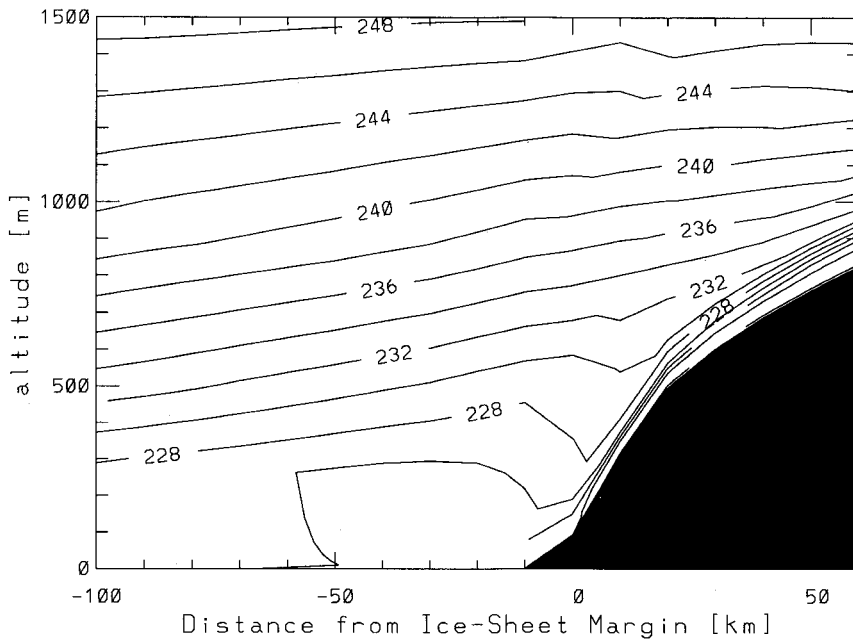


Figure 2: Panel (b): potential temperature in the vertical plane of integration, after 4-days time integration, for experiment 1b (no polynya, 20% lead fraction) as a function of distance to the ice-sheet margin (positive distances are on the ice sheet) and altitude. Contour interval of 2 K.

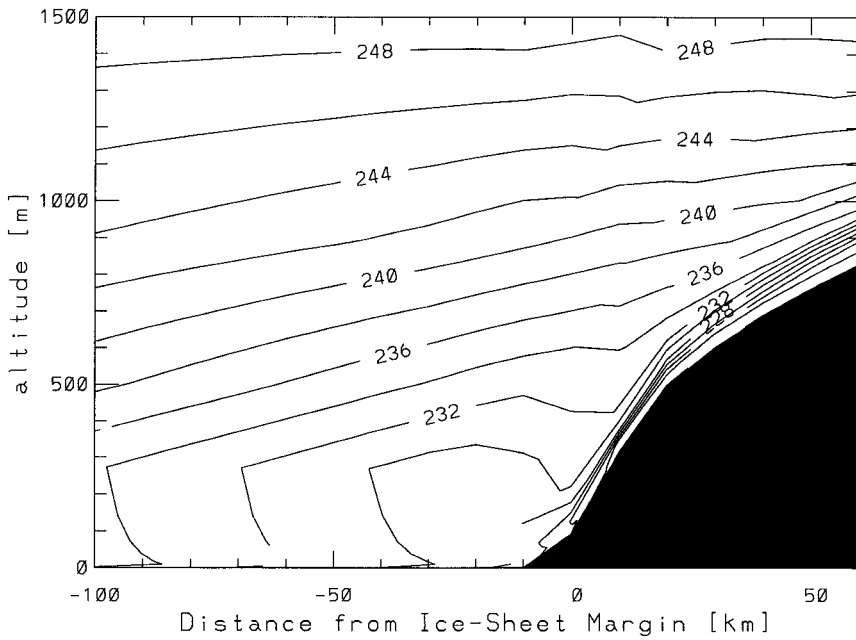


Figure 2: Panel (c): potential temperature in the vertical plane of integration, after 4-days time integration, for experiment 4 (50-km polynya width, 5% lead fraction) as a function of distance to the ice-sheet margin (positive distances are on the ice sheet) and altitude. Contour interval of 2 K.

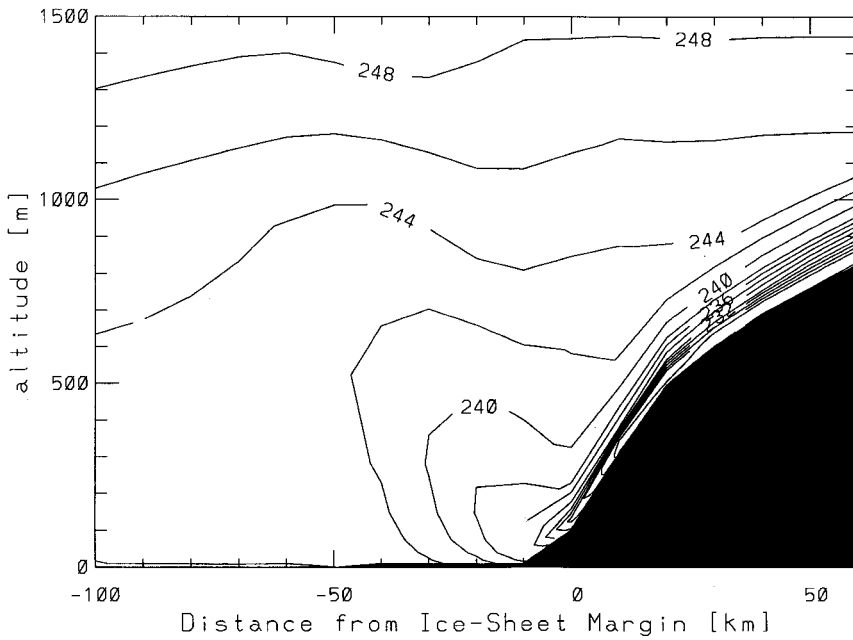


Figure 3: Panel (a):  $x$  (downslope) component of the wind field in the vertical plane of integration, for experiment 1 (no polynya, 5% lead fraction) after 4-days time integration, as a function of distance to the ice-sheet margin (positive distances are on the ice sheet) and altitude. Positive values indicate downslope wind and are represented by solid lines. Contour interval of  $2 \text{ m s}^{-1}$ .

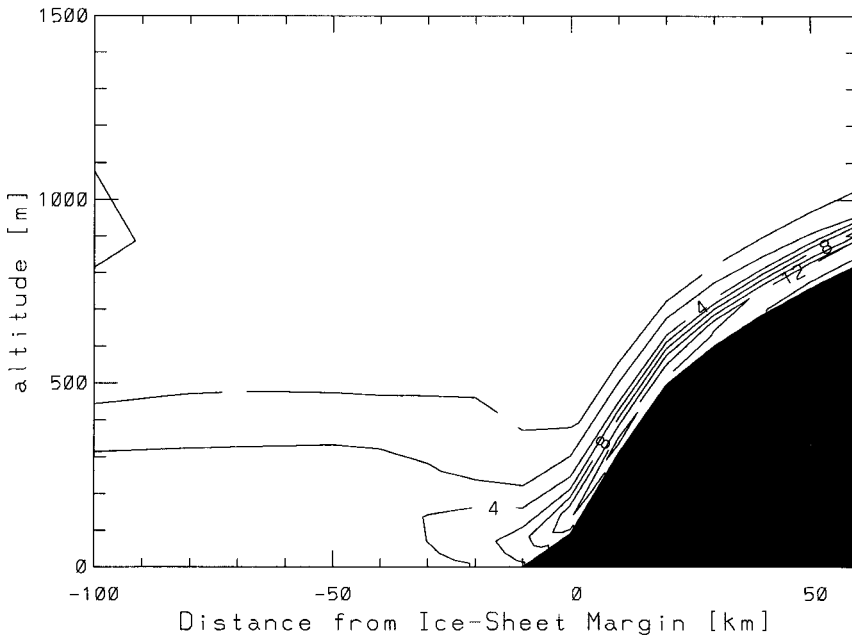


Figure 3: Panel (b):  $x$  (downslope) component of the wind field in the vertical plane of integration, for experiment 1b (no polynya, 20% lead Fraction) after 4-days time integration, as a function of distance to the ice-sheet margin (positive distances are on the ice sheet) and altitude. Positive values indicate downslope wind and are represented by solid lines. Contour interval of  $2 \text{ m s}^{-1}$ .

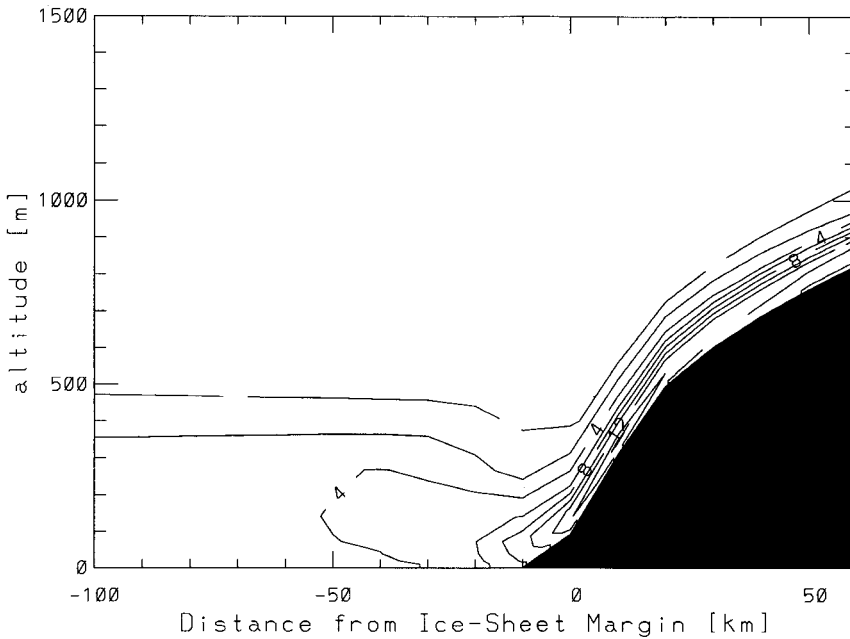
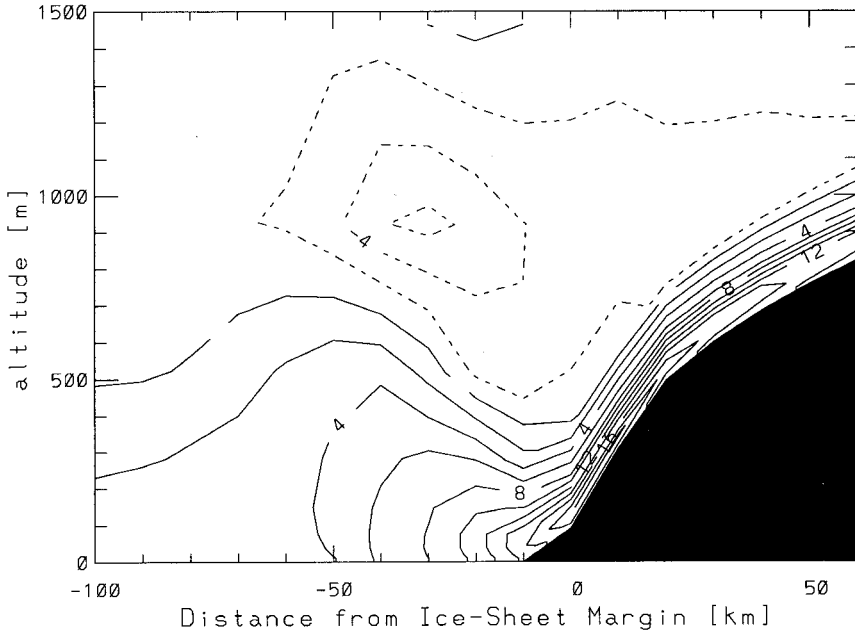


Figure 3: Panel (c):  $x$  (downslope) component of the wind field in the vertical plane of integration, for experiment 1b (50-km polynya width, 5% lead fraction) after 4-days time integration, as a function of distance to the ice-sheet margin (positive distances are on the ice sheet) and altitude. Positive values indicate downslope wind and are represented by solid lines. Contour interval of  $2 \text{ m s}^{-1}$ .



Comparing the downslope wind component for the same experiments (Figures 3a and 3c), it is found that for experiment 4 stronger katabatic winds are simulated in the coastal zone and on the steepest ice-sheet slopes. No wind speed increase is simulated farther upslope (not shown).

Another marked difference is the simulation of a significant return flow aloft, when the polynya exists (Figure 3c). In experiment 4, rising motion also occurs over the ocean and subsidence over the ice-sheet margin, while such motions are not simulated in experiment 1, except negative vertical wind speed in the lowest part of the katabatic layer. The former circulation is the signature of the ice breeze also simulated in experiment 6. The additional subsidence found in experiment 4 may be responsible for the warmer atmospheric temperatures simulated above the katabatic layer and the more marked related inversion strength in this case (compare Figures 2a and 2c). A consequence of the strengthening of the inversion over the ice sheet is an intensification of the associated negative buoyant force, accelerating the katabatic wind in the coastal zone.

Note that an unstable layer is also simulated above the katabatic inversion, especially over the steepest ice-sheet slopes. This unstable layer is distinct from that generated over the polynya (see Figure 2c) and is due to the detrainment of katabatic air from the top of the inversion (e.g. Gallée *et al.*, 1995a).

The coupling of the atmosphere with the polynya surface is also increased in experiment 4 because of the larger destabilization of the low atmosphere in this case (compare the shape of the  $4 \text{ m s}^{-1}$  isotach just above the oceanic surface in Figures 3a and 3c). The wind speed increase 55 km far from the ice-sheet margin (i.e. over the 6<sup>th</sup> oceanic grid point, see Table I, experiments 4 and 5) also reflects this stronger coupling between the surface boundary layer and the overlying atmosphere.

The impact of an increased lead fraction has also been inferred from a sensitivity experiment 1b to experiment 1. Experiment 1b is performed by prescribing a 20% lead fraction in place of the 5% lead fraction of experiment 1. Slightly stronger wind speeds are simulated in experiment 1b (see Table I and Figure 3b). No significant differences are found when comparing the depth of the mixed layer over the ocean (compare Figures 2a and 2b). Nevertheless the mixed layer temperature in experiment 1b is larger by roughly  $5^\circ\text{C}$ , 50 km far from the ice-sheet margin, while the temperature difference between both experiments is only  $2^\circ\text{C}$  over the ice sheet. In fact a marked temperature



gradient is simulated over the ocean in experiment 1b, explaining the onset of a land breeze in this case (compare Figures 3a and 3b). Nevertheless no significant strengthening of the inversion is simulated between experiments 1 and 1b.

To summarize, areas of open water are responsible for the existence of a significant temperature gradient between the ocean and the ice sheet, and the subsequent generation of an ice-breeze effect reinforcing the wind coming off the ice sheet. For sufficiently large areas of open water in the coastal zone, like polynyas, the ice breeze is strong enough to be responsible for a marked subsidence of warm maritime air over the ice sheet, reinforcing the inversion and intensifying the katabatic flow.

## 4.2 Polynya Response

As already mentioned, the strong cold katabatic winds blowing over the warm ocean are responsible for tremendous heat fluxes and frazil ice production. The frazil ice flux over the first polynya grid point (in  $\text{m day}^{-1}$ ) is shown in Table I. Pease (1987) has shown that the width  $L$  of a steady state wind-driven polynya may be approximated by

$$L = H_F u / F$$

where  $F$  is the frazil ice flux,  $H_F$  is the frazil ice collection thickness, and  $u$  is the component of the consolidated ice drift perpendicular to the coast. The length  $L$  is referred hereafter as the Pease width. Its value for  $H_F = 0.4$  m and  $u$  computed from a free drift model of consolidated ice:

$$u = 0.024 (u_a \cos \alpha - v_a \sin \alpha)$$

where  $(u_a, v_a)$  is the horizontal wind speed 10-m above the surface and  $\alpha = 20^\circ$ , is shown in Table I for the first coastal grid point. Note that  $L$  is purely indicative of the size that a polynya would have if it is allowed to respond to the wind forcing.  $L$  does not necessarily correspond to the prescribed polynya width of experiments 1–5.

It is found in Table I that the frazil ice flux  $F$  increases when the prescribed polynya width increases. This reflects the impact of the large heat losses from the ocean in conjunction with larger katabatic winds in the coastal area. It is also seen that the resulting Pease width is not affected by the larger  $F$ . Rather it is slightly increased, amounting roughly to 20 km in experiment 5. The same

assessment holds when the Pease width is averaged over the two first polynya grid points (i.e. over 20 km, experiments 3, 4 and 5). This weak sensitivity of the Pease width to the wind speed in the coastal zone was already mentioned by Pease (1987) and results from the counteracting effect of the increased frazil ice production and increased offshore ice drift. Looking at the evolution of the atmospheric variables farther on sea (Table I), it is found that the rapid weakening of the katabatic flow could be responsible for a rapid weakening of the offshore ice drift. Nevertheless the distance over which the weakening of the katabatic flow occurs is larger than the Pease width, so that the polynya could not be affected. On the other hand, it must be stressed that the Pease width may overestimate the actual polynya width, since internal stresses in ice are not included. In this case the compression effects resulting from the katabatic wind weakening at some distance from the polynya edge could be responsible for a decrease of the offshore ice drift. This effect is analyzed in a last experiment (not shown) in which the polynya model is activated in the two-dimensional version of MAR. In this case a significant open water fraction is simulated in the two first oceanic grid boxes near the ice-sheet margin, and amounts to 75% and 59% there. A measure of the corresponding polynya width could be  $(0.75 + 0.59) \times 10 \text{ km} = 13.4 \text{ km}$ , a lower value than the Pease width deduced from the results of experiments 2–5.

It must also be noted that the two-dimensional assumption underestimates the katabatic wind speed in the area of Terra Nova. In order to address these two points, a three-dimensional experiment in the area of Terra Nova Bay will now be presented.

## 5 SIMULATION OF THE TERRA NOVA BAY POLYNYA

In this section, one shows the results of a three-dimensional simulation of the Terra Nova Bay polynya. The model domain is that of Gallée (1995a) (Figure 1). It is taken from the Drewry (1983) map and consists of  $160 \times 160$  grid points, covering the southwestern Ross Sea and a part of the antarctic continent, i.e. the northwestern Ross Ice Shelf, including the Ross Island, and Victoria Land, including the Reeves and Byrd Glaciers. The Drygalski Ice Tongue is also included in the model domain. As for the two-dimensional experiments, the atmospheric model is initialized with the Vostok sounding and

polar night is assumed. As the size of the Terra Nova Bay polynya is poorly correlated with the large scale wind forcing, the latter is assumed to be zero in the present study.

The polynya model is initialized with a 20% lead fraction. The initial consolidated ice thickness is 1 m. As in the two-dimensional simulation a frazil ice collection thickness of 0.4 m is assumed. This rather high value has been chosen in order to simulate a realistic polynya area in Terra Nova Bay and must be considered regarding the other assumptions made in the polynya model. For example an uniform frazil ice thickness is assumed in each oceanic grid box. Nevertheless, the low air temperatures over the Terra Nova Bay polynya could accelerate the transformation of frazil ice into pancake ice, reducing the heat exchange between the atmosphere and the polynya. Such process is not represented in the model so that frazil ice production could be overestimated. On the other hand the wind waves prevent grease ice from consolidating and are responsible for setting up long rows of frazil ice parallel to the katabatic wind direction (Kurtz and Bromwich, 1985). The efficiency of the actual frazil collection process is also increased owing to herding of frazil ice by the wind waves. A consequence of stronger winds is a larger frazil collection thickness (Bauer and Martin, 1983).

### 5.1 Polynya Response

The simulation is conducted over 4 days. The open water fraction after the 4-days simulation is shown on Figure 4. For the sake of clarity, only a part of the domain is shown. Note also that in all Figures displaying model output on  $\sigma$ -surfaces, the South Pole direction is for  $y$  positive while the southwestern corner of Terra Nova Bay (referred to hereafter as Bay End) is located at grid point ( $x = 10$  km,  $y = 10$  km). After the 4-days simulation, the total area of open water in a  $100 \times 100$  km<sup>2</sup> square including Terra Nova Bay and the Drygalski Ice Tongue (southwestern corner coordinates:  $x = 10$  km,  $y = 50$  km — Figure 4) does not vary by more than 4 km<sup>2</sup> per hour. It amounts roughly to 3500 km<sup>2</sup>, a larger area than the mean area (1300 km<sup>2</sup>) mentioned by Kurtz and Bromwich (1985), but such apparent disagreement must be considered with caution, since the present estimation includes the area of loosely or thin consolidated ice. At the end of the simulation, the total area of open water occupies 9.7% of the oceanic domain, a typical winter situation in the southwestern Ross Sea (e.g. Gloersen *et al.*, 1992).

Figure 4: Simulated open-water fraction after 4-days time integration, in the southwestern Ross Sea. Contour interval is 20%. Ice sheet elevation contours in meters (dashed) are also plotted. Contour interval is 0.2 km. Label DI refers to the location of the Drygalski Ice Tongue.

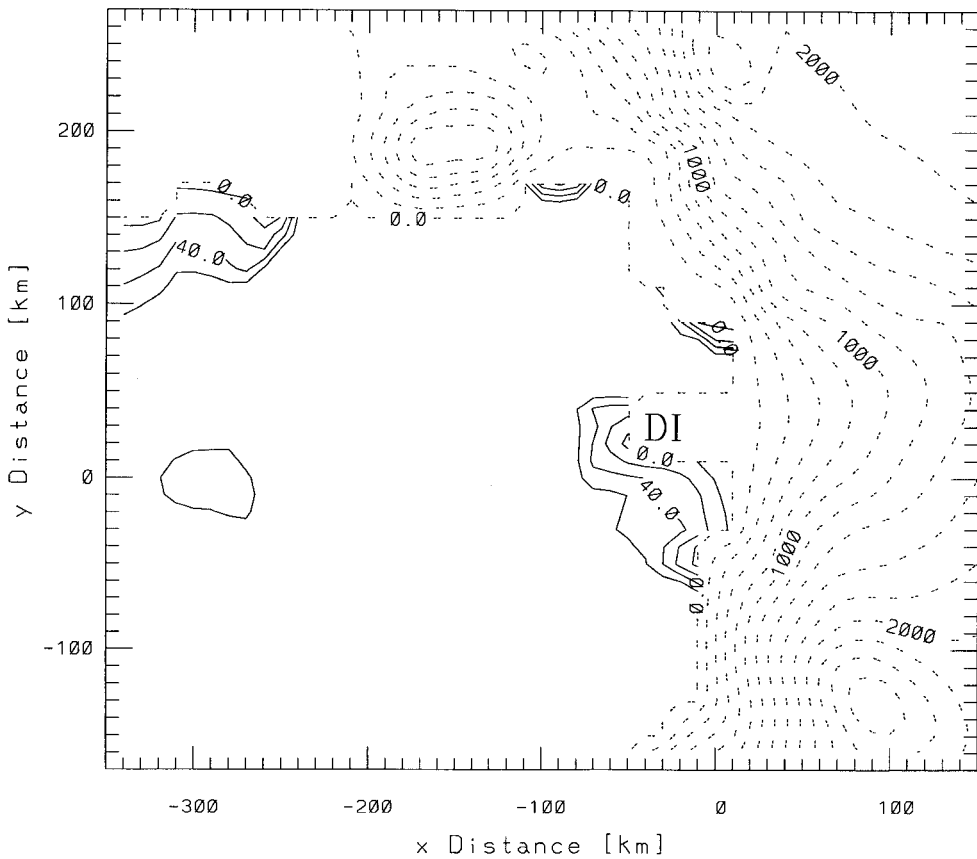


Figure 5: Simulated sea-ice drift vectors after 4-day integration. Ice sheet elevation contours (km) are also plotted. The contour interval is 0.2 km. Vectors whose magnitude is less than  $1 \text{ cm s}^{-1}$  are not plotted. Vectors are plotted every 2 grid points. The arrow length at the right bottom corner of the graph represents sea-ice drift velocity amounting to  $120 \text{ cm s}^{-1}$ .

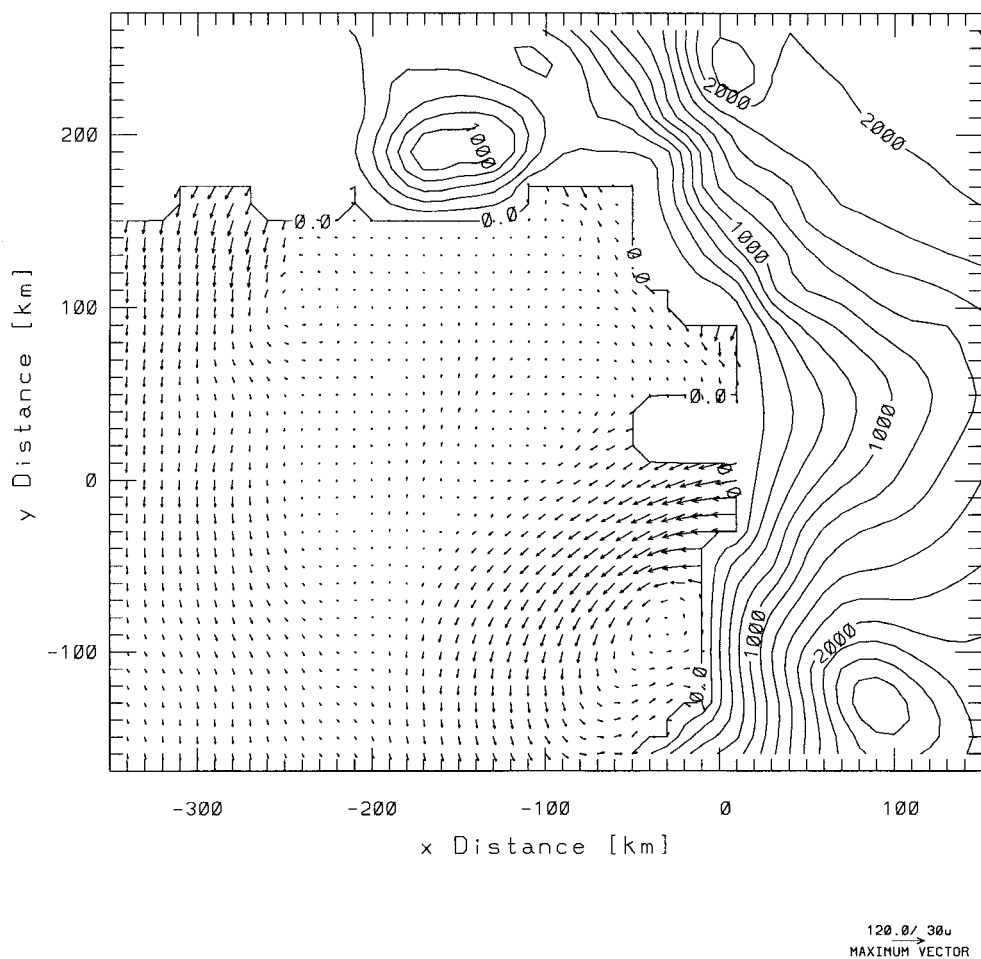
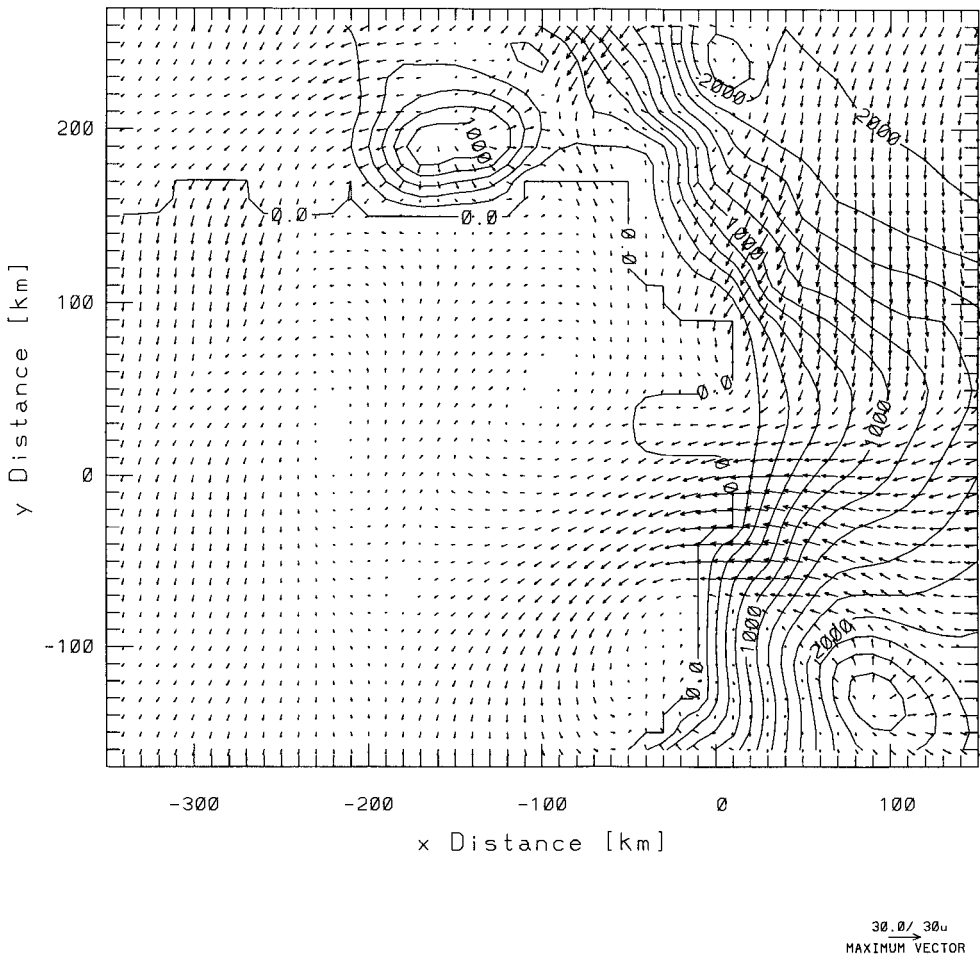


Figure 6: Simulated katabatic wind vectors after 4-day integration for the lowest level of the model (10 m above the surface), Ice sheet elevation contours (km) are also plotted. The contour interval is 0.2 km. Vectors whose magnitude is less than  $1 \text{ m s}^{-1}$  are not plotted. Vectors are plotted every 2 grid points. The arrow length at the right bottom corner of the graph represents wind speed amounting to  $30 \text{ m s}^{-1}$ .



The Terra Nova Bay polynya is simulated mainly northward of Drygalski Ice Tongue, in rough agreement with the observations. An area of open water is also simulated eastward of the Drygalski Ice Tongue. It may be correlated with a southwesterly sea-ice drift there (Figure 5), in slight disagreement with the observed southerly sea-ice drift. It must be noted that in the present version of the model, the sea-ice drift is forced only by the wind, which blows from the continent over the Drygalski Ice Tongue (Figure 6). Nevertheless an open water area may also be observed eastward of Drygalsky Ice Tongue, as it is seen for exemple in Kurtz and Bromwich (1985, their Figures 3b and 3c). Note that a southerly sea-ice drift is simulated farther on sea, resulting from the katabatic forcing coming off the Ross Ice Shelf. Furthermore, the polynya observed to the north of the Ross Ice Shelf is also simulated by the model, responding to the katabatic forcing in that region.

The consolidated ice thickness after 4-days simulation shown in Figure 7 reflects mainly the influence of the sea-ice drift. Thin ice is simulated in the area of Terra Nova Bay, where ice divergence occurs. In contrast, much thicker ice is simulated northward and southeastward of Terra Nova Bay, a pattern again resembling Figure 3 of Kurtz and Bromwich (1985).

## 5.2 Air-Sea Interactions over Terra Nova Bay

The analysis of the katabatic wind speed allows some insight into the impact of air-sea interactions in the area of Terra Nova Bay. The present simulation may be easily compared to those made by Gallée (1995b). Indeed the model set up is similar, except that in that study (i) the Drygalsky Ice Tongue is not included, and (ii) an uniform open water area is prescribed in each oceanic grid box. It is first seen that the maximum wind speed in Terra Nova Bay is significantly larger in the latter case, even when considering a prescribed uniform 30% lead fraction (simulation L30 of Gallée, 1995b). After 3-day simulation for example, the maximum wind speed in the lowest model level (roughly 10 m above the surface) is  $23.3 \text{ m s}^{-1}$  ( $23.1 \text{ m s}^{-1}$  in L30) while in the fourth model level (roughly 80 m above the surface) it is  $28.4 \text{ m s}^{-1}$  ( $27.8 \text{ m s}^{-1}$  in L30). Furthermore the maximum wind speed is now simulated in the fifth model level (roughly 150 m above the surface) and amounts to  $28.8 \text{ m s}^{-1}$ , in better agreement with the observations of Parish and Bromwich (1989).

The wind speed at that level but after 4-days simulation is shown in Figure 8. the strongest winds are simulated around the 400-m surface elevation contour,

Figure 7: Simulated sea ice thickness after 4-day integration. Contour interval is 0.1 m. Ice sheet elevation contours (km) are also plotted. The contour interval is 0.2 km.

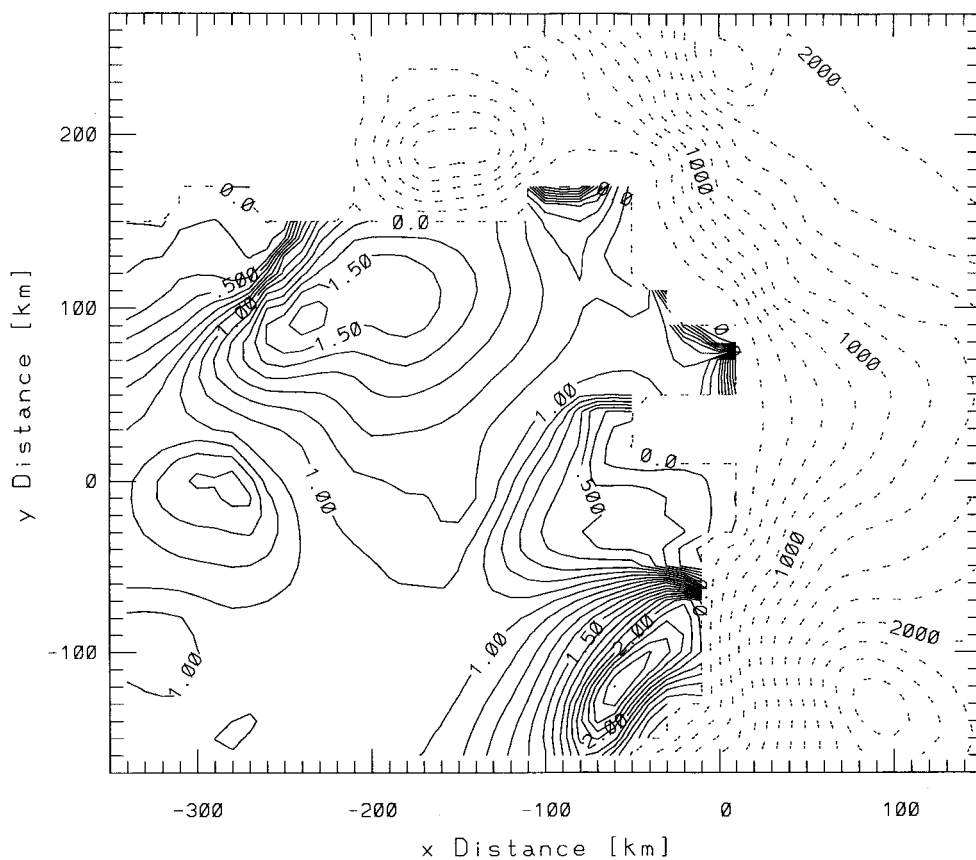
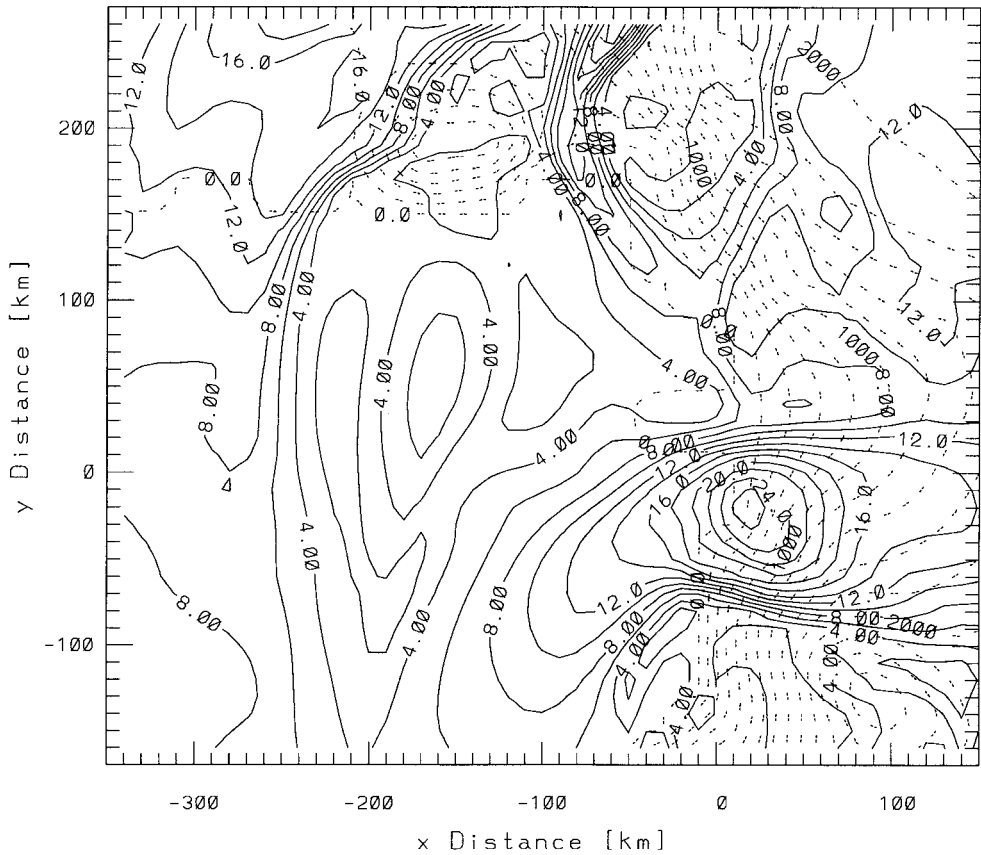




Figure 8: Simulated katabatic wind speed after 4-day integration at the fifth level of the model (150 m above the surface). Contour interval is  $2 \text{ m s}^{-1}$ . Ice sheet elevation contours are also plotted. The contour interval is  $0.2 \text{ km}$ .



closer to the coastline than in Gallée and Schayes (1994). This intensification of the katabatic winds may be compared to that simulated with the two-dimensional version of the model, and results from a strong ice-breeze effect reinforcing the negative buoyant force over the steepest slopes, near the ice-sheet margin.

The katabatic winds blowing over the Terra Nova Bay polynya are strong and bring cold continental air in contact with a warm open water surface. Large friction velocities  $u_*$  are simulated over the open water area and sea ice there, amounting to roughly  $1 \text{ m s}^{-1}$ . Such strong friction velocities explain the rather rapid drift of loosely ice in Terra Nova Bay (Figure 5).

Furthermore the heat fluxes over the areas of open water are very strong. At Bay End for example, the sum of the heat losses is  $1348 \text{ W m}^{-2}$ . A maximum of  $1517 \text{ W m}^{-2}$  is simulated 10 km northward. The daily frazil ice production rate is shown in Figure 9. Large values are simulated, amounting to  $0.50 \text{ m day}^{-1}$  near the coast of Terra Nova Bay. Even when taking into account that 25% of the surface heat losses are offset by the oceanic upward sensible heat flux, the frazil ice production rate is twice larger than previously estimated (e.g.  $0.22 \text{ m day}^{-1}$ , Kurtz and Bromwich, 1985). It is possible that such difference is due to the assumptions made when modelling the frazil ice. For example it is assumed in the model that the presence of frazil ice in open water areas does not alter the heat transfer with the atmosphere, probably in contrast with the actual behavior in the more distal parts of the polynya, where the surface energy balance could be a complicated function of the types and quantities of sea ice present (Kurtz and Bromwich, 1985).

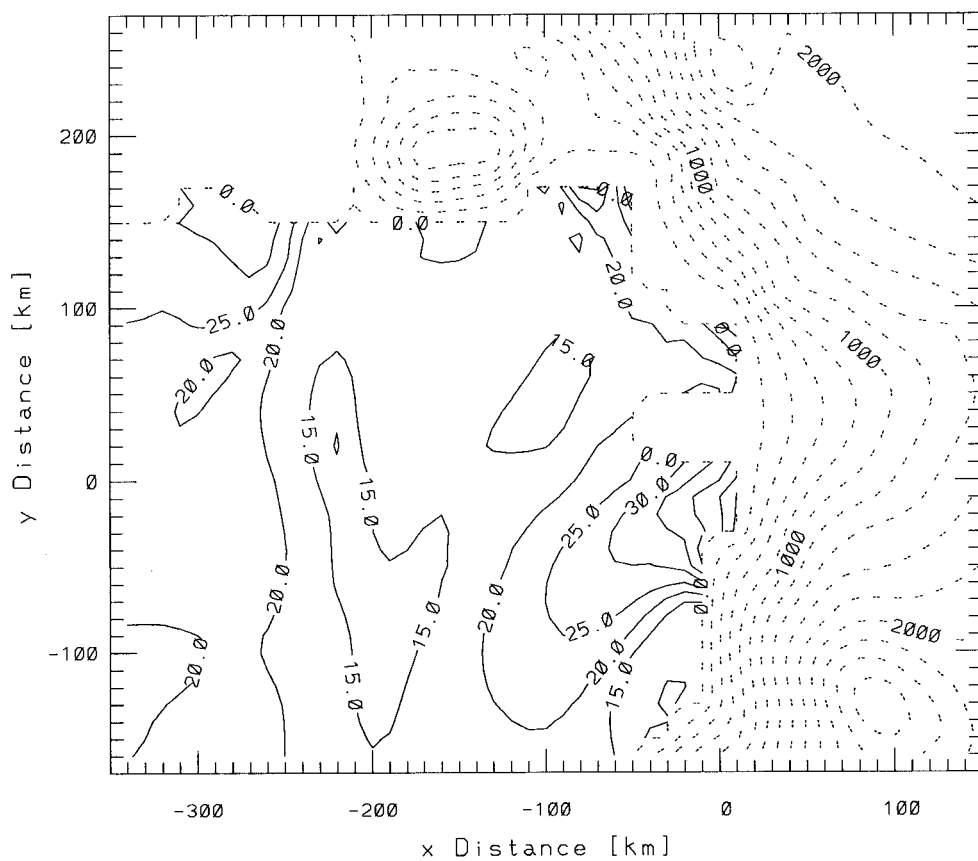
It is also possible that the frazil ice production rate simulated in the present study is close to the actual production rate. However this is possibly less acceptable since a large frazil ice collection thickness ( $H_W = 0.4 \text{ m}$ ) must be prescribed in the polynya model in order to simulate a realistic Terra Nova Bay polynya.

## 6 CONCLUSION

The three-dimensional Atmospheric Mesoscale Circulation Model MAR has been coupled to a wind-driven polynya model, generalized from that of Ou (1988), by including sea-ice dynamics and thermodynamics.

The atmospheric model sensitivity to the presence of a prescribed coastal

Figure 9: Daily frazil production rate after 4-day integration. Contour interval is 5 cm. Ice sheet elevation contours (km) are also plotted. The contour interval is 0.2 km.



1

polynya is analyzed by performing two-dimensional simulations. For sufficiently large areas of open water located in the coastal zone, a strong ice breeze is superimposed on the katabatic flow, causing subsidence of warm maritime air over the ice sheet and a subsequent intensification of the inversion and the katabatic wind. Nevertheless this has little impact on the polynya size predicted by the Pease (1987) model, since stronger katabatic winds reinforce the heat exchange between the polynya and the atmosphere. On the other hand the decay of katabatic winds over the ocean has an impact on the polynya size, owing to internal stresses in consolidated sea ice.

A simulation of the Terra Nova Bay polynya is also performed with the three-dimensional version of the model. The size of the simulated polynya is in qualitative agreement with the observations. As for the two-dimensional experiments, the katabatic flow is significantly reinforced over the ice-sheet slopes in the vicinity of the polynya (i.e. over Reeves Glacier). A good agreement is now found between observation and simulation of the katabatic wind in this area. The simulated heat losses from the Terra Nova Bay polynya are larger by a factor 2 than in previous estimates, so that brine rejection into the ocean could also be more important than expected. Nevertheless processes like the consolidation of frazil ice into pancake ice are still poorly understood and not included in the model, leading to an overestimation of the simulated heat losses. Other missing processes, like frazil ice herding by wind waves, could have a strong impact on the polynya size. This stresses the need for having a better knowledge of the processes governing the frazil ice evolution in the Terra Nova Bay polynya, in order to develop new parameterizations.

Because it provides a realistic atmospheric forcing, the atmospheric model used here could be an useful tool for developing such parameterization.

### Acknowledgment

This research is sponsored by the Belgian Program "Scientific research on the Antarctic" (Services of the Prime Minister - Federal Office for Scientific, Technical and Cultural Affairs) under contract A3/10/001. I also acknowledge Prof. André Berger, Prof. Guy Schayes, and Dr. Jean-Pascal van Ypersele for continued support.

## References

- [1] Anthes, R.A., Y.-H. Kuo, E.-Y. Hsie, S. Low-Nam, and T.W. Bettge, 1989: Estimation of skill and uncertainty in regional numerical models. *Quart. J. Roy. Meteor. Soc.*, **115**, 763–806.
- [2] Argentini, S., Mastrantonio, G., Fiocco, G. and Ocone, R., 1992: Complexity of the wind field as observed by a sodar system and by automatic weather stations on the Nansen Ice Sheet, Antarctica, during summer 1988–89: two case studies. *Tellus*, **44B**, 422–429.
- [3] Bauer, J. and S. Martin, 1983: A model of grease ice growth in small leads. *J. Geophys. Res.*, **88**, 2917–2925.
- [4] Bott, A., 1989: A positive definite advection scheme obtained by nonlinear renormalization of the advective fluxes. *Mon. Wea. Rev.*, **117**, 1006–1015.
- [5] Bromwich, D.H., and Kurtz, D.D., 1984: Katabatic Wind Forcing of the Terra Nova Bay Polynia, *J. Geophys. Res.*, **89**, 3561–3572.
- [6] Bromwich, D.H., 1989: Satellite analyses of Antarctic katabatic wind behavior. *Bull. Amer. Meteor. Soc.*, **70**, 738–749.
- [7] Bromwich, D.H., Parish, T.R., and Zorman, C.A., 1990: The confluence zone of the intense katabatic winds at Terra Nova Bay, Antarctica, as derived from airborne sastrugi surveys and mesoscale numerical modeling. *J. Geophys. Res.*, **95**, 5495–5509.
- [8] Bromwich, D.H., T.R. Parish, A. Pellegrini, C.R. Stearns, and G.A. Weidner, 1993: Spatial and temporal characteristics of the intense katabatic winds at Terra Nova Bay, Antarctica. *Antarctic meteorology and climatology: studies based on automatic weather stations, Antarctic Research Series*, **61**, 47–48.
- [9] Deardorff J.W., 1978: Efficient Prediction of Ground Surface Temperature and Moisture with Inclusion of a Layer of Vegetation. *J. Geophys. Res.*, **83**, 1889–1903.
- [10] Drewry, D.J., 1983: The surface of the Antarctic ice sheet, *Antarctica: Glaciological and Geophysical Folio*, sheet 2, D.J. Drewry, Ed., Scott Polar Research Institute. University of Cambridge, England.

- [11] Duynkerke, P.G., 1988: Application of the  $E - \epsilon$  turbulence closure model to the neutral and stable atmospheric boundary layer. *J. Atmos. Sci.*, **45**, 865–880.
- [12] Gallée, H., J.P. van Ypersele, T. Fichet, C. Tricot, and A. Berger, 1991: Simulation of the last glacial cycle by a coupled 2-D climate-ice sheet model, 1, The climate model, *J. Geophys. Res.*, **96**, 13,139–13,161.
- [13] Gallée, H., and G. Schayes, 1992: Dynamical aspects of katabatic winds evolution in the Antarctic Coastal Zone. *Bound.-Layer Meteor.*, **59**, 141–161.
- [14] Gallée, H., and G. Schayes, 1994: Development of a Three-Dimensional Meso- $\gamma$  Primitive Equations Model, Katabatic Winds Simulation in the area of Terra Nova Bay, Antarctica. *Mon. Wea. Rev.*, **122**, 671–685.
- [15] Gallée, H., 1995a: Simulation of the Mesocyclonic Activity in the Ross Sea, Antarctica. *Mon. Wea. Rev.*, **123**, 2051–2069.
- [16] Gallée, H., 1995b: Mesoscale atmospheric circulations over the southwestern Ross Sea sector, Antarctica. *J. Appl. Meteor.* (in press).
- [17] Gallée, H., O. Fontaine de Ghélin and M. Van den Broeke 1995a: Simulation of Atmospheric Circulation during the GIMEX 91 Experiment using a Meso- $\gamma$  Primitive Equations Model. *J. of Climate*, **11**, 2843–2859.
- [18] Gallée H., Pettré, P. and Schayes G., 1995b: Sudden cessation of katabatic winds in Adélie Land, Antarctica, *J. Appl. Meteor.* (in press).
- [19] Gloersen, P., W.J. Campbell, D.J. Cavalieri, J.C. Comiso, C.L. Parkinson, and H.J. Zwally, 1992: Arctic and Antarctic Sea Ice, 1978–1987: Satellite passive-microwave observations and analysis. *NASA SP-511*, 290 p.
- [20] Gordon, A.L., 1988: The Southern Ocean and global climate. *Oceanus*, **31**, 2, 39–46.

- [21] Guest, P.S. and K.L. Davidson, 1991: The aerodynamic roughness of different types of sea ice. *J. Geophys. Res.*, **96**, 4709–4721.
- [22] Häkkinen, S., 1986: Coupled Ice-Ocean Dynamics in the marginal ice zones: upwelling/downwelling and eddy generation. *J. Geophys. Res.*, **91**, 819–832.
- [23] Hibler, W.D., 1979: A dynamic thermodynamic model sea ice model. *J Phys Oceanogr.* **6**, 815–846.
- [24] Hibler, W.D., 1984: The role of sea-ice dynamics in modeling CO<sub>2</sub> increases. In *Climate processes and climate sensitivity* (J.E. Hansen and T. Takahashi Eds), *Geophys. Monogr.* **29**, *M. Ewing Vol. 5*, AGU, 241
- [25] Kessler E., 1969: On the distribution and continuity of water substance in atmospheric circulation; *Meteorological Monography*, vol.27, American meteorological society.
- [26] Kottmeier, Ch. and D. Engelbart, 1991: Generation and atmospheric heat exchange of coastal polynyas in the Weddell Sea. *Bound.-Layer Meteor.*, **60**, 207–234.
- [27] Kurtz D.D. and D.H. Bromwich D.H., 1985: A Recurring, Atmospherically Forced Polynia in Terra Nova Bay. *Oceanology of the Antarctic Continental Shelf, Antarctic Research Series*, **43**, 177–201.
- [28] Lynch, A.H., W.L. Chapman, J.E. Walsh and G. Weller, 1995: Development of a regional climate model of the western Arctic. *J. Climate* **8**, 1555–1570.
- [29] Martinson, D. G., 1993: Ocean Heat and seasonal sea ice thickness in the Southern Ocean. In : *Ice in the Climate System, NATO Advanced Research Workshop, Aussois (France)*, W.R. Peltier (Ed.), Springer-Verlag Berlin Heidelberg, NATO ARW Series, vol.12, 597–609.
- [30] Morcrette, J.J., 1984: Sur la paramétrisation du rayonnement dans les modèles de la circulation générale atmosphérique. Univ. des Sci. et Tech. de Lille, Lille, France, Thèse de Doctorat d'Etat, 373 p.

- [31] Ou H.W., 1988: A Time-Dependant Model of a Coastal Polynia, *J Phys Oceanogr.*, **18**, 584–590.
- [32] Overland, J.E. and C.H. Pease, 1988: Modeling ice dynamics of coastal seas, *J Geophys Res*, **93**, 15619–15637.
- [33] Parish T.R., 1984: A Numerical Study of Strong Katabatic Winds over Antarctica. *Mon. Wea. Rev.*, **112**, 545–554.
- [34] Parish, T.R., and Bromwich, D.H., 1989: Instrumented aircraft observations of the katabatic wind regime near Terra Nova Bay. *Mon. Wea. Rev.*, **117**, 1570–1585.
- [35] Parish T.R., 1992: On the role of antarctic katabtic winds in forcing large-scale tropospheric motions. *J. Atmos. Sci.*, **49**, 1374–1385.
- [36] Pease C.H., 1987: The Size of Wind-Driven Coastal Polynias. *J Geophys Res*, **92**, 7049–7059.
- [37] Pettré, P., and J.-C. André, 1991: Surface-pressure change through Loewe's phenomena and katabatic flow jumps: study of two cases in Adélie Land, Antarctica. *J. Atmos. Sci.*, **48**, 557–571.
- [38] Priestley R.E., 1962: Scott's Northern Party, *J. Geogr.*, **128**, 129–140.
- [39] Schwerdtfeger W., 1984: Weather and Climate of the Antarctic. *Developments in Atmospheric Sciences*, **15**, Elsevier, 261 pp.
- [40] Semtner, A.J., 1976: A model for the thermodynamic growth of sea ice in numerical investigations of climate. *J. Phys. Oceanogr.*, **6**, 379–389,
- [41] Semtner, A.J., 1987: A numerical study of sea ice and ocean circulation in the Arctic. *J. Phys. Oceanogr.*, **17**, 1077–1099.
- [42] Shinohara Y., 1990: A redistribution function applicable to a dynamic model of sea ice. *J Geophys Res*, **95**, 13423–13431.
- [43] Smith, S.D., Muench, R.D., and Pease, C.H., 1990: Polynyas and Leads: an Overview of Physical Processes and Environment. *J Geophys Res*, **95**, 9461–9479.



- [44] Toggweiler, J.R. and Samuels, B. 1995. Effect of sea ice on the salinity of Antarctic bottom waters. *J. Phys. Oceanogr.*, **25**, 1980–1997.
- [45] Tricot, C., and A. Berger, 1988: Sensitivity of present-day climate to astronomical forcing, in *Long and Short Term Variability of Climate Lect. Notes Earth Sci.*, vol. 16, edited by H. Wanner and U. Siegenthaler, 132–152.
- [46] Weller, G.E. (ed), 1993: The role of the Antarctic in Global Change: An International Plan for a Regional Research Programme. *Cambridge, SCAR*, 54p.
- [47] Wendler, G., Kodama, Y., and Poggi, A., 1983: Katabatic wind in Adélie Land. *Antarctic J. U.S.*, **18**, 236–238.
- [48] Zwally H.J., Comiso J.C. and Gordon A.L., 1985: Antarctic Off-shore Leads and Polynias and Oceanographic Effects. *Oceanology of the Antarctic Continental Shelf, Antarctic Research Series 43*, 203–226.

**DYNAMICS OF THE ANTARCTIC ICE SHEET  
AND  
ENVIRONMENTAL CHANGE**

F. PATTYN<sup>1</sup>,  
H. DECLEIR and  
D. WILLAERT

VRIJE UNIVERSITEIT BRUSSEL  
GEOGRAFISCH INSTITUUT  
Pleinlaan 2  
B-1050 Brussels  
Belgium

<sup>1</sup> Corresponding author E-mail : [fpattyn@vub.ac.be](mailto:fpattyn@vub.ac.be)



## Contents

<b>ABSTRACT</b>	<b>1</b>
<b>1 RESEARCH GOALS</b>	<b>2</b>
1.1 UNDERSTANDING ICE SHEET SYSTEMS . . . . .	3
1.2 PALEO-RECONSTRUCTION AND MODELING . . . . .	5
<b>2 MATERIALS AND METHODS</b>	<b>7</b>
2.1 THE ICE SHEET SYSTEM MODEL (ICE2D) . . . . .	7
2.1.1 Ice Deformation . . . . .	7
2.1.2 Strain-Rates and Velocities . . . . .	8
2.1.3 Thermodynamics . . . . .	9
2.1.4 Isostatic Bedrock Adjustment . . . . .	11
2.1.5 Basal Motion . . . . .	11
2.1.6 Numerical Computation . . . . .	14
2.2 GLACIER SURFACE VELOCITY FROM SEQUENTIAL SPOT IMAGERY	15
2.2.1 Introduction . . . . .	15
2.2.2 The Image Matching Technique . . . . .	16
2.2.3 Precise Image Co-Registration . . . . .	18
<b>3 RESULTS</b>	<b>19</b>
3.1 DATA SAMPLING AND ENVIRONMENTAL FORCING . . . . .	19
3.2 ICE STREAM DYNAMICS I: BASAL MOTION AND CYCLICITY . . . . .	22
3.2.1 Experimental Setup . . . . .	23
3.2.2 Oscillatory Behavior . . . . .	24
3.3 ICE STREAM DYNAMICS II: SHIRASE GLACIER . . . . .	28
3.3.1 Regional Description and Observations . . . . .	28
3.3.2 Present Stress Field of Shirase Glacier . . . . .	29
3.3.3 Steady State Modeling Experiments . . . . .	31
3.3.4 Dynamic Modeling Experiments . . . . .	32
3.4 DYNAMICS OF THE ICE SHEET IN EAST DRONNING MAUD LAND . . . . .	34
3.4.1 Situation and Glacial History of the Sør Rondane . . . . .	35
3.4.2 Steady State Sensitivity Experiments . . . . .	35
3.4.3 Dynamic Experiments . . . . .	39
3.5 SURFACE GLACIER VELOCITIES OF GJELBREEN . . . . .	46
3.5.1 Area and Image Selection . . . . .	46
3.5.2 Results and Evaluation . . . . .	47

<b>4 DISCUSSION</b>	<b>51</b>
4.1 ICE STREAM DYNAMICS . . . . .	51
4.2 PALEO ICE SHEET IN EAST DRONNING MAUD LAND . . . . .	52
<b>5 CONCLUSION</b>	<b>55</b>
<b>ACKNOWLEDGEMENTS</b>	<b>56</b>
<b>REFERENCES</b>	<b>57</b>
<b>A APPENDIX</b>	<b>63</b>
A.1 DEFORMATION MODEL I . . . . .	63
A.2 DEFORMATION MODEL II . . . . .	63
A.3 DEFORMATION MODEL III . . . . .	64

## ABSTRACT

In this study we examined (i) the stability of the ice sheet in East Dronning Maud Land and Enderby Land where it is drained by a large fast-flowing continental ice stream (Shirase Glacier) and (ii) the regional behavior of the Antarctic ice sheet in East Dronning Maud Land in function of environmental change over a period of the last 200,000 years. Both tasks were accomplished by numerical modeling of the ice sheet system and by satellite remote sensing.

For this purpose, a high resolution two-dimensional time-dependent flow line model was developed, taking into account grounded ice, ice shelf and ice stream mechanics, basal motion and isostatic adjustment. Furthermore the two-dimensional temperature field is calculated and coupled to the flow field. The model is numerically solved on a fine grid, which is unequally spaced both in the horizontal and vertical directions.

An analysis of ice stream dynamics under different basal conditions revealed a thermally regulated cyclic behavior, strongly related to the hydraulic conditions at the bed. Applying this mechanism to Shirase Glacier, a possible explanation is given for the rapid ice sheet thinning which is at present observed in Shirase Drainage Basin. Our modeling experiments showed that this thinning could not be solely attributed to the local imbalance due to Holocene ice sheet retreat.

For the paleo-reconstruction of the ice sheet in East Dronning Maud Land, the model was forced with the climate signal in the past and eustatic sea-level variations. The outcome of the experiments was then compared to the geomorphological evidences on past glacier stands in the Sør Rondane Mountains. Results of the 'best fit' scenario showed that the present ice sheet in the Sør Rondane is close to its maximum position of the last glacial–interglacial period, which corroborates the small differences found between the level of present active and Last Glacial Maximum moraines. The model experiments also indicate glacier variations over the last 200,000 years of the order of 100–150 m, which are however very dependent on the position on the glacier (seaward, inland, inside the mountain range) highlighting the damming effect of the coastal mountains.

Finally a method is presented to infer surface glacier velocities from sequential satellite imagery and successfully applied to the ice fall area of a glacier in the Sør Rondane.

## 1 RESEARCH GOALS

The East Antarctic ice sheet appears as a stable and dominant feature on earth at least for the last few million years. What happened before (Pliocene–Early Pleistocene) is highly questioned and gave rise to three different views (Kennett and Hodell, 1993). The first hypothesis ('stabilist view') holds that the East Antarctic ice sheet remained relatively stable since middle Miocene, experiencing only relatively small ice volume variations. The second hypothesis ('giant ice sheet') suggests an important growth of the Antarctic ice sheet during early Pliocene warmth, while the third hypothesis ('dwarf ice sheet') says that Antarctica experienced major deglaciation during the warmth of the Pliocene.

Also the picture at the end of the Pleistocene has gradually changed. Where twenty years ago the last and penultimate glacial maximum ice sheets were believed to have expanded to the edge of the continental shelf, modern dating techniques and new compelling evidence suggest only small changes. However, during this period temperature changes of 10 K and eustatic sea-level changes of more than 100 m were recorded, implying surface mass balance changes of 50 %. In view of the glacio-geomorphological evidence this implies that these rather important climatic changes had an almost negligible effect on the giant ice mass of East Antarctica.

The main aim of our research is to investigate the dynamic behavior of the East Antarctic ice sheet on a regional scale over the last few  $10^5$  years, taking into account the climatic history and field evidence on past ice sheet stands. This research was carried out in a marginal mountain range, where dated morainic deposits bear witness of former glacier stands. A second part of this investigation encompasses a detailed study on the stability, ice dynamic behavior, and ice stream mechanics in particular of fast flowing outlet glaciers. Both research actions are based on numerical modeling of Antarctic outlet glaciers, i.e. fast flowing continental ice streams and outlet glaciers cutting through a mountain range.

Numerical modeling of ice sheet systems<sup>1</sup> is one of the strategies in studying the time-dependent behavior of ice sheets. Its application has several advantages:

- It allows an understanding of the dynamic behavior of the ice sheet, especially the inter-relation with its boundary conditions, and of the sensitivity of the system with respect to changing boundary conditions.
- It enables to disentangle the relevant physical processes responsible for ice sheet

---

<sup>1</sup>An ice sheet system encompasses the ice sheet s.s. and its boundary conditions, i.e. the outer boundary (ice shelf, ice stream, grounding zone, calving, eustasy), the lower boundary (isostasy, hard and soft bed deformation, hydraulics, basal melting) and the upper boundary (mass balance, surface temperature, climate change)

variations with respect to environmental changes, such as eustasy, isostasy, thermodynamics, basal melting, etc.

- It can yield predictions of the behavior of an ice sheet which can be tested against empirical field evidence. This comparison can be used to validate the model, whether it is possible to reconstruct the known variations of the ice sheet both in space and time. In addition, the model reconstruction can help to fill in the gaps by linking field evidences in space and time.
- Model predictions can guide future expeditions to locations where particular pieces of field evidence might be found in order to elucidate the knowledge on the ice cap's history and its present behavior.

In order to achieve these goals a profound analysis of the dynamic ice flow, marginal ice flow, basal dynamics and mass balance was undertaken, by means of a high resolution numerical model. The purpose of the experiments was twofold: (i) to study the control mechanisms in regional ice sheet stability, especially continental ice streams, and (ii) to investigate the reaction of the ice sheet to the climate signal in the past and in comparison with empirical field evidence. We opted for a high performance model, with an improved numerical computation scheme allowing for variable grid size spacing both in the horizontal and the vertical and with a large degree of freedom: three basic ice deformation models, three fundamental basal motion laws, changing marginal dynamics, and a large variety of 'possible' environmental constraints.

High resolution numerical modeling makes only sense if accurate and detailed data on present surface topography, ice thickness, surface temperature, mass balance and velocities are available. Continuous field work remains therefore indispensable. Besides field surveys, remote sensing is a valuable source for regularly adding data to the rather blank map of Antarctic knowledge, especially in areas which are hardly accessible by man. Therefore, a method is presented to infer glacier surface velocities from sequential satellite images. The result serves both an analysis of the glacier dynamics as well as a validation for ice sheet model outcome.

## 1.1 UNDERSTANDING ICE SHEET SYSTEMS

The dynamic behavior of a large polar ice sheet is well understood: grounded ice flow is basically governed by shearing close to the bed. In its most simplistic form, the basal shear stress equals ice density times gravity times overburden depth times surface slope, which Hutter (1993) defined as the glaciologist's first commandment. However, like any physical system, an ice sheet is not only controlled by its internal dynamics, but also by its boundary conditions, which are less well understood. Environmental processes such as surface temperature and mass balance act as the *upper boundary*



and are in many ice sheet models regarded as the external system forcing. The present environmental conditions thereby serve as a reference.

Basal motion is the major component of the *lower boundary*. The basal velocity depends on the internal ice dynamics, the bedrock conditions and the presence of water at the ice sheet base. Basal velocity will play a role when the temperature of the basal ice is at melting point and will gain more importance close to the margin where it interacts with the margin ice dynamics.

Finally, the *outer boundary* encompasses the outer margin of the ice sheet system. When the ice sheet margin ends at the sea under the form of a floating ice shelf, a transition zone can be defined where the ice sheet dynamics gradually evolve towards ice shelf dynamics. Elaborate studies on this grounding zone revealed that for small basal motion the width of the transition zone is of the same order of magnitude as the ice thickness, so that the grounding zone is reduced to a grounding line and the shallow ice approximation (or the first commandment) still holds, provided that there is no passive grounding of the ice shelf. It suffices to calculate the longitudinal stress deviator along the grounding line and prescribe a longitudinal stress gradient (van der Veen, 1987). Grounding line movement is thus only governed by sheet mechanics (Hindmarsh, 1993). This situation is the most common outer boundary at the edge of the East Antarctic ice sheet where a steep surface slope, characterizing grounded ice, abruptly changes to a small surface gradient where the ice starts floating.

However, large amounts of Antarctic ice are not drained along these margins, but through fast outlet glaciers or ice streams, which are believed to be more sensitive to environmental changes. These ice streams are characterized by large basal velocities, relatively small surface gradients and a low basal traction. The internal ice dynamics involve not only shearing, but longitudinal stretching as well, thus violating the first commandment. In West Antarctica, where ice streams are a common drainage feature, they are able to destabilize the ice sheet, moreover since most of the bedrock elevation lies below sea level.

Also, the East Antarctic ice sheet is at places drained by large ice streams, such as Lambert Glacier, Jutulstraumen, Shirase Glacier or Slessor Glacier, all characterized by large velocities and a small surface gradient in the stream area. Whether these continental ice streams are able to destabilize the East Antarctic ice sheet is not presumed, since most of them have a bedrock lying close or above sea level. However, treating them physically as 'continental ice sheet' would mean the same as ignoring their existence. We therefore performed model experiments with the ice sheet system model in which all relevant stresses (shear, longitudinal, vertical resistive stress) are incorporated. Sensitivity experiments were carried out with different basal boundary conditions for the ice stream area in order to determine the stability of the ice sheet system with changing climate.

## 1.2 PALEO-RECONSTRUCTION AND MODELING

Reconstructing the history of the Antarctic ice sheet poses one of the main challenges to the earth science community and can be considered as a key issue for understanding past and future global change. Field evidence for this purpose comes from two different sources (Figure 1).

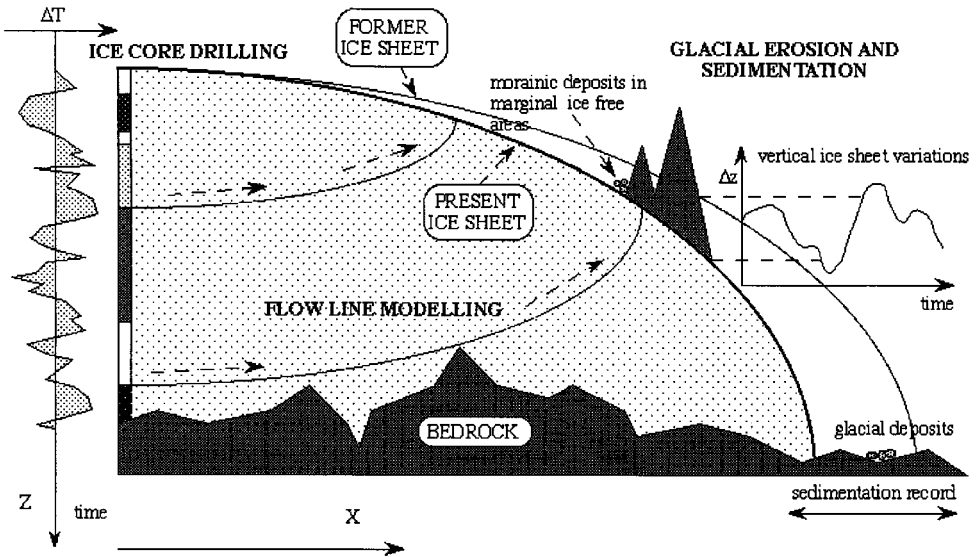


Figure 1: Schematic representation for understanding the glacial history of ice sheets

A first source is the pure climatic evidence, provided by the glaciological community mainly by means of ice core drilling near the center of the ice cap. Up to now nearly all data come from the Vostok ice core, but new ice cores are being undertaken: at Dome F by the Japanese Antarctic Research Expedition (JARE), at dome C and later in West Dronning Maud Land by the European Community (EPICA). These data essentially provide us with variations in temperature, mass balance, air and ice composition in the time domain. A second source is provided by the earth science community and encompasses the geological evidences mainly off shore by seismic stratigraphy and on shore by geomorphological evidences in the ice free areas like the coastal oasis and the marginal mountain ranges. These data indicate the spatial variations of the ice sheet, both in altitude and extent, while also time variations can be inferred.

For a real understanding of the role of the cryosphere, to make sense of and to link the independent observations at the ice divide on the one hand (ice core) and at the marginal areas on the other hand (geological and geomorphological evidence) ice sheet modeling is necessary. In other words climate is different from geology and in 'glacial geology' the transfer function linking climate and geology is the glacier.

All too often in the past simple deductions were made and taken for granted. Climatic variations (Ice Ages) were inferred directly from geological evidences without serious models for the glacier behavior (e.g. Hollin, 1962; Denton and Hughes, 1981). Today dynamic modeling should be capable of providing physical constraints to the deduction of ice sheet variations from the observations as made on the ice divide and in the marginal areas. We therefore applied high resolution numerical ice sheet modeling in order to simulate the ice sheet behavior over the last 200,000 years under different boundary conditions of sea-level forcing, basal mechanics and thermodynamics. By comparing the different model simulations with geomorphological data on former glacier stands, it was possible to disentangle the relevant physical processes responsible for ice sheet variations in East Dronning Maud Land, Antarctica.

## 2 MATERIALS AND METHODS

### 2.1 THE ICE SHEET SYSTEM MODEL (ICE2D)

This numerical ice sheet system model is a dynamical flow line model that predicts the ice thickness distribution along a flow line in space and time in response to environmental conditions, based on the calculation of the two-dimensional flow regime (velocity, strain-rate and stress fields) and the temperature distribution. It is one of the most complete two-dimensional ice sheet models in use, extended with a large number of basal boundary models, such as basal water flow, sliding and bed deformation, and an ice shelf model as outer boundary condition.

A Cartesian co-ordinate system  $(x, z)$  with the  $x$ -axis parallel to the geoid and the  $z$ -axis vertically pointing upward ( $z = 0$  at sea level) is defined. Starting from the known bedrock topography and surface mass balance distribution, and assuming a constant ice density, the change of ice thickness along the flow line is predicted as

$$\frac{\partial H}{\partial t} = -\frac{1}{b} \frac{\partial(UHb)}{\partial x} + M - S \quad (1)$$

with  $U$  the depth averaged horizontal velocity [ $\text{m a}^{-1}$ ],  $H$  the ice thickness [ $\text{m}$ ],  $M$  the surface mass balance [ $\text{m a}^{-1}$  ice equivalent], and  $S$  the melting rate at the base of the ice sheet [ $\text{m a}^{-1}$ ]. Divergence and convergence of the ice flow are taken into account in the calculation of the variation of the ice flux along the flow line through  $b$  defining the width of the flow band and taken perpendicular to the flow line. Boundary conditions to the ice sheet system are zero surface gradients at the ice divide and a moving margin or ice shelf at the seaward side, depending on the flotation criterion, basal melting rate and surface ablation.

#### 2.1.1 Ice Deformation

The major assumption made in the model formulation is to consider plane strain, so that all stress components involving  $y$  are neglected. Consider furthermore that the ice sheet experiences no shear at its sides ( $\tau_{xy} = 0$ , a point which will be taken up later), the three-dimensional Euler continuum is written as

$$\frac{\partial \tau_{xx}}{\partial x} + \frac{\partial \tau_{xz}}{\partial z} = 0 \quad (2)$$

$$\frac{\partial \tau_{xz}}{\partial x} + \frac{\partial \tau_{zz}}{\partial z} = \rho g \quad (3)$$

with  $\tau_{ij}$  the full stress components,  $\rho$  the ice density [ $910 \text{ kg m}^{-3}$ ], and  $g$  the gravitation constant [ $9.81 \text{ m s}^{-2}$ ]. Following Whillans (1987) and van der Veen and Whillans (1989), the full stresses ( $\tau_{ij}$ ) are separated into lithostatic ( $L$ ) and resistive ( $R$ ) components. The lithostatic component describes the effect of gravity pulling ice forward,

whereas resistive components oppose glacial motion.

$$\tau_{ij} = R_{ij} + \delta_{ij}L \quad (4)$$

with  $L = -\rho g(H + h - z)$  and  $\delta_{ij}$  the Kronecker-delta ( $\delta_{ij} = 1$  if  $i = j$  and equals 0 otherwise). Furthermore, deviatoric stresses are related to the full stresses as

$$\tau_{ij} = \tau'_{ij} + \delta_{ij}P \quad (5)$$

where  $P = (\tau_{xx} + \tau_{yy} + \tau_{zz})/3$  is the spherical stress. For plane flow it follows that  $\tau'_{yy} = 0$ , so that  $\tau'_{xx} = -\tau'_{zz}$ . After some arithmetic manipulation, the following expression can be derived from Eq.(4) and (5).

$$\tau_{ij} = \tau'_{ij} + \delta_{ij}(\tau'_{xx} + R_{zz}) - \delta_{ij}\rho g(H + h - z) \quad (6)$$

Thus, inserting Eq.(6) in Eq.(2) and (3) and integrating from the surface of the ice sheet  $H + h$  to a height  $z$  results in an expression for the shear stress and the vertical resistive stress respectively.

$$\begin{aligned} \tau'_{xz}(z) &= 2 \int_z^{H+h} \frac{\partial \tau'_{xx}}{\partial x} dz + \tau_d \left( \frac{H + h - z}{H} \right) + \\ &+ \tau'_{xz}(H + h) + \int_z^{H+h} \frac{\partial R_{zz}}{\partial x} dz \end{aligned} \quad (7)$$

$$R_{zz}(z) = \int_z^{H+h} \frac{\partial \tau'_{zz}}{\partial x} dz + R_{zz}(H + h) \quad (8)$$

where  $\tau_d = -\rho g H \partial(H + h)/\partial x$  is the driving stress. For modeling of valley glaciers a shape factor  $F$  is introduced, so that  $\tau_{xz} = F \tau'_{xz}$ , taking into account the effect of valley wall friction, since  $\tau_{xy} \neq 0$ . Values for this shape factor depend on the cross-section form and the height-to-width ratio (Nye, 1965; Paterson, 1994).

If both longitudinal stress gradients and the vertical resistive stress are neglected, the shear stress at the base of the ice sheet in Eq.(7) equals the driving stress. This is the most common stress expression that can be found in large scale ice sheet models (e.g. Huybrechts and Oerlemans, 1988). Boundary conditions for the above equations are a stress free surface.

$$\tau'_{xz}(H + h) - (2\tau'_{xx}(H + h) + R_{zz}(H + h)) \frac{\partial(H + h)}{\partial x} = 0 \quad (9)$$

$$R_{zz}(H + h) - \tau'_{zz}(H + h) \frac{\partial(H + h)}{\partial x} = 0 \quad (10)$$

### 2.1.2 Strain-Rates and Velocities

For an isotropic ice mass that deforms under steady-state creep, the constitutive equation, relating the deviatoric stresses to the strain-rates (which are per definition related

to velocities) can in the case of plane strain be expressed as (Paterson, 1994)

$$\begin{aligned}\dot{\epsilon}_{ij} &= A(T^*)\tau_e^{n-1}\tau'_{ij} \approx A(T^*)\left(\tau_{xx}^{\prime 2} + \tau_{xz}^{\prime 2}\right)^{(n-1)/2}\tau'_{ij} \\ &= \frac{1}{2}\left[\frac{\partial u_i}{\partial x_j} + \frac{\partial u_j}{\partial x_i}\right]\end{aligned}\quad (11)$$

where  $u_i$  and  $u_j$  are the velocity components,  $n$  the flow law exponent ( $n = 3$  in the experiments described below) and  $A(T^*)$  a flow parameter depending on impurities in the ice, on crystal fabric and on ice temperature, corrected for the dependence of the melting point on pressure ( $T^* = T + 8.7 \cdot 10^{-4}(H + h - z)$ , with  $T$  the ice temperature [K]). An Arrhenius relationship for  $A(T^*)$  is adopted from Paterson (1994)

$$A(T^*) = m a \exp\left[\frac{-Q}{RT^*}\right] \quad (12)$$

where  $a = 1.14 \cdot 10^{-5} \text{Pa}^{-n} \text{a}^{-1}$  and  $Q = 60 \text{ kJ mol}^{-1}$  for  $T^* < 263.15 \text{ K}$ , and  $a = 5.74 \cdot 10^{10} \text{Pa}^{-n} \text{a}^{-1}$  and  $Q = 139 \text{ kJ mol}^{-1}$  for  $T^* \geq 263.15 \text{ K}$ .  $m$  is a tuning parameter taking into account the unknown factors such as crystal fabric, impurity content etc. Basically, from Eqs.(7) to (10) the two-dimensional stress field can be derived, and the horizontal velocity field is obtained through integration from the bottom of the ice sheet to a height  $z$  of Eq.(11). Integrating once more results in the vertical mean horizontal velocity which enters the continuity equation (Eq.1). An expression for the vertical velocity is obtained from the incompressibility condition, i.e.  $\partial w/\partial z = -\partial u/b\partial x$ . For the determination of the two-dimensional flow field, three different models were developed, i.e. Deformation Models I to III with an increasing degree of sophistication. Deformation Model III calculates the complete stress field as described in the above stress and strain equations; Deformation Model II neglects the vertical resistive stresses and simplifies the flow law Eq.(11) to  $\dot{\epsilon}_{xz} = \frac{1}{2}\partial u/\partial x$ , and Deformation Model I neglects, besides the simplifications made in Deformation Model II, the longitudinal deviatoric stresses. A detailed reference to the derivation of the flow field for the three deformation models is given in the Appendix.

### 2.1.3 Thermodynamics

The temperature distribution in an ice sheet is governed by diffusion, friction and advection, and is therefore dependent not only on boundary conditions such as surface temperature and geothermal heat flux, but also on ice velocity. The thermodynamic equation can thus be written as (Huybrechts and Oerlemans, 1988; Ritz, 1989)

$$\frac{\partial T}{\partial t} = \frac{k_i}{\rho c_p} \frac{\partial^2 T}{\partial z^2} - u \frac{\partial T}{\partial x} - w \frac{\partial T}{\partial z} + \frac{\Phi}{\rho c_p} \quad (13)$$

with  $T$  the ice temperature [K], and  $k_i$  and  $c_p$  the thermal conductivity and the specific heat capacity respectively, defined as  $k_i = 3.101 \cdot 10^8 \exp(-0.0057T)$  and  $c_p = 2115.3$

+ 7.79293 ( $T - T_0$ ), with  $T_0 = 273.15$  K the absolute temperature (Huybrechts, 1992). The heat transfer is thus a result of vertical diffusion (horizontal diffusion is neglected because it is small compared to the vertical diffusion), horizontal and vertical advection and internal friction due to deformational heating. The internal heating rate per unit volume is given by (Paterson, 1994)

$$\begin{aligned}\Phi &= \sum_{ij} \dot{\epsilon}_{ij} \tau_{ij} \approx \dot{\epsilon}_{xx} \tau_{xx} + 2\dot{\epsilon}_{xz} \tau_{xz} \\ &\approx \tau'_{xx}(z) \frac{\partial u}{\partial x} + \tau'_{xz}(z) \frac{\partial u}{\partial z}\end{aligned}\quad (14)$$

In most ice sheet models longitudinal strain rates are neglected, because they seem small compared to shear strain rates. However, since we will carry out a study on ice stream behavior the heating effect caused by  $\partial u / \partial x$  might not be neglected. Boundary conditions follow from the annual mean air temperature at the surface, and the geothermal heat flux (enhanced with heat from basal motion) at the base

$$\left( \frac{\partial T}{\partial z} \right)_{base} = \gamma_g - \frac{\tau_b u(h)}{k_i} \quad (15)$$

where  $\gamma_g$  [ $\text{K m}^{-1}$ ] is the geothermal heat entering the ice expressed as a temperature gradient, and the second term on the right-hand side the heat surplus caused by basal motion. The geothermal heating can take two forms, depending on whether or not heat conduction in the bedrock below is considered.

$$\begin{aligned}\gamma_g &= \frac{G}{k_i} \quad \text{without bedrock heat conduction} \\ &= \frac{k_r}{k_i} \left\{ \frac{\partial T}{\partial z} \right\}_r \quad \text{with bedrock heat conduction}\end{aligned}\quad (16)$$

where  $G = -54.6 \text{ mW m}^{-2}$  is the geothermal heat flux corresponding to 1.30 HFU (Heat flow Units) (Sclater et al., 1980) and  $k_r$  the thermal conductivity of rock [ $k_r = 1.041 \cdot 10^8 \text{ Jm}^{-1}\text{K}^{-1}\text{a}^{-1}$ ] (Turcotte and Schubert, 1982). As shown by Ritz (1987) and Huybrechts (1992), taking into account the effect of thermal conductivity in the bedrock may seriously damp the basal temperature response for climatic oscillations operating on longer time scales. For the calculation of the heat transfer in the underlying bed, only vertical diffusion is considered in a rock slab of 2000 m thickness divided into 5 equally spaced layers. The temperature change in time is written as

$$\frac{\partial T_r}{\partial t} = \frac{k_r}{\rho_r c_r} \frac{\partial^2 T_r}{\partial z^2} \quad (17)$$

where  $T_r$  is the rock temperature [K],  $\rho_r$  the rock density [ $3300 \text{ kg m}^{-3}$ ], and  $c_r$  the specific heat capacity [ $1000 \text{ J kg}^{-1}\text{K}^{-1}$ ]. The lower boundary is defined as the geothermal heat flux entering through the base of the considered rock slab. At the upper surface,

boundary conditions follow from the basal ice temperature and the basal temperature gradient.

The basal temperature in the ice sheet is kept at pressure melting point whenever it is reached, and the surplus energy is used for melting. This may, in some cases, lead to the formation of a temperate ice layer between  $\zeta = 1$  and  $\zeta = \zeta_{melt}$ , so that the basal melt rate  $S$  is defined as

$$S = \frac{k_i}{\rho L} \left[ \left( \frac{\partial T}{\partial z} \right)_c - \left( \frac{\partial T}{\partial z} \right)_b \right] + \frac{1}{\rho L} \int_h^{z_{melt}} \Phi dz \quad (18)$$

where index  $b$  denotes the basal temperature gradient as given in Eq.(15) and index  $c$  the basal temperature gradient after correction for pressure melting. In the ice shelf, the vertical temperature profile is taken linearly with the surface temperature as the upper boundary condition and a constant temperature of  $-2^\circ\text{C}$  at the bottom of the ice shelf.

#### 2.1.4 Isostatic Bedrock Adjustment

Bedrock adjustment to the ice load is calculated as described in Brochie and Silvester (1969). The elastic properties of the lithosphere determine the ultimate bedrock depression. The deflection at a normalized distance  $x = r/L$  from the point load can be written as

$$w(x) = \frac{qL^2}{2\pi D_r} \text{kei}(x) \quad (19)$$

with  $\text{kei}(x)$  a Kelvin function of zero order,  $r$  the real distance from the load  $q$ ,  $D_r$  the flexural rigidity [ $10^{25}\text{Nm}$ ], and  $L$  the radius of relative stiffness ( $L = (D_r/\rho_r g)^{1/4}$ ). The viscosity of the underlying asthenosphere determines the relaxation time. The time dependent response is modeled by a simple relaxation, which performs better than the diffusion model (Le Muer and Huybrechts, 1996)

$$\frac{\partial h_b}{\partial t} = -\frac{1}{\Theta}(w - h) \quad (20)$$

with  $\Theta$  the characteristic time scale of 3000 a.

#### 2.1.5 Basal Motion

For modeling purposes, the full stress field in an ice sheet system, which consists of a grounded ice sheet, its grounding zone or stream area and a coupled ice shelf, is derived from a basal boundary condition. The calculation of the two-dimensional ice velocity field is thus reduced to a one-dimensional problem, in which the basal sliding mechanism in the ice sheet, the stream flow mechanism and the ice shelf flow needs to be determined. Since the basal boundary condition is iteratively updated with the derivation of the two-dimensional flow field, the final solution is a two-dimensional one.



The ice shelf is simply taken as a freely floating ice shelf bounded in a parallel-sided bay, so that all stresses in the  $y$ -direction can be set to zero. Vertical shearing is omitted, so that the force balance equation reduces to

$$2 \frac{\partial(H\bar{\tau}'_{xx})}{\partial x} = \rho g H \frac{\partial(H+h)}{\partial x} \quad (21)$$

In order to calculate the longitudinal deviatoric stress from this equilibrium, its value at the seaward edge of the shelf must be known. Here, the total force of the ice must be balanced by the sea water pressure, so that (Thomas, 1973)

$$\tau'_{xx}(e) = \bar{\tau}'_{xx}(e) = \frac{1}{4} \rho g H \left( 1 - \frac{\rho}{\rho_s} \right) - \sigma_b \quad (22)$$

where  $\rho_s$  is the density of sea water [ $1028 \text{ kg m}^{-3}$ ] and  $\sigma_b$  the ice shelf backpressure. Using Eq.(22) to calculate the longitudinal stress deviator at the edge of the ice shelf, Eq.(21) is then integrated upstream to yield the longitudinal deviatoric stress in the whole ice shelf. Once the vertical mean horizontal velocity at the grounding line is known, the vertical mean horizontal ice shelf velocity (which equals the basal velocity) is calculated from the definition of the normal strain-rates and the constitutive relation Eq.(11)

$$\dot{\epsilon}_{xx} = \frac{\partial u}{\partial x} = A(T^*) \tau_{xx}^m \quad (23)$$

The temperature dependent flow law parameter  $A(T^*)$  is taken as a constant in the whole ice shelf, based on the mean ice shelf temperature.

Basal motion of the grounded ice sheet can originate from sliding of the ice over its bed and deformation of the bed itself, the latter if the bed consists of sediments saturated with water at a pressure that closely matches the ice overburden pressure. Sliding is thus only expected where the basal ice is at melting point (Paterson, 1994). In polar ice streams, the origin of basal water is most likely due to basal melting primarily caused by strain heating. Percolation of surface melt water and the formation of intra-glacial channels and moulins might thus be neglected. In most basal motion laws, derived from laboratory experiments and data fitting from observed values, basal motion is a function of the shear stress at the base, bed roughness and the effective normal pressure at the base, the latter equalling the ice overburden pressure minus the water pressure at the base of the ice sheet. A general sliding law has the form of (Bindschadler, 1983; Budd et al., 1984; Budd and Jenssen, 1987; van der Veen, 1987)

$$u_s = A_s \tau_b^p N^{-q} \exp [v(T^* - T_0)] \quad (24)$$

where  $p$  and  $q$  are positive numbers ranging between 0 and 3 and the exponential term a correction for the basal temperature, introduced by Budd and Jenssen (1987).  $N$  is the effective normal pressure at the base. For glaciers that terminate in the sea,

subglacial water pressure at the grounding line may be calculated from the flotation criterion, so that the effective normal pressure  $N$  is proportional to the height of the glacier surface above buoyancy.

$$N = p_i - p_w = \rho g H + \rho_s g (h_b - H_{sl}) \quad (25)$$

with  $H_{sl}$  the sea level height compared to the present sea level (datum) and  $p_i$  and  $p_w$  the ice and water pressure respectively. In some flow models of the Antarctic ice sheet (Budd *et al.*, 1984; Huybrechts, 1990), the effective normal pressure is calculated in the same fashion over the whole model domain and not only at the grounding line. However, the physical restriction is that the bedrock should lie beneath sea level and that the water pressure originates from sea water infiltrating at the grounding line and moving in the upstream direction. Since this type of parameterization is widely used in ice sheet models, it is adopted for the calculation of sliding type 2 and 5 in Table 1.

Subglacial water pressure or the pressure gradient underneath the ice sheet can be derived from the existence of subglacial channels and/or cavities. Bindschadler (1983) applied the so-called Röttlisberger-channels (Röttlisberger, 1972) for the derivation of effective normal pressure in Antarctic ice streams. The theory and physical background of the formation of channels and cavities is very complicated and highly dependent on the detailed bedrock topography. Since basal conditions in the Dronning Maud Land area are hardly known, the use of such physical principles remains highly speculative.

A more straightforward treatment of the basal water flow is to consider a water film underneath the ice sheet. According to Weertman and Birchfield (1982), the sliding velocity is dependent on the depth of the water layer  $\delta$  and the critical particle size  $\delta_c$ .

$$\begin{aligned} u_s &= A_s \tau_b^p \left( 1 + 10 \frac{\delta}{\delta_c} \right) & \text{if } \delta < \delta_c \\ &= 10 A_s \tau_b^p \frac{\delta}{\delta_c} & \text{if } \delta \geq \delta_c \end{aligned} \quad (26)$$

and

$$\delta = \left( \frac{12 \mu Q_w}{P_g} \right)^{\frac{1}{3}} \quad (27)$$

where  $Q_w$  is the water flux per unit width [ $\text{m}^2 \text{s}^{-1}$ ], calculated through downstream integration of the basal melting rate, and  $P_g$  the pressure gradient (Alley, 1989).

In the analysis above, the glacier moves over an undeformable bed, and the water acts as a lubrication layer between the bedrock and the ice. However, in the presence of subglacial till it is very likely that, whenever this till layer becomes saturated, the drainage is along the till and/or bed (Walder and Fowler, 1994). When the till layer is sufficiently thick, deformation of the till layer (bed deformation) can occur (Alley, 1989). Combination of all these processes (cavities in ice and till, subglacial aquifers) obviously make the basal motion mechanism very complicated. Nevertheless, Alley *et al.*

Table I: Constants and parameters for the different basal velocity laws

Type	$U_s$ law	$N$	$A_s$	$p$	$q$	$v$	$\delta_c$
1	Eq.(26)	—	$1.5 \cdot 10^{-1}$ [m a <sup>-1</sup> ]	0	—	—	$10^{-4}$ [m]
2	Eq.(24)	Eq.(25)	$5.0 \cdot 10^9$ [N m <sup>-1</sup> a <sup>-1</sup> ]	1	2	0.1	—
3	Eq.(24)	Eq.(28)	$0.8 \cdot 10^5$ [Pa <sup>0.47</sup> ma <sup>-1</sup> ]	1.33	1.8	0.0	—
4	Eq.(26)	—	$2.0 \cdot 10^{-11}$ [Pa <sup>-2</sup> m <sup>-1</sup> a <sup>-1</sup> ]	2	—	—	$10^{-4}$ [m]
5	Eq.(24)	Eq.(25)	$2.0 \cdot 10^{-7}$ [N <sup>-2</sup> m <sup>5</sup> a <sup>-1</sup> ]	3	1	—	—

(1989) incorporated in a simplified way the bed deformation. Neglecting the shear strength of the till and setting the effective pressure  $N$  independent of depth, the bed deformation velocity then takes the form of the sliding velocity Eq.(24) without the exponential term. The effective pressure  $N$  is calculated as (Alley et al., 1989)

$$N = \frac{\beta \tau_b}{1 + 0.1 \log_{10} \delta} \quad (28)$$

where the denominator represents the fraction of the bed occupied by the water film with depth  $\delta$ , and  $\beta$  a geometric constant related to the bed roughness ( $\beta \approx 2.0$  in the analysis of (Alley et al., 1989)). In total we considered five basal velocity laws, based on three different basal motion concepts: (i) basal sliding related to basal shear stress and effective normal pressure at the bed, (ii) sliding due to the presence of a water film, and (iii) till deformation at the ice–bed interface. The coefficients for the different basal motion laws are given in Table I.

### 2.1.6 Numerical Computation

The ice sheet system model is numerically solved on an irregular grid both in the horizontal and the vertical. This does not mean that we introduced the complexity that is overcome with finite element models or multi-grid approaches. The irregular grid system is an approximation to the finite difference system. Experiments showed that grid size changes (larger grid sizes) are acceptable in slow moving areas characterized by a small surface slope, such as the interior ice sheet. The nominal grid size should however be maintained in the regions of high shear, the grounding area and the ice shelf. Introducing such a variable grid size seriously alters the model performance in terms of computation time. The calculation of the first and second derivatives are thus

approximated as

$$\begin{aligned}\frac{\partial f}{\partial x} &\approx \frac{f_{i+1} - f_{i-1}}{x_{i+1} - x_{i-1}} \\ \frac{\partial^2 f}{\partial x^2} &\approx \frac{2}{x_{i+1} - x_{i-1}} \left[ \frac{f_{i+1} - f_i}{x_{i+1} - x_i} - \frac{f_i - f_{i-1}}{x_i - x_{i-1}} \right]\end{aligned}\quad (29)$$

As in dynamic meteorology, the velocity field, stress field and thermodynamic equation are not integrated on a fixed vertical grid in space, as the lower and upper boundary conditions, dependent on ice thickness will not coincide with grid points. Therefore, a scaled co-ordinate system was introduced with 21 layers in the vertical (see Appendix).

Because of the non-linear nature of the velocity in the ice sheet, the continuity equation (Eq.1) is reformulated as a non-linear partial differential equation and written as:

$$\frac{\partial H}{\partial t} = \frac{1}{b(x)} \frac{\partial}{\partial x} \left[ b(x) D(x) \frac{\partial (H + h)}{\partial x} \right] + M - S \quad (30)$$

with  $D(x)$  a diffusion coefficient which, in the grounded ice sheet, equals the mass flux ( $UH$ ) divided by the surface gradient. A solution to this equation can be obtained by writing Eq.(30) in its conservation form (Mitchell and Griffiths, 1980). For the numerical computation a semi-implicit scheme was applied, and new ice thicknesses on the next time step were found by the solution of a tridiagonal system of equations. An implicit numerical scheme (only for the vertical) was adopted for the ice and rock temperature field, resulting in a similar set of tridiagonal equations.

## 2.2 GLACIER SURFACE VELOCITY FROM SEQUENTIAL SPOT IMAGERY

### 2.2.1 Introduction

Understanding and monitoring the present and future behavior of ice sheets and glaciers is one of the prime issues in glaciology. Environmental modeling of ice sheets is one aspect, but the repeatedly gathering of data such as mass balance, temperature, surface and basal topography, velocity, etc. is necessary to feed glaciological models as well as to monitor changes in the present behavior of ice masses.

Velocity measurements of the Antarctic ice sheet are at present very scarce, but crucial to understanding the present flow regime of the ice sheet and outlet glaciers. Conventional methods in the collection of glacier velocity data, such as stake measurements, are rather time consuming, and demand a lot of field work. Moreover, measurements can only be carried out at places which are accessible to man, which do not always coincide with the zones of glaciological interest. The recent application of computer image-matching algorithms to sequential satellite imagery of ice stream areas (Bindschadler and Scambos, 1991; Scambos and Bindschadler, 1993) has for instance greatly increased the ability to determine the large-scale velocity field of ice

streams. Such a method for deriving glacier velocities in the ice fall area of outlet glaciers in Dronning Maud Land is presented here, based on the computer image-matching algorithm of Pattyn (1992), using sequential multispectral SPOT images. A detailed reference is found in Willaert (1995). The applied method consists of four main parts: (i) a precise co-registration of both images using reference points on rock outcrops, (ii) the selection of corresponding points on the glacier surface in the two images by using an image matching algorithm, (iii) the calculation of surface velocities from the horizontal displacement of matched features over time and (iv) verification of the results.

### 2.2.2 The Image Matching Technique

Computer-based image-matching is at present a well known technique in digital photogrammetry, robotics and medical image processing. It is devised to detect automatically corresponding points in two images of the same object or space. An area-based matching method, based on the principle of cross-correlation, is used. Defining the first image as the Target image, and the second image as the Search image, the cross-correlation between an  $(N \times M)$  array of pixel gray values surrounding pixel  $i$  of line  $j$  in the target image (Figure 2) and an  $(N \times M)$  array surrounding pixel  $i'$  of line  $j'$  in the search image is calculated to determine if  $(i, j)$  and  $(i', j')$  are conjugate match points.

For a target array centered along a particular pixel, a search array seeks a conjugate point by moving over a predefined search space (Figure 2). The maximum correlation coefficient of all searches refers to the corresponding point. Defining  $T_{ij}$  and  $S_{ij}$  as the gray values corresponding to the pixel at location  $(i, j)$  in the Target and Search image respectively, the correlation coefficient is calculated as (e.g. Ungar et al., 1988; Pattyn, 1992)

$$R^2 = \frac{\sigma_{TS}^2}{\sigma_{TT}\sigma_{SS}} \quad (31)$$

$$\sigma_{TS} = \sum_{k=-K}^K \sum_{l=-L}^L [T_{i+k,j+l} S_{i'+k,j'+l}] - [N M \bar{T} \bar{S}] \quad (32)$$

$$\sigma_{TT} = \sum_{k=-K}^K \sum_{l=-L}^L [T_{i+k,j+l}]^2 - [N M \bar{T}^2] \quad (33)$$

$$\sigma_{SS} = \sum_{k=-K}^K \sum_{l=-L}^L [S_{i'+k,j'+l}]^2 - [N M \bar{S}^2] \quad (34)$$

where

$$\bar{T} = \frac{1}{N M} \sum_{k=-K}^K \sum_{l=-L}^L [T_{i+k,j+l}] \quad (35)$$

$$\bar{S} = \frac{1}{N M} \sum_{k=-K}^K \sum_{l=-L}^L [S_{i'+k,j'+l}] \quad (36)$$

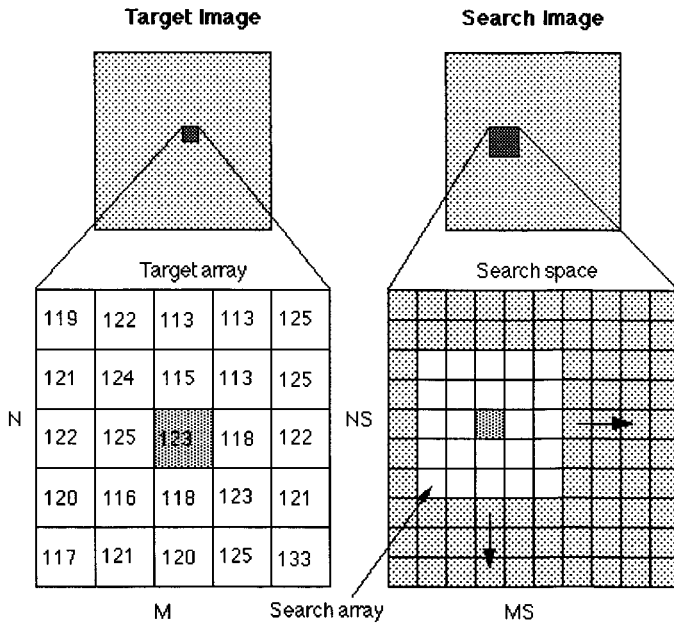


Figure 2: Detail of the image matching process for the automatic detection of corresponding points in two images of the same object or space

and  $K = (N + 1)/2$ ,  $L = (M + 1)/2$ , with  $N$  and  $M$  the size of the target and search arrays, both odd numbers.

Correlations are performed for each target pixel  $T_{ij}$  within a given search space, so that a matrix or correlation map of  $NS$  by  $MS$  correlation coefficients is obtained. The pixel position  $(i', j')$  that coincides with the maximum of these correlation coefficients is the corresponding point. From the correlation map, a variety of correlation statistics are computed to evaluate the match, such as the maximum correlation coefficient, the number of correlation peaks, mean and variance of the correlation surface, the difference between the highest correlation coefficient and the mean of the correlation surface (peak-above-mean), and the difference between the highest and second highest correlation coefficient (peak-above-second-peak). The overall accuracy is further increased by calculating the corresponding points at sub-pixel accuracy by fitting a bi-quadratic function to the correlation coefficients in the neighborhood of the maximum (Rosenholm, 1985). The location of the maximum of this function (to  $\pm 0.1$  pixel accuracy) is the reported match location.

### 2.2.3 Precise Image Co-Registration

Compared to other satellite image sources, the SPOT satellite and its products offer a number of geometric advantages with respect to cartographic processing. The main advantage is the stereo-capability which makes it possible (i) to view a certain area of interest more often in time and (ii) to reconstruct the surface topography based on images taken from a different viewing angle. However, the latter capability forms a disadvantage for the kind of information we would like to extract, since two images of the same area will always be characterized by a parallax distortion due to small differences in viewing angle (vertical images are scanned with a viewing angle between  $-5^\circ$  and  $+5^\circ$ , the resulting value chosen by the instrument and not on user demand) further enhanced by the accidented relief. Prior to the extraction of corresponding points on the glacierized surface (which allows to determine the surface velocity from the horizontal displacement), the two images should be co-registered perfectly on rock outcrops and nunataks, non-movable features over time. A transformation from pixel co-ordinates from one image into the reference system of the other image requires the selection of a number of corresponding points sampled on rock outcrops. Based on this selection a transformation relationship is established so that each pixel of one image is warped into the reference system of the other by means of a resampling. Most available co-registration algorithms are based on global transformations, i.e. two polynomial functions (one for the  $x$ - and one for the  $y$ -co-ordinate) are determined for the transformation of the whole image. Obviously, the more accidented the terrain and the accompanied distortion the more difficult it becomes to accurately describe the spatial error simply by two polynomials. We therefore opted for a local transformation in which all reference points (in the two images) are linked by a network of triangles (triangulation). A point lying in a triangle is transformed by a local transformation of first degree of that particular triangle instead of the whole image. The method has two main advantages: (i) pixels coinciding with reference points are exactly mapped and (ii) the more reference points used, the denser the network and the higher the obtained accuracy. An accurate extraction of reference points in two images is achieved with the image matching technique, in which only points on rock outcrops were used for the triangulation purpose.

### 3 RESULTS

#### 3.1 DATA SAMPLING AND ENVIRONMENTAL FORCING

The primary input for the model is the bedrock and ice surface profile sampled along a flow line. Except for the experiments described in section 3.2, data were sampled from the oversnow traverses carried out in East Dronning Maud Land and Enderby Land (Figure 3). For the construction of the Shirase Glacier flow line (see section 3.3) ice

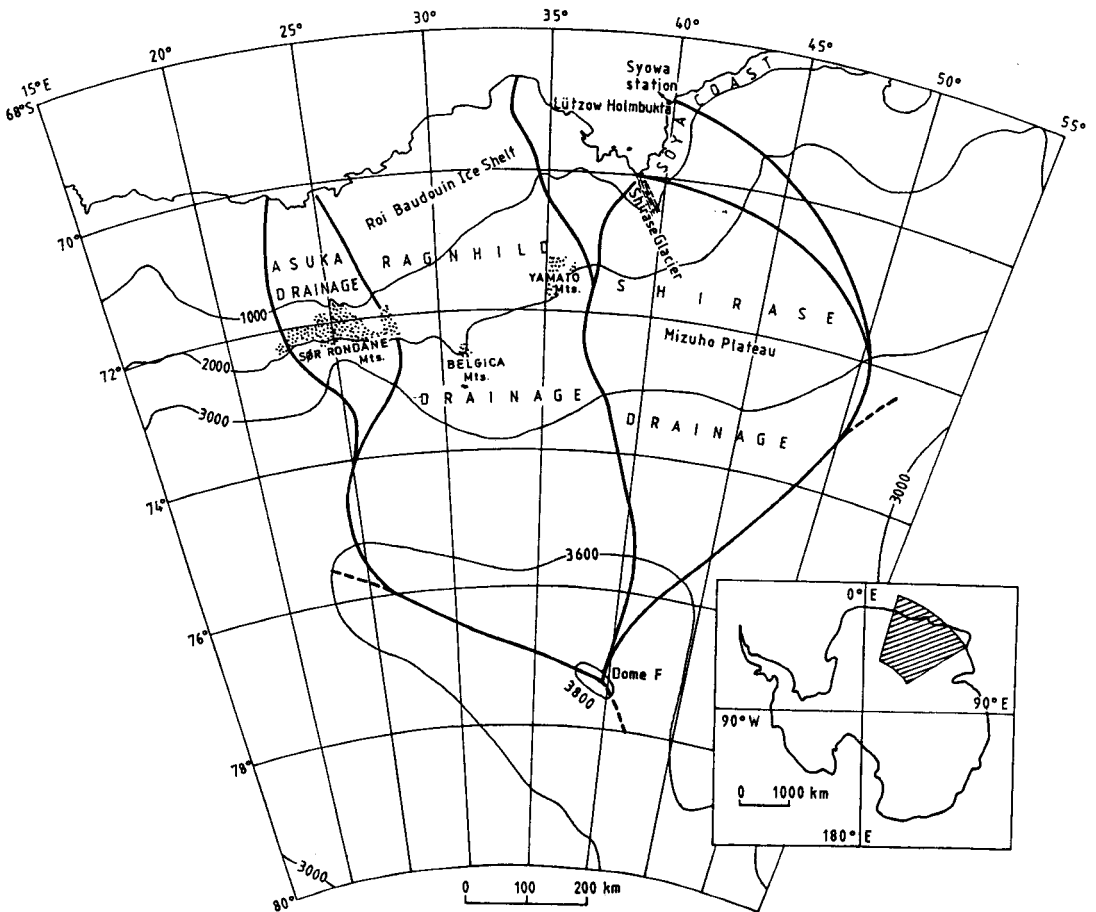


Figure 3: Situation map of East Dronning Maud Land and Enderby land displaying the major drainage basins of the ice sheet

thickness data are obtained from the oversnow traverses from Syowa Station to Dome F during the 1992 field season (Kamiyama *et al.*, 1994) and smaller traverses in the area (Watanabe *et al.*, 1992). Detailed subglacial reference in the stream region was compiled after Mae and Yoshida (1987) and in the ice shelf area after Moriwaki and



Yoshida (1983). These data were sampled with an approximate grid size of 10 km, leading to a flow line of about 1200 km in length. Convergence and divergence of the ice flow was digitized from the topographic map of the region (Ageta *et al.*, 1995) by drawing two flow lines at each side of the central flow line and measuring in each grid point the flow band width ( $b$  in Eq.(1) on page 7) perpendicular to the central line.

For the Asuka Drainage Basin, a flow line was drawn starting at Dome F, entering the Sør Rondane Mountains through the outlet glacier Gjelbreen and continuing north to the coast, beyond the edge of the continental shelf. The outlet glacier Gjelbreen (not shown on Figure 3) cuts along the 25°E meridian through the Sør Rondane Mountain range in a south–north direction. Data on bedrock and surface topography were extracted from Nishio *et al.* (1995) and Ageta *et al.* (1995) in the plateau area and the zone between the mountains and the coast and from Pattyn and Declair (1995b) in the mountain area.

From 79 measurements of 10 m snow depth temperatures (Satow and Kikuchi, 1995) ranging from an elevation of 250 m to 3760 m a.s.l. in Shirase and Asuka Drainage Basin, the present surface temperature could be determined. The mean annual surface mass balance was obtained from snow pit observations measured by the gross  $\beta$ -profile method (Takahashi and Watanabe, 1995). The resulting data sets are visualized in Figure 4.

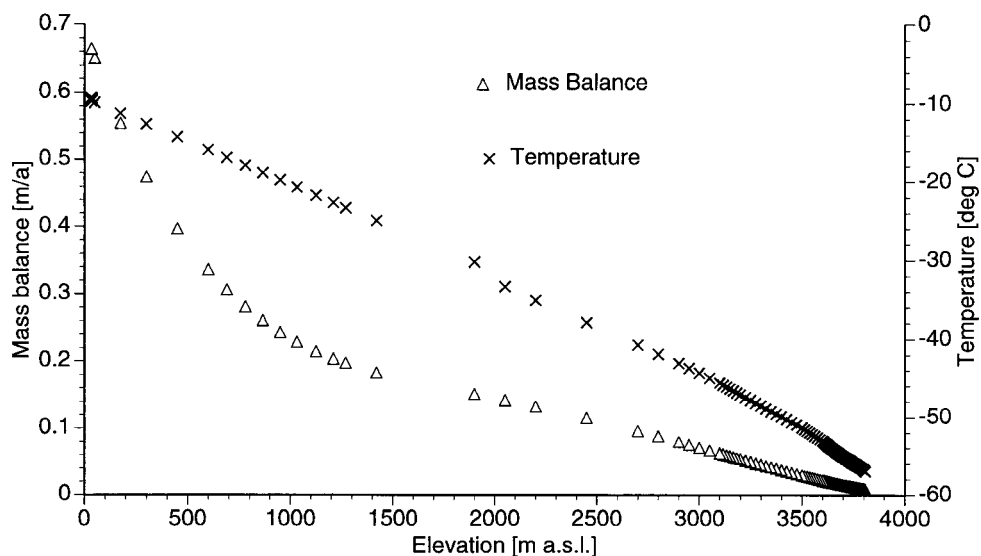


Figure 4: Present surface temperature and mass balance distribution in East Dronning Maud and Enderby Land as adopted for modeling experiments

For each flow line the point measurements on surface and bedrock topography, flow line width, shape factor, surface mass balance and temperature were listed as a

function of their position along the flow line. In order to obtain a complete flow line data set, a cubic spline and Lagrange polynomial interpolation was applied. Sampling for the Asuka flow line and the Shirase flow line was performed on a 10 km grid.

Although we ignore at present the precise environmental conditions reigning in East Dronning Maud Land during the last glacial stage and beyond, the proximity to the central ice divide suggests the use of climatic forcing similar to that found for the Vostok ice core (Figure 5, Jouzel *et al.* (1993)). Drilling experiments are at present being carried out at Dome F and the climatic record will only be available in a few years. Dur-

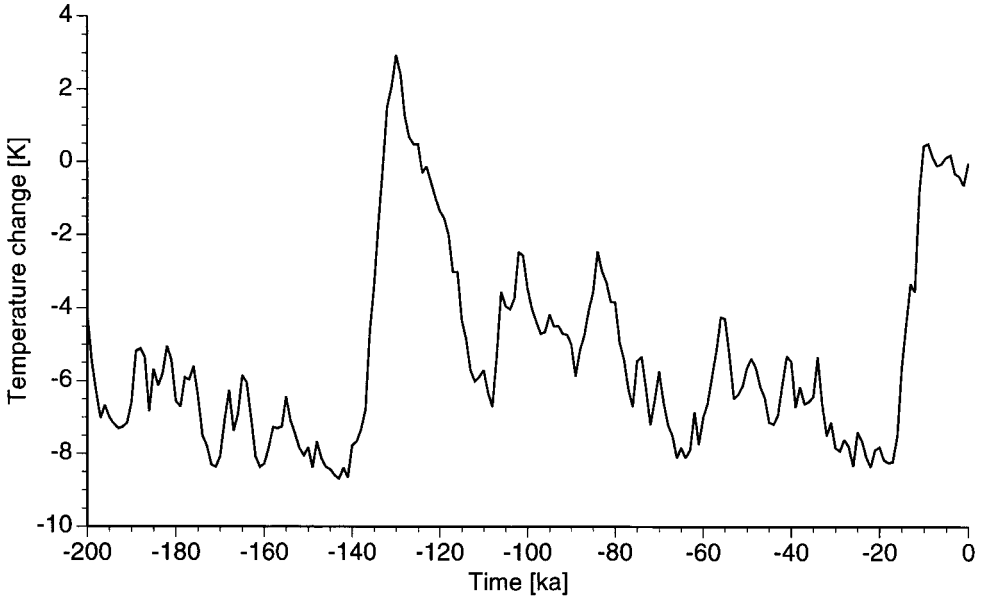


Figure 5: Background temperature signal from the Vostok ice core used for model forcing

ing the paleo-experiments surface temperature is perturbed by changes in background temperature (assumed uniform over the ice sheet) and by local changes in surface elevation. Changes in surface temperature also affect accumulation rates in different climates. Following Lorius *et al.* (1985) the accumulation rate  $M(t)$  in the past is calculated from its present value  $M(0)$  times the ratio of the derivatives of the saturation vapor pressure with respect to  $T_f(t)$  and with respect to  $T_f(0)$ , where  $T_f$  is the temperature above the inversion layer

$$M(t) = M(0) \exp \left[ 22.47 \left( \frac{T_0}{T_f(0)} - \frac{T_0}{T_f(t)} \right) \right] \left[ \frac{T_f(0)}{T_f(t)} \right]^2 \quad (37)$$

To relate the temperature above the inversion layer ( $T_f$ ) to the surface temperature ( $T_s$ ) the relation proposed by Jouzel and Merlivat (1984) was used:  $T_f(t) = 0.67 T_s(t) +$

88.9, where  $T_s(t)$  is the surface temperature [K] and  $T_0 = 273.15$  K (see also Huybrechts, 1990). Applying Eq.(37) for a temperature decrease of 10K, which is a typical value for a glacial–interglacial shift, we find for each point on the ice sheet profile (assuming that the temperature decreases with altitude) an accumulation rate which is roughly 50-60% of the present one.

On eustatic sea-level changes exists less agreement, probably because more detailed records of sea-level changes over the last glacial–interglacial cycle exist compared to temperature records. Shackleton (1987) made a careful comparison between several of these available data sets, showing a rather large discrepancy. We therefore opted to use all three of them for modeling purposes: (i) the Benthonic oxygen isotope record, (ii) the low resolution planktonic record from the west equatorial Pacific (which we replaced by a simple sawtooth function), and (iii) the New Guinea record, estimated from marine terraces (Shackleton, 1987). All three data sets are visualized in Figure 6.

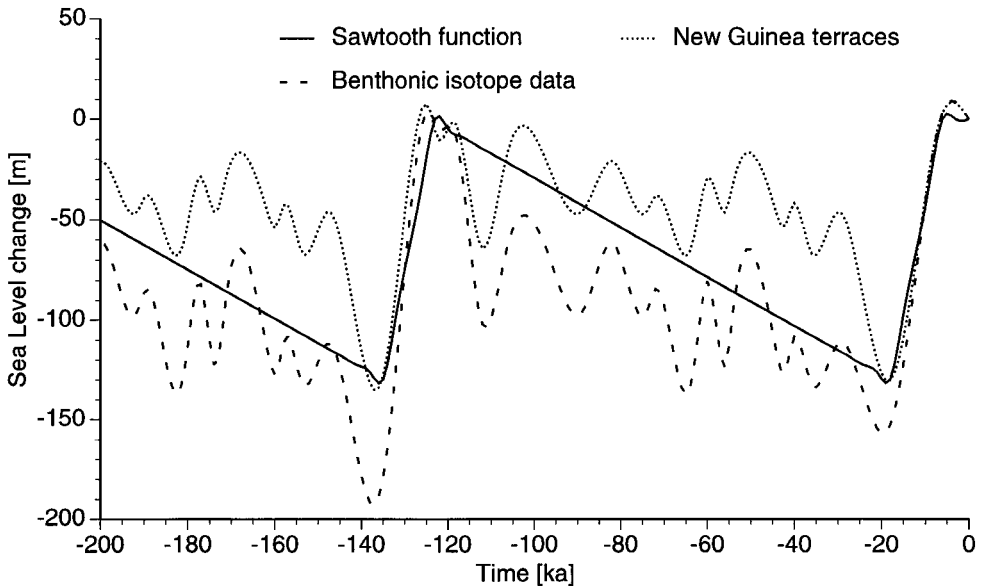


Figure 6: Eustatic sea level changes used for model forcing.

### 3.2 ICE STREAM DYNAMICS I: BASAL MOTION AND CYCLICITY

The aim of this part is to investigate the sensitivity of the ice sheet system to changes in basal boundary conditions, under a fixed present-day climate.

### 3.2.1 Experimental Setup

For the standard model run we considered a linear sloping bedrock, with an elevation of 500 m a.s.l. at the divide, away from it gradually lowering by 150 m per 100 km, and a horizontal grid size spacing of 10 km. Starting from the initial bedrock condition we developed an ice sheet bounded by the surface mass balance and temperature configuration as obtained from data of East Dronning Maud Land. Taking this simple bedrock topography, local extraneous effects interacting with the basal motion laws are excluded. After 40,000 years of calculation (with Deformation Model III) a full grown steady state ice sheet was obtained with a bedrock lying approximately 400 m below sea level (due to bedrock adjustment) and a temperature field coupled to the velocity field. Basal velocity was excluded from this standard run. The grounding line was situated at 470 km distance from the ice divide and determined by the flotation condition (Figure 7). Using this steady state situation as a reference, the model ran forward

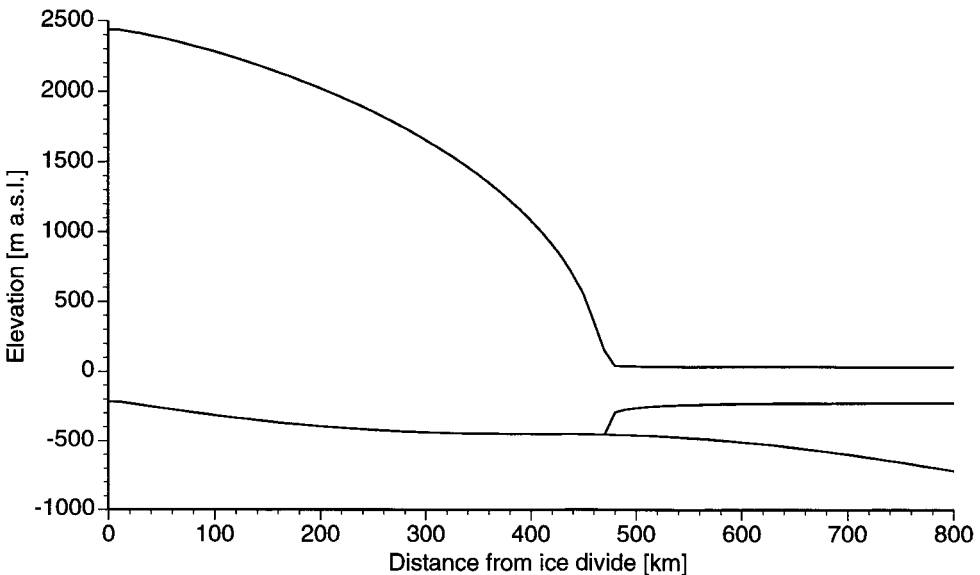


Figure 7: Basic ice sheet configuration in sliding experiments

again 20,000 years constrained by one of the five selected basal motion laws. According to Figure 8, the proportion of basal movement in the total balance velocity is highly dependent on the basal motion type. Basal sliding types 2, 4 and 5 show an increase in the proportion of basal motion in the total velocity towards the grounding line. These are the Budd and Van der Veen type (2 and 5 in Table I and Figure 8) based on Eq.(24), with the effective pressure independent from the water production at the ice sheet base, and the Alley type (4 in Table I and Figure 8) for a water film based on

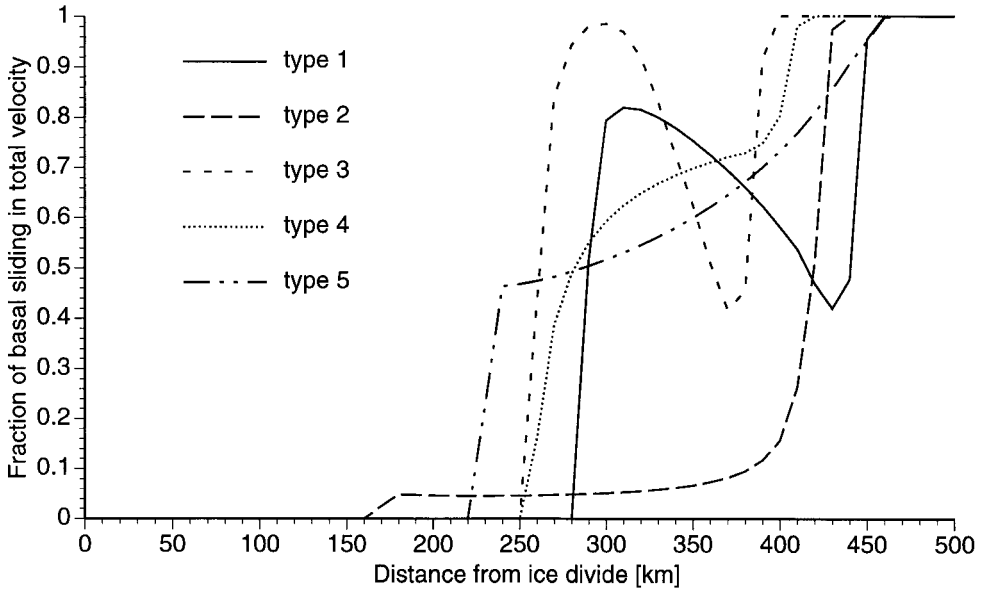


Figure 8: Ratio of the basal velocity to the total balance velocity in the ice sheet according to the 5 types of basal velocity laws after 20,000 years of integration

Eq.(26). These three types are a function of the basal shear stress, which increases towards the grounding line. However, the till deformation law (type 3) also depends on the basal shear stress, as can be seen in Table I, but looking closely at the governing equations for this type, one notices that the basal shear stress also enters the effective pressure  $N$  through Eq.(28), so that the basal motion in fact becomes inversely proportional to the basal shear stress due to the power constants  $p$  and  $q$  (with values of 1.33 and 1.8 respectively). The remaining types 1 and 3 (sliding over a water film and till deformation) are characterized by a sudden increase in basal velocity where the basal ice temperature reaches pressure melting point, and the proportion of the basal motion in the total velocity decreases in the downstream direction.

### 3.2.2 Oscillatory Behavior

A question that arises when the ice sheet is subjected to a change in basal boundary condition, is whether or not the ice mass will retrieve a new steady state. The answer is given by Figure 9, displaying the mean grounded ice thickness during the course of 20,000 years of integration for the five basal motion experiments (only the last 10,000 years are displayed). Whenever the basal movement cannot be balanced by the ice input upstream (and surface mass balance), the ice sheet will continuously shrink, given that the environmental conditions remain the same or favour the enhanced basal

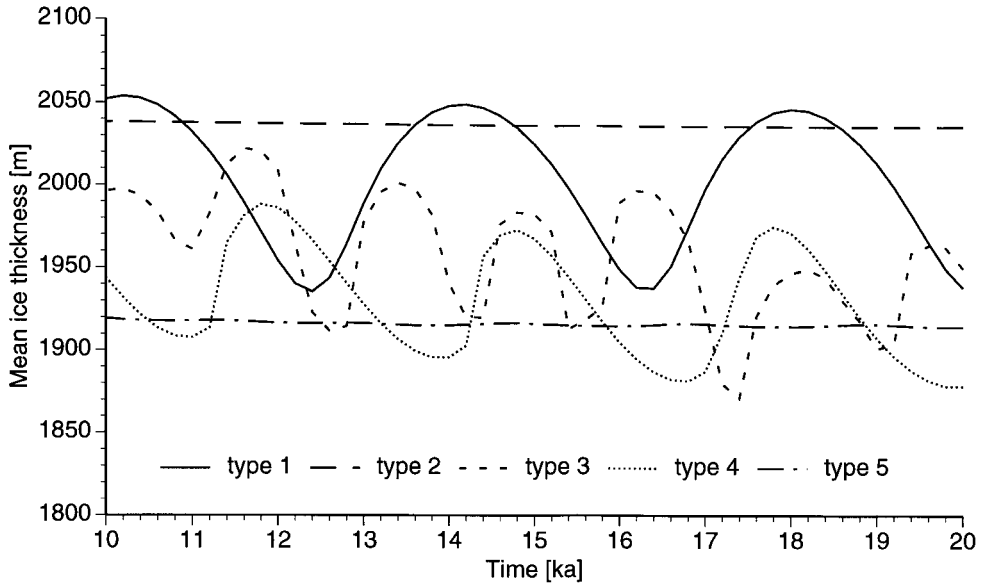


Figure 9: Evolution of the mean grounded ice thickness when applying the 5 different basal velocity laws

movement (such as a warmer climate). However, the ice sheet temperature plays an important role in controlling the basal ice sheet dynamics. Introducing basal movement causes the ice sheet to move more rapidly. The basal temperature decreases, leading to a decrease of the total surface subjected to melting. As a result basal velocities decrease, stabilizing the ice sheet motion. The whole process gives rise to a cyclic behavior: the slower ice sheet will tend to grow and warm, bottom melting increases, hence resulting in larger basal velocities. This can be seen in Figure 10, where both mean ice thickness and temperature change during the course of 10,000 years are displayed, according to the basal motion type 1. In particular, the sliding laws which are directly dependent on the changing basal characteristics such as the basal melting rate will show this apparent behavior. Furthermore, when basal velocity gradients increase, stretching becomes the dominant process, so that shearing in the basal layers becomes less effective ( $\partial u / \partial z \approx 0$ ), thus reducing the production of basal meltwater caused by shear strain heating. The amount of basal meltwater influences directly the basal water flux and the sliding velocity.

In order to obtain a better insight in the physical processes (both thermal and mechanical response) a closer look at the thermodynamic behavior during a cycle of the oscillation at different places in the ice sheet is necessary. Figures 11 and 12 display the different components of the heat budget at a distance of 100 km from the ice divide at the base of the ice sheet (Figure 11) and a height halfway up (Figure 12). The

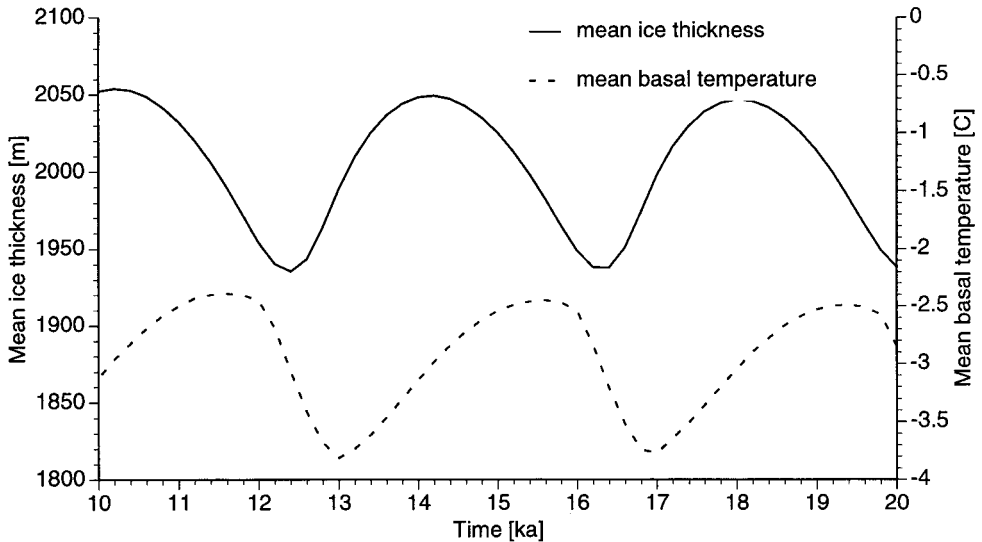


Figure 10: Evolution of the mean grounded ice thickness and basal temperature when applying basal velocity law 1

heat budget is divided into four components of the thermodynamic equation (Eq.13 on page 9), i.e. vertical diffusion, horizontal advection, vertical advection and friction, and are written as heat flux divergences in units of  $\text{Jm}^{-3}\text{a}^{-1}$ , representing the rate of energy change per unit volume. Once the basal ice reaches pressure melting point, the additional heat is used for enhanced melting (Eq.18 on page 11), which causes an increase in basal sliding through a basal motion law. Basal sliding itself produces more heat which is added to the basal temperature gradient (Eq.15 on page 10), resulting in a positive feedback, the so-called creep-instability. However, as seen in Figure 12, vertical advection rates increase in the ice sheet and slowly re-distribute the cold wave towards the bottom by means of vertical diffusion. At the base, increase in frictional heating causes the ice to warm, while an increase in vertical diffusion (probably the transport of the cold wave) cools it down afterwards (Figure 11).

Also the surface gradient decreases when the ice sheet becomes warmer and starts to flow faster. This would imply that the basal shear stress decreases, leading to a decrease in the basal temperature gradient, which is enhanced by both basal velocity and basal shear stress (Eq.15). For sliding laws which are directly proportional to the basal shear stress to a certain power, this effect decreases the basal velocities as well. However, it is not very clear if this influence is primordial in the oscillation process, since basal sliding laws which are not related to the basal shear stress or even inversely proportional to it, also show the apparent cyclic behavior.

These simple comparison experiments showed that regardless of climatic variability,

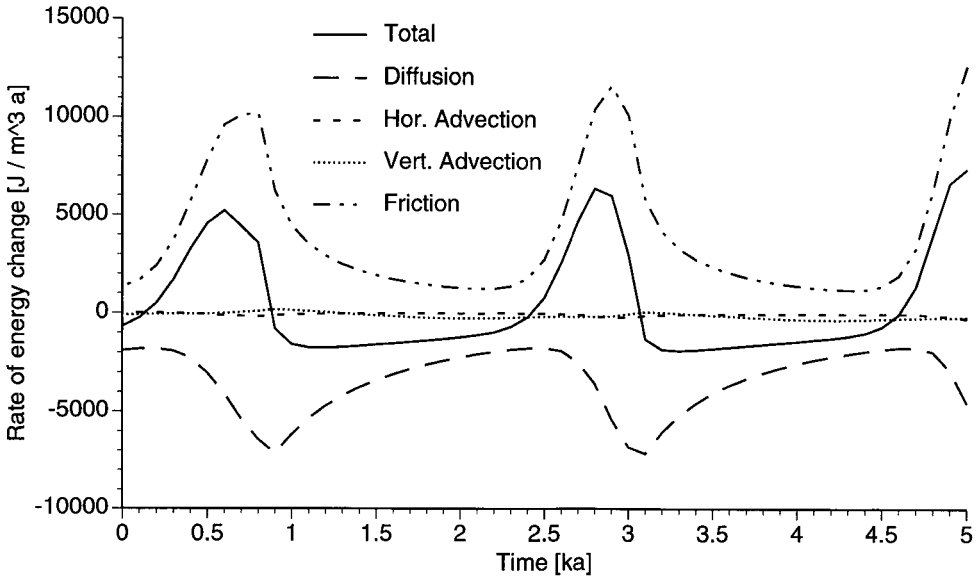


Figure 11: Time series of two cycles in the oscillation in terms of the energy budget at the base at 100 km from the ice divide

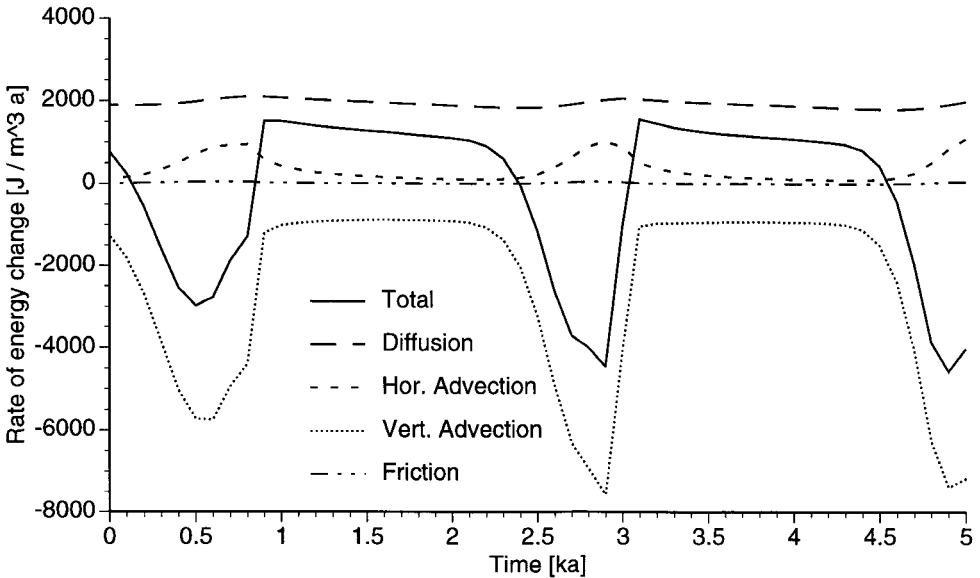


Figure 12: Time series of two cycles in the oscillation in terms of the energy budget at a height halfway up the ice sheet at 100 km from the ice divide



an internal oscillation mechanism is generated due to the interaction between the ice sheet thermo-mechanics and the basal processes, and that basal processes such as sliding over a water film, buoyancy at the grounding area and till deformation cause a different response in ice sheet behavior.

### 3.3 ICE STREAM DYNAMICS II: SHIRASE GLACIER

#### 3.3.1 Regional Description and Observations

Shirase Glacier (70°S, 39°E) is an important continental ice stream in East Dronning Maud and Enderby Land (Figure 3). It drains about 90% of the total ice discharge of Shirase Drainage Basin covering approximately 200,000 km<sup>2</sup> of ice coming from the polar plateau near Dome F (77°22'S, 39°37'E) (Fujii, 1981). Shirase Glacier is one of the fastest Antarctic glaciers, with velocities up to 2700 m a<sup>-1</sup> in the stream region (Fujii, 1981). Shirase Glacier covers a wide valley, which curves from a northward direction near the exit area to a north-west direction further inland. The subglacial bedrock lies below sea level at a distance of 100 km from the present coastline to reach 500 m a.s.l. near Mizuho Plateau (Mae and Yoshida, 1987). Elsewhere, the bedrock lies between 500 and 1000 m a.s.l. The glacier terminus is a free floating ice tongue in Lützow–Holmbukta. The shallow continental platform (< -300 m a.s.l.) in the eastern part of this bay is characterized by drowned glacial troughs. The 'Central Trough' extends up to 100 km northward from Shirase Glacier and reaches locally (close to Shirase Glacier) -1600 m a.s.l. (Moriwaki and Yoshida, 1983). The location of these troughs seems, as elsewhere in Antarctica, to be controlled by tectonics. The ice flow in Shirase Drainage Basin is also characterized by large convergence toward the Shirase Glacier stream area.

Extensive field work has been carried out in Shirase Drainage Basin during the last three decades. During the Japanese Glaciological Research Program (1969–1975), its major aim being the study of the ice flow of Mizuho Plateau, repetitive surveying of a triangulation chain, 250 km in length, revealed large submergence velocities (0.7 to 1.0 m a<sup>-1</sup>) in the region along the 72°S parallel, from 39°E to 43°E (Naruse, 1979). Taking into account densification in the upper firn layers, the accumulation was not enough to compensate for the ice mass deficit caused by the submergent flow, hence substantial thinning of the ice sheet at Mizuho Plateau was inferred. Later measurements in this area (Nishio *et al.*, 1989; Toh and Shibuya, 1992) confirmed this thinning rate ranging from 0.5 to 2.0 m a<sup>-1</sup> in the region where the surface elevation is lower than 2800 m. Furthermore, from an analysis of the total gas content of ice cores in Mizuho Plateau (Kameda *et al.*, 1990) it was also found that the ice sheet decreased by 350 m during the last 2000 years, and it was concluded that the thinning is a rather recent phenomenon. Mae and Naruse (1978) and Mae (1979) argue that the thinning of the

ice sheet in this particular area is predominantly caused by basal sliding with a velocity of about  $10 \text{ m a}^{-1}$ . These conclusions were drawn by applying the mass continuity equation (in a simplified version) to the local ice configuration properties, such as local ice thickness, surface and bedrock gradient, surface strain-rates, and mass balance. In addition the calculation of the basal shear stress profile along the central flow line was found to be similar to the shear stress profile of surging glaciers (Mae, 1979). This led the authors to conclude that the ice sheet is not in a steady state. However, no field survey data on the basal sliding velocity are available, nor is there new evidence supporting the thesis that the basal sliding mechanism is the main cause of enhanced ice sheet thinning.

It is however very likely that basal sliding will occur. Radio echo sounding in Shirase Drainage Basin (Nishio and Uratsuka, 1991) shows that large areas in the lower drainage basin are characterized by pressure melting at the base, and the authors estimated a water layer thickness of 0–30 cm at the interface between the base of the ice sheet and the bedrock in the downstream area of Shirase Glacier, even in areas where the bedrock lies well above sea level. Basal sliding is thus a candidate in playing a major role in the dynamic behavior of the ice sheet at Mizuho Plateau and certainly in the downstream area.

Despite the abundance of field data, numerical modeling experiments in the Shirase Drainage Basin area are very scarce. Apart from some steady state temperature and glacier profile reconstructions (Nishio *et al.*, 1989), three-dimensional dynamic modeling was performed by Nagao *et al.* (1984) and with an improved finite element model by Fujita *et al.* (1991). Despite this improvement, major shortcomings were the ignorance of longitudinal stress and isostatic changes, a fixed seaward boundary, and the use of a steady state temperature profile. Excluding these features may seriously hamper a profound analysis of the ice sheet dynamics. The present modeling experiments aim at a better understanding of the present ice sheet dynamics of Shirase Glacier, the sensitivity of the ice sheet system with respect to different boundary conditions and its dynamic behavior in a time-dependency. First however, the present stress field of Shirase Glacier is calculated based on field observations at the glacier surface in order to infer the characteristics of the stream area.

### 3.3.2 Present Stress Field of Shirase Glacier

When the ice sheet geometry (ice thickness, surface elevation) and the surface horizontal velocity field are known, it becomes possible to calculate the present stress field and basal velocity of the ice sheet by integrating the model equations in a reversed way. This 'diagnostic model run' can be obtained by integrating Eq.(43) and Eq.(44) on page 64 (Deformation Model III) from the surface of the glacier to a relative height in

the glacier. Boundary conditions are the surface horizontal and vertical velocity. Since vertical velocities are not known, a steady state situation for the upper boundary of the vertical velocity is assumed, which equals the surface mass balance rate. Horizontal surface velocities are known at several sites on Mizuho Plateau and at the glacier margin. Temperature in the ice sheet was calculated on the basis of a steady state temperature distribution and coupled to the velocity field by means of the Arrhenius relationship (Eq. 12 on page 9).

Adopting this ice sheet configuration, it was possible to obtain the two-dimensional stress and strain field in the ice sheet, from the ice divide to the edge of the floating ice shelf, simply starting from the present horizontal velocity. The resulting effective stress distribution (incorporating both shearing and stretching) in the glacier area (from a distance of 600 km from the ice divide down to the grounding line) is displayed in Figure 13. In the upstream area the ice flow is primarily governed by shear stresses

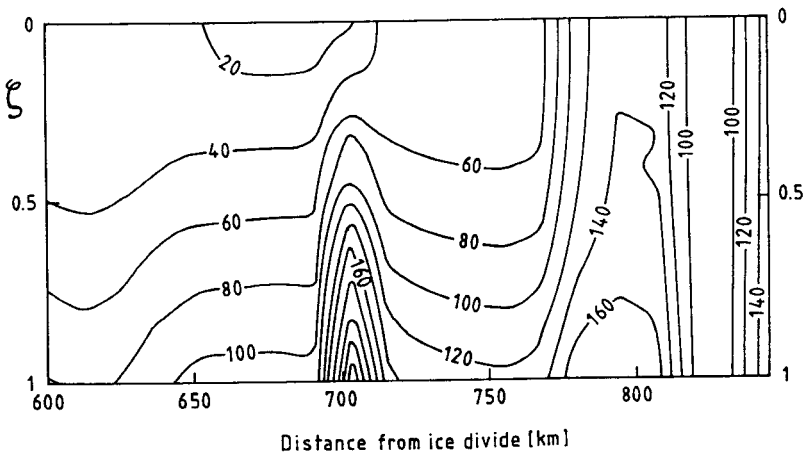


Figure 13: Two-dimensional effective stress field [Pa] in the stream area of Shirase Glacier

(down to 710 km from the divide), because of the relatively high surface slopes imposing a large driving stress. The stream area itself (from 800 km further downstream) is almost solely driven by longitudinal stretching, and shear stresses are almost negligible. Between these two areas both shear stress and longitudinal stress are of the same order of magnitude and form some kind of transition zone. Figure 13 depicts, despite the poor knowledge on the detailed surface and bedrock topography and surface velocities in the stream area (700-850 km from the divide), the overall characteristics of an ice stream, i.e. a large horizontal velocity gradient and a very small vertical gradient of the horizontal velocity ( $\partial u / \partial z \approx 0$ ). These features resemble more ice shelf behavior than grounded ice sheet dynamics and is called 'shelly stream'.

**Table II:** Comparison of measured horizontal surface velocity of different stations on Mizuho Plateau with present steady state modeled values. Also listed are the modeled basal sliding velocity and the basal shear stress according to the standard model run.

Station	$u(H+h)$ [m a <sup>-1</sup> ] measured	$u(H+h)$ [m a <sup>-1</sup> ] model	$u(h)$ [m a <sup>-1</sup> ] model	$\tau_b$ [kPa] model
G6	8	6	0.6	58.8
G5	13	8	0.8	66.1
G4	20	14	1.3	83.8
G3	29	17	1.9	82.4
G2	36	39	3.8	110.5
Stream	2000-2500	253	251.8	40.0

Vertical resistive stresses play a role in those areas where the flow regime changes, i.e. from shearing to stretching and vice versa. They are of the order of 1 to 5 kPa, almost two orders of magnitude smaller than the effective stress.

### 3.3.3 Steady State Modeling Experiments

The main purpose of the modeling experiments is to calculate the present local imbalance of the ice sheet by imposing different basal boundary conditions. Seen the relative importance of longitudinal stresses in the stream area, Deformation Model III was employed. Choosing a basal boundary is however less straightforward. Till deformation and/or water drainage along both a soft and hard bed will very likely occur, as is the case with other ice streams of Antarctica, though no observations or measurements of this kind are available. However, subglacial drainage structures on hard bed are observed along the ice free Sôya Coast in Lützw-Holmbukta and seem to be of a recent date (T. Sawagaki, pers. comm.). We will therefore restrict ourselves to a basic experiment, i.e. will an oscillating behavior set in and can the present observed imbalance be explained by this kind of mechanism?

As a basic experiment the ice sheet system was run forward in time, starting from the present ice surface and bedrock elevation, until a steady state was reached after approximately 200 ka. Basal motion type 4 was employed with a tuning parameter  $A_s = 2.0 \cdot 10^{-11} \text{Pa}^{-2} \text{m}^{-1} \text{a}^{-1}$  (see Table I on page 14). The tuning value for the ice sheet and ice shelf (parameter  $m$  in Eq.(12) on page 9) was set to 1.0 and 0.2 respectively. The resulting ice sheet profile is displayed in Figure 14.

Modeled ice thicknesses are in overall accordance with the observed values, as are the horizontal surface velocities compared to the measured velocities in the field (Table II). However, in the stream area of Shirase Glacier horizontal surface velocities are one order of magnitude lower than the observed values. Obviously, the large con-

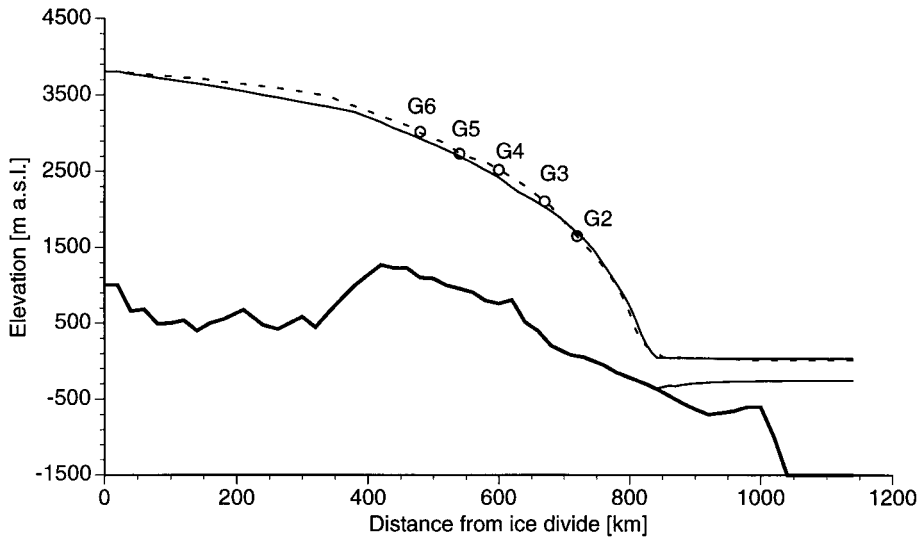


Figure 14: Steady state simulation for Shirase flow line (full line) compared to the present observed situation (dashed line). The model domain extends from the ice divide (0 km) to beyond the edge of the continental shelf (1100 km). G2 to G6 are markers where the surface velocity and thinning rate are observed.

vergence of the ice flow is not sufficient to cause a large increase in the downstream surface velocity (from  $40 \text{ m a}^{-1}$  at Mizuho Plateau to  $2500 \text{ m a}^{-1}$  in the ice stream). Some other flow mechanism should account for this, probably an enhanced basal sliding which causes the ice stream to flow like an ice shelf, the so-called 'shelvy stream'.

Nevertheless, even in this steady state experiment longitudinal deviatoric stresses play a dominant role in the vicinity of the grounding line, and are almost one order of magnitude higher than the shear stresses. Due to the basal sliding and longitudinal stretching in the transition zone between the ice sheet and the ice shelf the surface slope decreases. An immediate consequence of the decreasing downstream surface slope and ice thickness is that the basal shear stress will not reach its maximum at the ice sheet edge, but somewhat more upstream, as shown in Table II. Despite the conclusion of Mae (1979) that a similar profile of the basal shear stress along the central flow line should indicate that the ice sheet is not in steady state or that this basal shear stress configuration resembles a surging glacier, the numbers in Table II are those of a steady state ice sheet solution.

### 3.3.4 Dynamic Modeling Experiments

In order to study the dynamic sensitivity of Shirase Drainage Basin and its present local imbalance and thinning rate the evolution of the ice sheet was simulated during a

complete glacial–interglacial cycle. As an initial configuration, the model was run in a steady state with background temperature of  $-5.2$  K and a sea-level 50 m lower than the present eustatic level. The model was then forced according to the Vostok temperature signal (Figure 5) and eustatic sea-level changes according to the data from the New Guinea terraces (Figure 6). Three experiments were carried out, each with different values for the tuning parameter  $A_s$  of basal motion type 4 in Table I on page 14, i.e. 2.0, 4.0 and  $6.0 \cdot 10^{-11} \text{Pa}^{-2} \text{m}^{-1} \text{a}^{-1}$ .

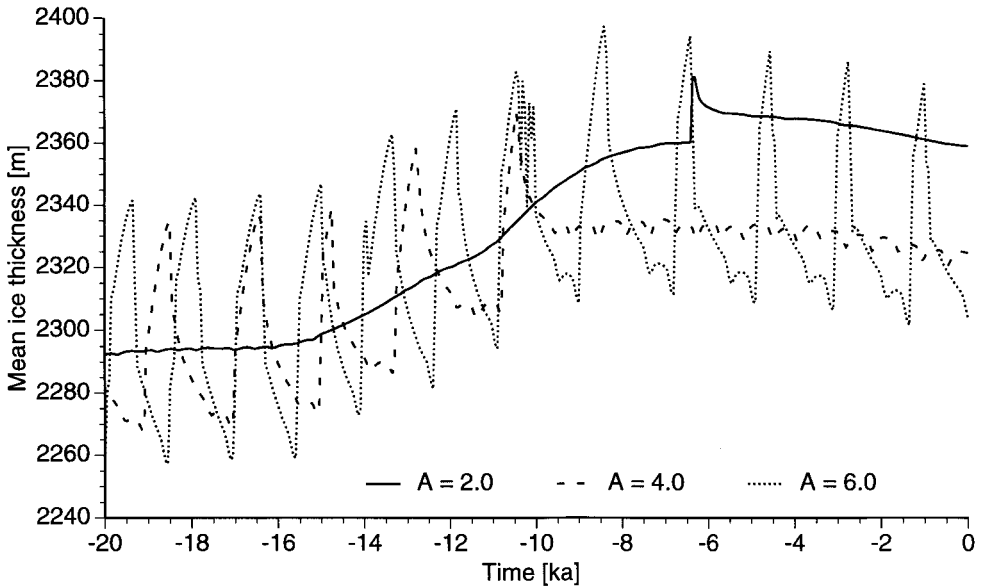


Figure 15: Evolution of the mean ice thickness over the last 20 ka in Shirase Drainage Basin for three different values for the tuning parameter  $A_s$  of basal motion type 4, i.e. 2.0, 4.0 and  $6.0 \cdot 10^{-11} \text{Pa}^{-2} \text{m}^{-1} \text{a}^{-1}$ .

Figure 15 shows as a result the mean ice thickness evolution from 20 ka BP to present. The tuning value clearly triggers the onset of a cyclic behavior, although small variations can be observed with the lowest tuning value. Doubling the tuning value to  $4.0 \cdot 10^{-11}$  creates two types of oscillations: large oscillations during the last glacial stage, becoming abruptly small in the Holocene. This difference is probably due to changes in the surface mass balance budget, as explained by Payne (1995). Furthermore, the oscillations are superimposed on the basic climatic response marking the glacial–interglacial contrast. However, a larger tuning value of  $6.0 \cdot 10^{-11}$  results in a general oscillation with small differences between the glacial and the interglacial period. Ice surface variations are not exceptionally large (mean ice thickness fluctuates with an amplitude of approximately 80m), and the amplitude of the oscillations (dotted line) is of the same order of magnitude as the ice sheet surface variation over a

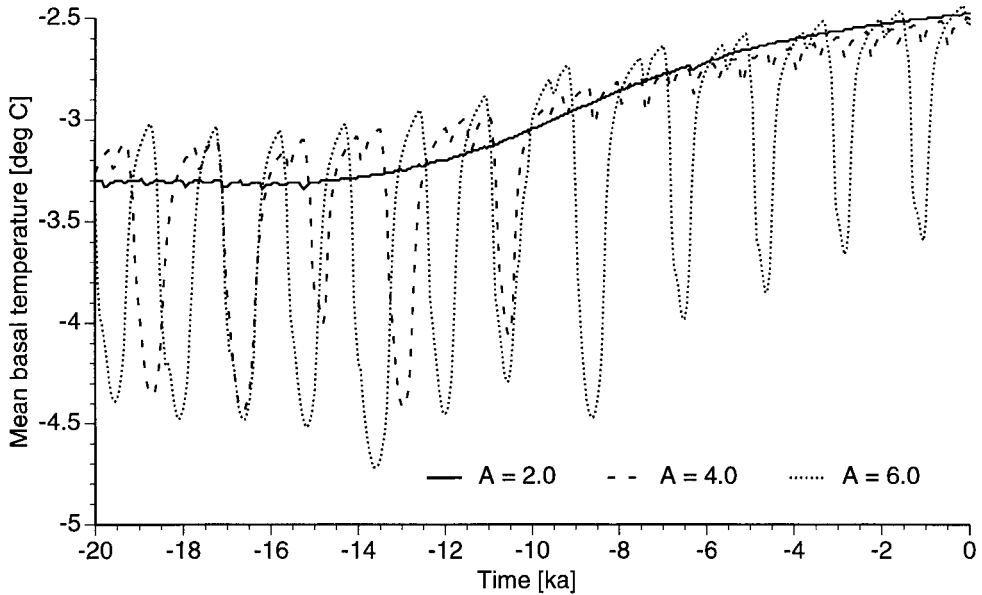


Figure 16: Evolution of the mean basal temperature over the last 20 ka in Shirase Drainage Basin for three different values for the tuning parameter  $A_s$  of basal motion type 4, i.e. 2.0, 4.0 and 6.0  $10^{-11} \text{Pa}^{-2} \text{m}^{-1} \text{a}^{-1}$ .

glacial–interglacial cycle (solid line). Ice sheet variations remain relatively small: no extreme ice loss is observed, nor any instability of the ice sheet which should lead to a collapse or a (partial) disintegration of the ice sheet. It is however the small periodicity of the oscillations that accounts for high imbalance values. These imbalance values are within the range of the present observed imbalance and increases towards the coast. Furthermore, the velocities at the grounding line occasionally exceed  $1000 \text{ m a}^{-1}$  during the cyclic behavior.

The variations in mean basal temperature corresponding to these experiments are displayed in Figure 16. The oscillations in basal temperature also follow the main climatic trend, but are characterized by a much larger amplitude than the basic amplitude in the glacial–interglacial contrast, i.e. 1.5 K versus 0.7 K.

### 3.4 DYNAMICS OF THE ICE SHEET IN EAST DRONNING MAUD LAND

The main purpose of this part is to investigate the ice sheet behavior during the course of the last 200,000 years (last and penultimate glacial period) and to extract the controlling factors for its behavior in that period. To serve this purpose both steady state and dynamic sensitivity experiments were carried out and a special care was taken for the ice sheet response to changes in both environmental conditions and model param-

eters at different places in the ice sheet, i.e. in the vicinity of the mountain range and beyond.

### 3.4.1 Situation and Glacial History of the Sør Rondane

The Sør Rondane Mountains are a 200 km long mountain range, approximately 100 km from the present coast and form part of a series of mountains surrounding the East Antarctic continent (Figure 3). Morphologically, this area is quite different from the Shirase Drainage Basin, except for the inland part between the ice divide and the mountain range. The mountains block the ice flow and at some places large outlet glaciers cut through the range. These are characterized by overdeepened valleys that resemble an ice covered fjord landscape and have very high surface slopes. Between the mountains and the edge of the continental shelf the bedrock lies beneath sea level. Some subglacial trenches (not as deep as Shirase Glacier) are present.

Besides the glaciological field work in this area, such as measurements of ice thickness and glacier velocity (Pattyn and Declerq, 1995b), glacio-geological and geomorphological research is carried out mainly by the Japanese Antarctic Research Expedition. Based on dating from cosmic ray bombardments of exposed till at some places in the Sør Rondane, which is also linked to the degree of weathering of till, Moriwaki *et al.* (1991) and Moriwaki *et al.* (1992) found that

- during the last glacial–interglacial cycle, rather minor ice sheet fluctuations occurred (from a few meters to a few tens of meters);
- during former glaciations, glacier surface stands were somewhat higher (up to 100 m higher than the present ice surface at around 1.5 Ma BP).

The extremely minor changes in ice sheet variations recorded in the Sør Rondane for the last glacial–interglacial (present) contrast could imply that the response of the ice sheet to environmental change is much lower than previously thought, or that environmental changes (especially eustasy) are overestimated. However, the geomorphological results could also imply that the present size of the ice sheet is close to its maximum size, and hence large parts of the ice sheet are out of balance with the present climate.

### 3.4.2 Steady State Sensitivity Experiments

Seen the relative small observed ice sheet variations during the last million years and the relatively slow movement of the ice sheet in the mountain range and the coastal area, basal sliding will hardly play a significant role in controlling the ice dynamic behavior. Moreover, as seen from maps and satellite images, there is no definite transition zone between the grounded ice sheet and the ice shelf, nor are there any traces of fast





flowing ice and heavy crevassing. We therefore included a basal motion type 5 (Table I) with a tuning value of  $2.0 \cdot 10^{-8} \text{N}^{-2} \text{m}^5 \text{a}^{-1}$  in combination with the ice deformation characteristics of Deformation Model II.

In a first experiment the model ran forward in time with the Asuka flow line data (outlet glacier Gjelbreen) until a steady state was reached after approximately 200,000 years. In order to control the height-to-width ratio, the free parameter  $m$  in Eq.(12) on page 9 was set to 1.0 for the grounded ice sheet and to 0.1 for the ice shelf. The steady state situation is presented in Figure 17. The ice sheet invades the central mountain

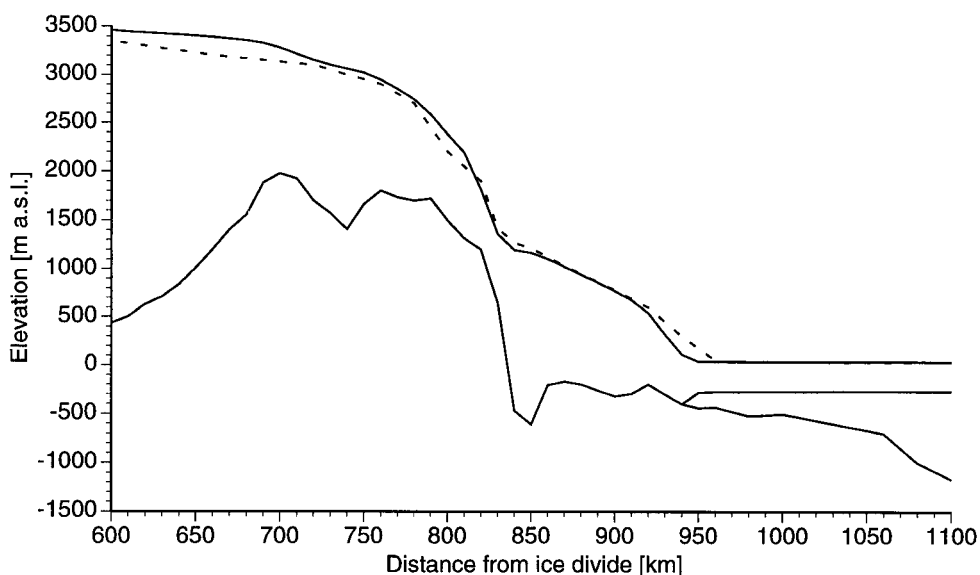


Figure 17: Steady state simulation of the Asuka flow line (full line) compared to the present observed situation (dotted line). The model domain extends from the ice divide (0 km) to beyond the edge of the continental shelf (1200 km). Only the area between 600 and 1100 km is shown. The glacier area inside the mountains is situated between 780 and 870 km.

range at 780 km and the glacier cascades down creating an ice fall. At the bottom of the ice fall (830 km) the surface slope diminishes and the glacier flows slowly in a deep trough, exiting the mountain range at 870 km. In this area bedrock remains below sea level. The difference between the modeled and the observed profile is within 150 m, which is acceptable seen the uncertainties in bedrock elevation outside the mountain area. Inside the mountains, the difference remains smaller than 50 m.

A first series of steady state sensitivity experiments was performed to investigate how the ice sheet reacts to environmental changes and the response times that are involved to obtain an equilibrium state to the new climate. The environmental changes were chosen to lie within the range of a full glacial–interglacial contrast as experienced over the last 200,000 years, whereby the present climatic conditions are taken as the

'interglacial' reference. The model was run forward in time for 100,000 year with individual changes in mass balance, temperature and sea level, and a combination of these changes. Forcing values are a lowering of mass balance by roughly 50 % (according to Eq.(37) on page 21), a temperature drop of 10 K and a sea level lowering of 130m. These values are typical for a recent glacial stage. Results of the forcing experiments are displayed in Figures 18 and 19 in which a constant geothermal heat flux corresponding to 1.30 HFU was assumed, and in Figures 20 and 21 where bedrock heating was included. The following conclusions can be drawn:

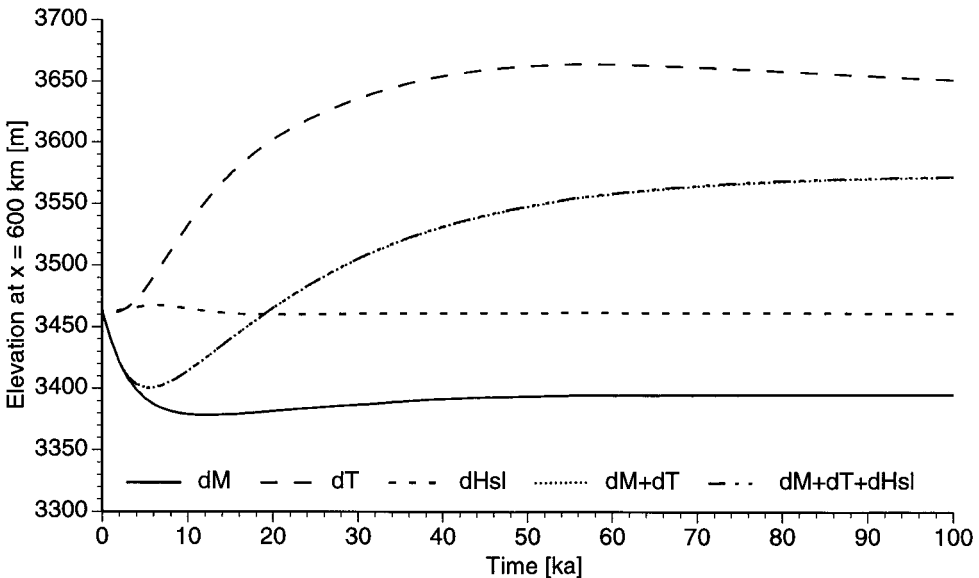


Figure 18: Reaction of the ice sheet (polewards of the mountains) at  $x = 600$  km to an instant lowering of mass balance by 50 % (dM), a temperature drop of 10 K (dT) and a lowering of sea level by 130 m (dHsl). Constant geothermal heat flux corresponding to 1.30 HFU

- Two important controlling factors in ice sheet variations over the total length of the flow line are temperature and mass balance. A decrease in mass balance causes an ice sheet lowering, while a drop in background temperature causes the ice sheet to expand.
- Sea level variations have only an effect in the coastal area and the lower part of the glacier. Higher up and beyond the mountains, the effect is minimized and even non-effective. This means that local effects in the coastal area do not influence the inland ice sheet and are hampered by the presence of the mountain range.

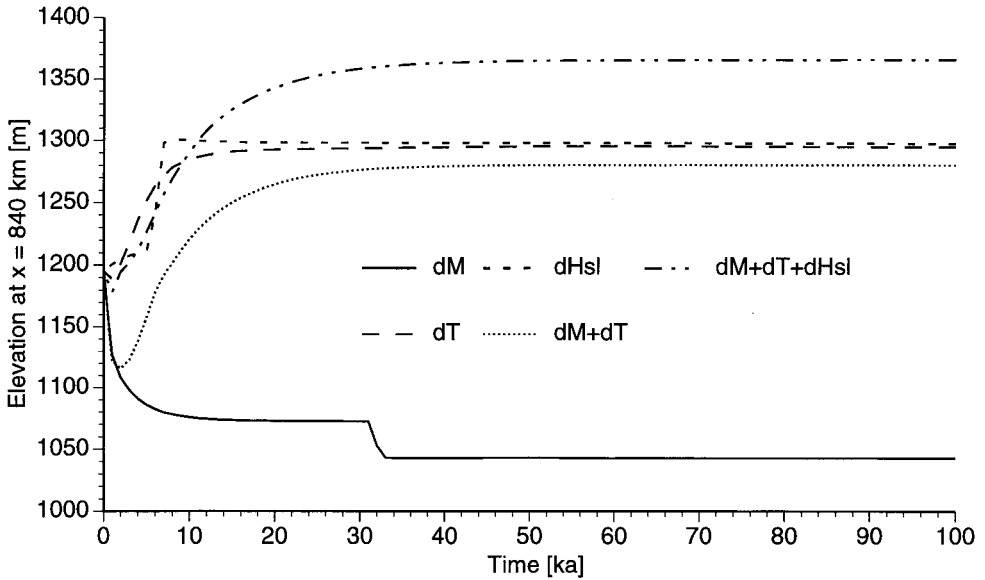


Figure 19: Reaction of the ice sheet (inside the mountain range) at  $x = 840$  km to an instant lowering of mass balance by 50 % ( $dM$ ), a temperature drop of 10 K ( $dT$ ) and a lowering of sea level by 130 m ( $dHsl$ ). Constant geothermal heat flux corresponding to 1.30 HFU

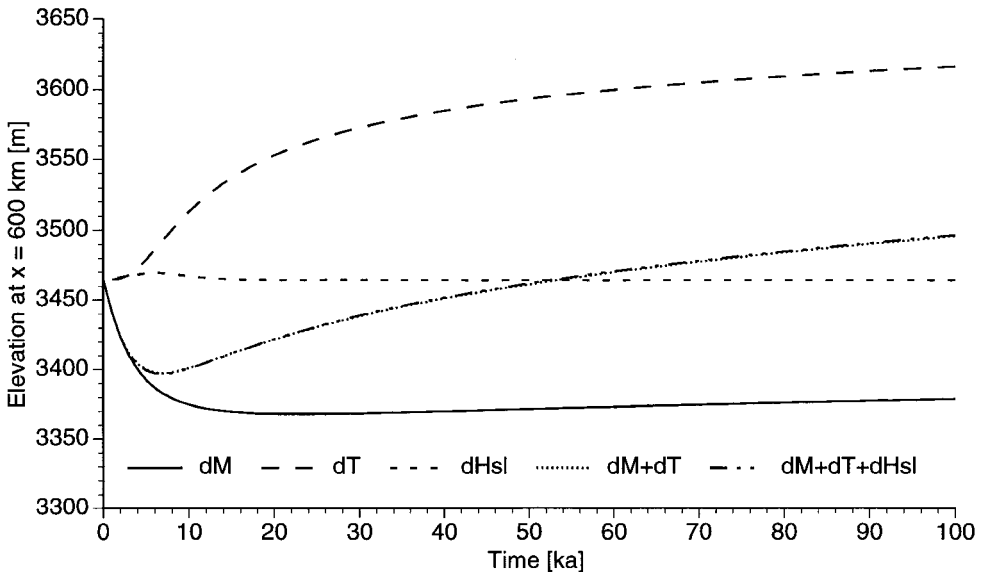


Figure 20: Reaction of the ice sheet (polewards of the mountains) at  $x = 600$  km to an instant lowering of mass balance by 50 % ( $dM$ ), a temperature drop of 10 K ( $dT$ ) and a lowering of sea level by 130 m ( $dHsl$ ). Bedrock heating is included.

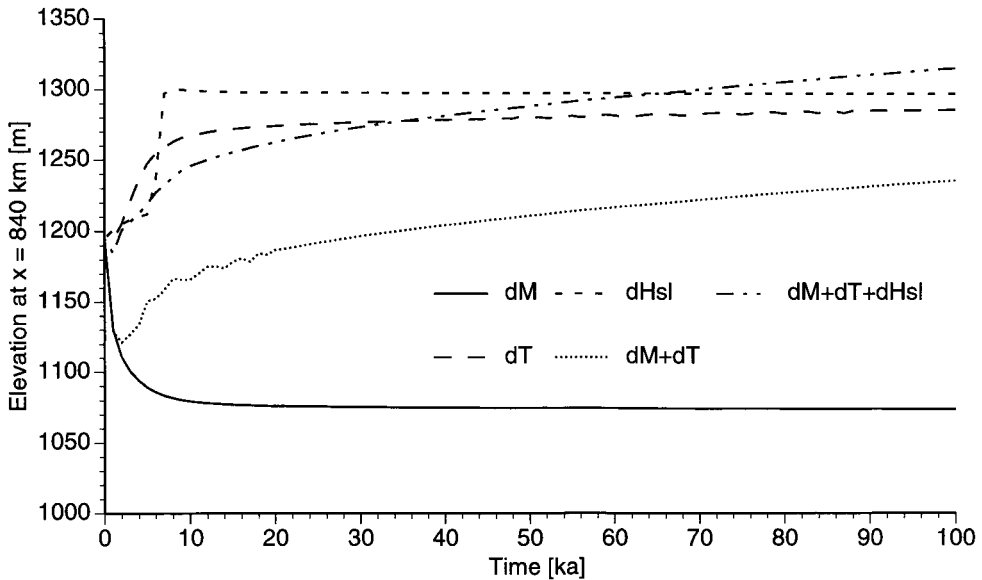


Figure 21: Reaction of the ice sheet (inside the mountain range) at  $x = 840$  km to an instant lowering of mass balance by 50 % ( $dM$ ), a temperature drop of 10 K ( $dT$ ) and a lowering of sea level by 130 m ( $dHsl$ ). Bedrock heating is included.

- A combination of temperature and mass balance change will have a counteracting effect. Behind the mountain range surface changes therefore remain small. In the coastal area the counteracting effect is minimized, since the thickening of the ice due to lower temperatures also imply an ice sheet advance.
- Response times to changes in both mass balance and sea level are rather small (10–30 ka).
- The largest response times are encountered when changes of surface temperature are involved (50–100 ka). When bedrock heating is included, a steady state is not even reached after 100 ka.
- Because of the different time lag in response to temperature and mass balance, the ice surface will first lower due to lower mass balance rates and then gradually increase as the surface temperature change affects the whole ice body (dotted line in experiments).

### 3.4.3 Dynamic Experiments

Subsequently, the ice sheet system is forced according to the Vostok temperature signal and eustatic sea level changes as given in Figures 5 and 6. First, the model is run

into a steady state with a background temperature of  $-5.2$  K, which is the mean temperature over the period of the last 200,000 years and a sea level of  $-50$  m. Afterwards the model was forced with the Vostok signal. Six experiments were carried out: forcing with the three sea-level curves for a constant geothermal heat flux corresponding to  $1.30$  HFU (Figures 22 and 23) and with bedrock heating included (Figures 24 and 25).

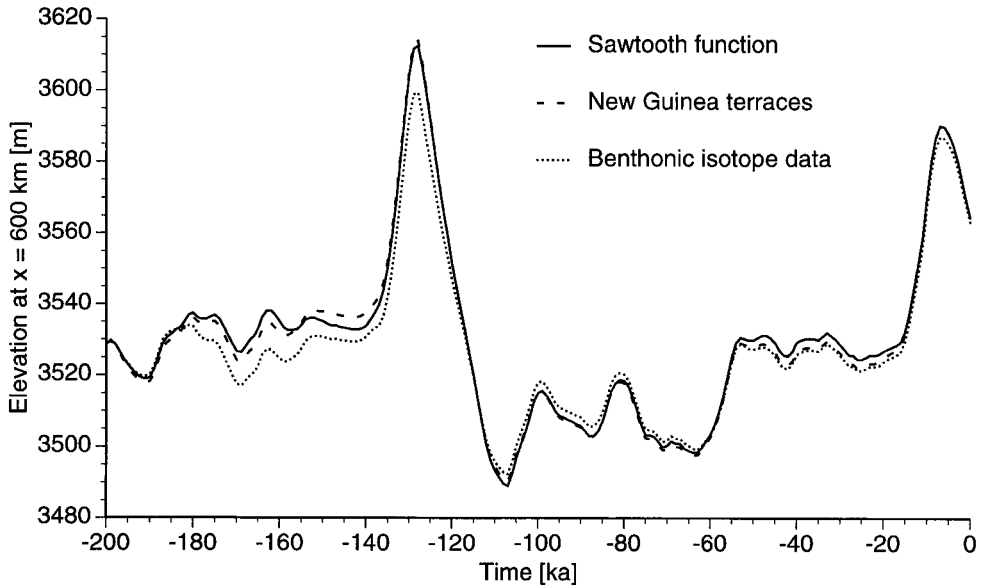


Figure 22: Reaction of the ice sheet (polewards of the mountains) at  $x = 600$  km to a forcing with the Vostok temperature signal and three eustatic sea-level changes. Constant geothermal heat flux corresponding to  $1.30$  HFU

The following conclusions can be drawn:

- Surface elevation changes on a glacial–interglacial contrast are of the order of  $120$  m behind the mountain range (at  $x = 600$  km) to maximum  $350$  m in the area between the mountains and the coast, the latter depending on the sea-level curve used.
- Surface elevation changes follow with a certain time lag the forcing temperature signal. Sea-level changes enhance the reaction of the ice sheet to the temperature signal. Especially the sea-level curve based on the Benthonic isotope data produces a bigger penultimate glacial ice sheet. As explained in the previous section, behind the mountain range sea-level changes have a negligible effect on the ice sheet surface elevation change.

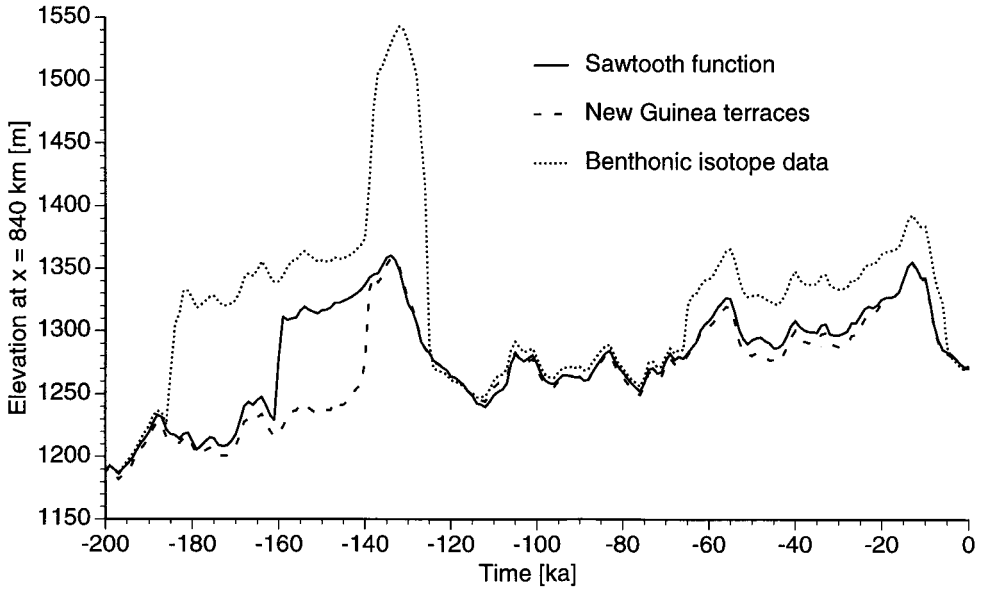


Figure 23: Reaction of the ice sheet (inside the mountain range) at  $x = 840$  km to a forcing with the Vostok temperature signal and three eustatic sea-level changes. Constant geothermal heat flux corresponding to 1.30 HFU

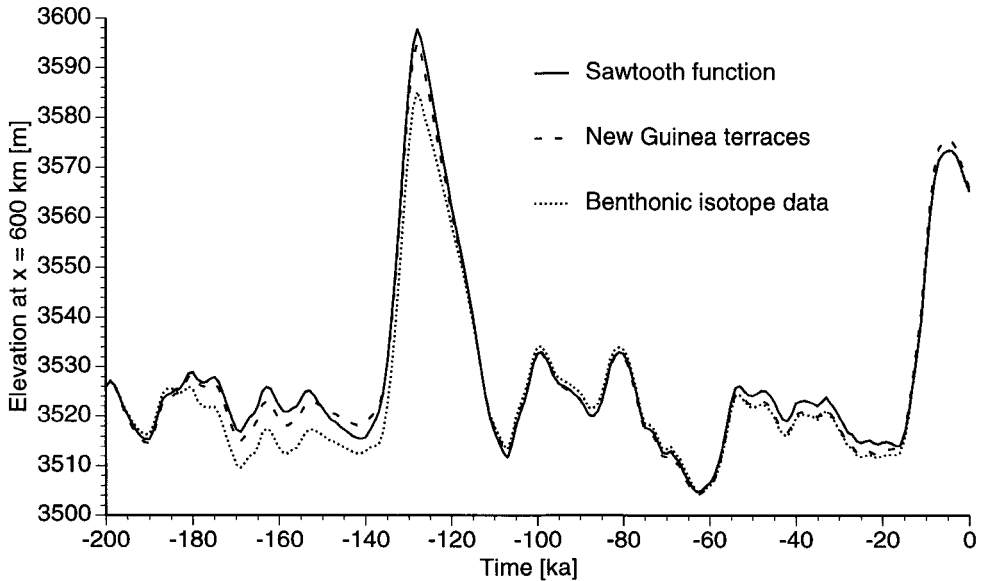


Figure 24: Reaction of the ice sheet (polewards of the mountains) at  $x = 600$  km to a forcing with the Vostok temperature signal and three eustatic sea-level changes. Bedrock heating is included.

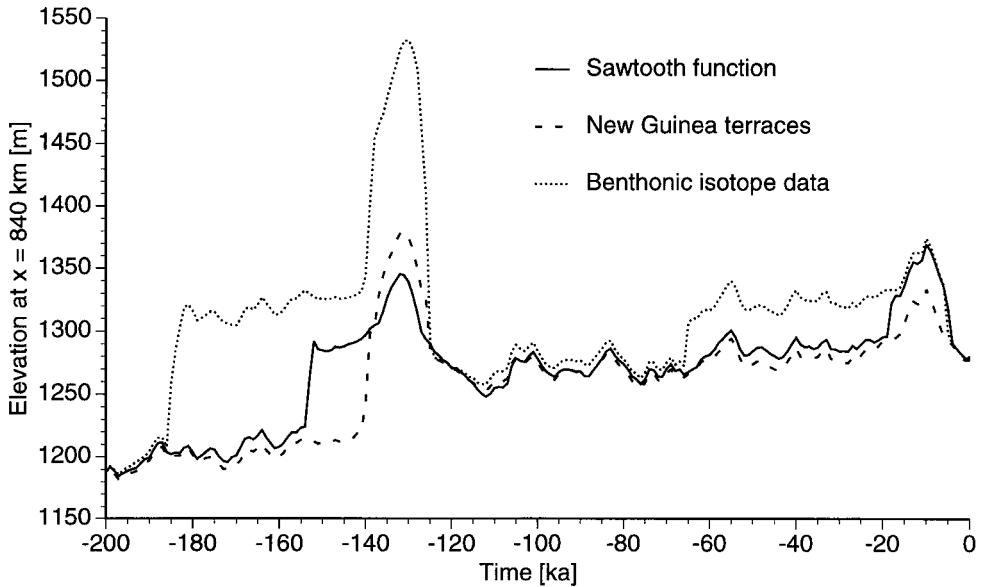


Figure 25: Reaction of the ice sheet (inside the mountain range) at  $x = 840$  km to a forcing with the Vostok temperature signal and three eustatic sea-level changes. Bedrock heating is included.

- Ice sheet variations (glacial–interglacial contrast) are generally larger during the penultimate glacial stage than during the last glacial stage.
- The largest ice sheet expansion does not correspond with the lowest temperature signal, but follows somewhat later. The time lag increases with increasing distance from the coast and generally falls at the beginning of the warmer period or even within. This means that the present ice sheet is close to its maximum expansion.
- Behind the mountains and at the entrance of the glaciers in the range, ice sheet variations are largely controlled by temperature and mass balance. At the end of a glacial stage (i.e. when background temperature is lowest) the cold ice sheet is not extremely big because of reduced mass balance. Only when temperature rises, the expansion is visible due to the combination of a cold ice sheet with increased mass balance. The process is further delayed by the slow re-distribution of temperatures in the ice sheet towards the divide and the inclusion of geothermal heating. Maximum surface elevation is observed in the Holocene (5-10 ka BP) and in the penultimate interglacial (120 ka BP).
- Between the mountains and the coast, sea-level changes determine the ice sheet lateral expansion and hence also control ice sheet surface elevation changes

besides the temperature/mass-balance effect. The maximum surface elevation changes depend to a large extent on the sea-level curve used. The maximum elevation is situated at the beginning of the Holocene (7-13 ka BP) and at around 130 ka BP.

In short, small surface elevation changes in the mountain area, which is in accord with the present day geomorphological findings, is obtained when bedrock heating is included in the thermo-mechanical response and sea-level changes are of minor importance (i.e. the eustatic curve based on data from the New Guinea terraces). For this experiment we can go into further detail.

2

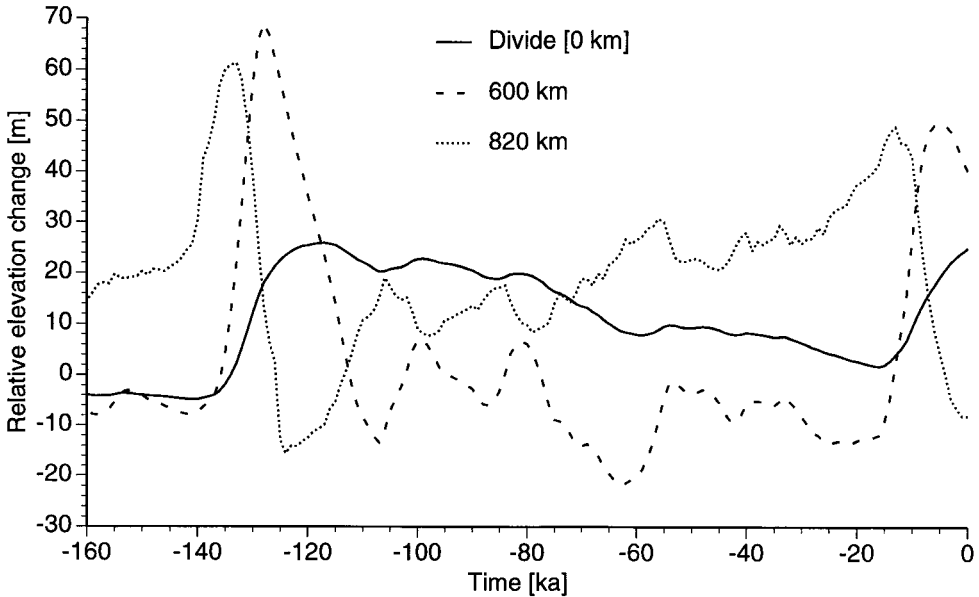


Figure 26: Reaction of the ice sheet at the ice divide, at  $x = 600$  km and at  $x = 820$  km to a forcing with the Vostok temperature signal and eustatic sea-level change according to the New Guinea data. Bedrock heating is included.

Figure 26 shows the relative surface elevation changes at three places in the ice sheet (i.e. the ice divide, behind the mountains and inside the range) in the course of the last 160 ka. Besides the time lag and the difference in amplitude in the response to the climate signal, some more interesting features can be observed:

- Between the penultimate and the last glacial stage the surface elevation gradually lowers at the divide, remains approximately constant behind the mountain range (a local minimum is observed around 62 ka BP) and gradually increases in the mountain range.



- The further away from the coast, the less pronounced is the reaction of the ice sheet to small temperature differences in the climate signal.
- At present, the ice surface in the vicinity of the ice divide is still rising.

Finally, a summary of the main characteristics of ice sheet response over time at different places in the ice sheet is given in Table III. Maximum ice surface elevations are only a few meters to a few tens of meters higher than present, and increase towards the coast, while the total amplitude of surface elevation change is around 60-70 m for the whole area of interest. A schematic representation of ice surface variations in the Sør Rondane for the last 22 ka, based on the above described experiment, is given in Figure 27. At 22 ka BP (i.e. lowest surface temperature of last glacial period) the ice sheet surface is generally rising, except at the divide. At 10 ka BP the deglaciation process is general in the coastal area and at the northern part of the mountain range, but at the southern part the ice sheet still grows and diminishes not before 5 ka BP. At present the coastal area thickens again, inside the mountains the ice surface still lowers, while at the ice divide the ice keeps thickening.

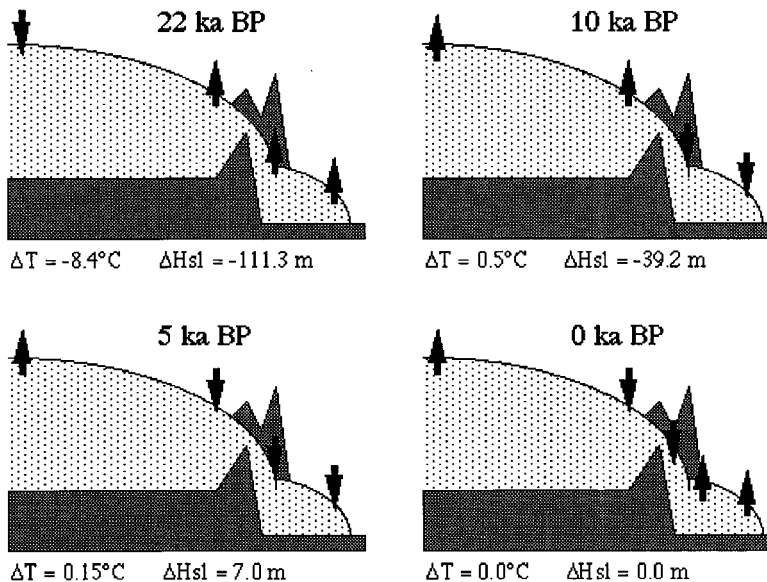


**Figure 27:** Schematic representation of the ice sheet variations (rise and fall) along the Asuka flow line for the last 22 ka according to modeling experiments.

**Table III:** Minimum and maximum ice surface elevations compared to the present elevation for different places along the Asuka flow line, and minimum and maximum values for background temperature change and sea level. Model run with bedrock heating included.

Time	$\Delta T$	$\Delta H_{sl}$	$\Delta \bar{H}$	Divide	600	700	800	820	840	900
-143	-8.7									
-140				-30						
-137		-135	-62							
-133								69		
-132							49			
-131									102	
-130	2.9									99
-129						39				
-128					29					
-125		7	9							
-124								-7		
-117				1						
-116							-8			
-112									-25	-27
-63					-62	-48				
-22	-8.4									
-18		-130								
-17			-53							
-16				-24						
-13								57		
-10	0.5						42		56	30
-7						21				
-5					10					
-4		8.5								
-1									-1	-1
0	0	0	0	0	0	0	0	0	0	0

with Time in [ka],  $\Delta T$  the background temperature change [K],  $\Delta H_{sl}$  the eustatic change [m],  $\Delta \bar{H}$  the mean surface elevation compared to present [m], and the following columns surface changes compared to present [m] for the ice divide (Divide), at a distance 600 km from the divide (600), etc.

### 3.5 SURFACE GLACIER VELOCITIES OF GJELBREEN

#### 3.5.1 Area and Image Selection

Two vertical multispectral SPOT images (level 1B) were used for the calculation of the surface glacier velocities, each covering the same area of approximately 60 by 60 km with a ground resolution of 20 m. The first (*target*) image (151–688) was recorded on 21.02.1990, the second (*search*) image (151–690/8) almost four years later on 31.01.1994. They physically cover the south-central area of the Sør Rondane Mountains, i.e. the southern part of the glacier Gjelbreen surrounded by the rock outcrops Lynckeryggen, Mefjell and Dufekfjellet (72°20'S, 25°E, Figure 28). Matching was per-

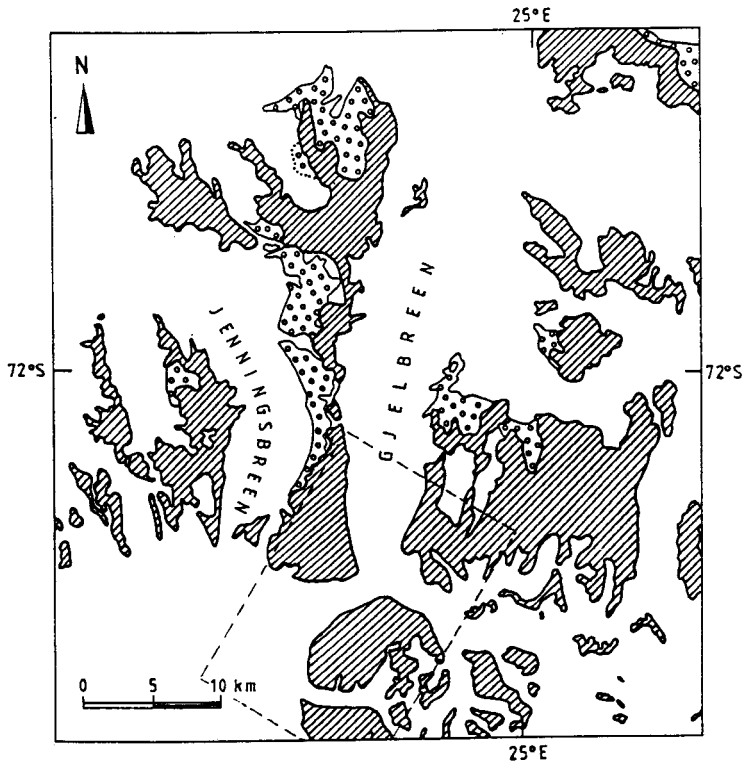


Figure 28: Detail map of central Sør Rondane area with reference to the satellite image display

formed on channel 2 of the SPOT images (SPOT XS2: 0.61–0.68  $\mu\text{m}$ ) since this carries most of the image information and the highest gray-value variability on both rock and ice surface (Pattyn and Declair, 1993).

### 3.5.2 Results and Evaluation

After image co-registration matching was performed on a smaller area of 700 by 1000 pixels (i.e. 14 by 20 km). For every five pixels in the target image a corresponding position was searched for in the search image. The size of the target and search array was taken as 15 by 19 pixels and the search space 19 by 23 pixels. A minimization of errors or 'mismatches' was obtained by adjusting the statistical threshold parameters: the minimal acceptable correlation coefficient was set to 0.6, the difference between the highest correlation value and the second highest in the correlation map (peak-above-second-peak) between 0 and 0.1, the difference between the highest correlation value and the mean value of the correlation map (peak-above-mean) between 0 and 0.2, and the maximum number of distinctive correlation maxima in the correlation map between 10 and 100.

A second evaluation was necessary, based on the glacier flow characteristics and the knowledge of the area. The image was subdivided in three areas, characterized by a difference in glacier flow orientation and surface velocity range and the velocity data were once more filtered based on their velocity magnitude and direction. The results of the operation are displayed in Figure 29. In order to obtain a proper idea of the global horizontal velocity field on Gjelbreen, 10 rectangular zones were selected for which the mean velocity was calculated, as shown in Figure 30. From Figure 30 it can be seen that the velocities in the ice fall area of Gjelbreen range from 16 to 52 m a<sup>-1</sup>, and beneath the ice fall decreasing to 26 m a<sup>-1</sup> in the northern part of the image. At the southern entrance of Gjelbreen the method failed to give accurate results, due to both relatively slow movement and a lack of rock outcrops to perform an accurate co-registration in this area.

The quality of the semi-automatic matching algorithm can furthermore be checked by a visual interpretation of crevasse displacements. Crevasses are very distinguishable features on the glacier surface and their position can accurately be determined by visual 'point picking' in the two images. From Figure 31 it can be seen that the quality of the automatic matching of points on crevasses is confirmed by the 'point picking' method.



Figure 29: Result of glacier surface motion after automatic matching and filtering

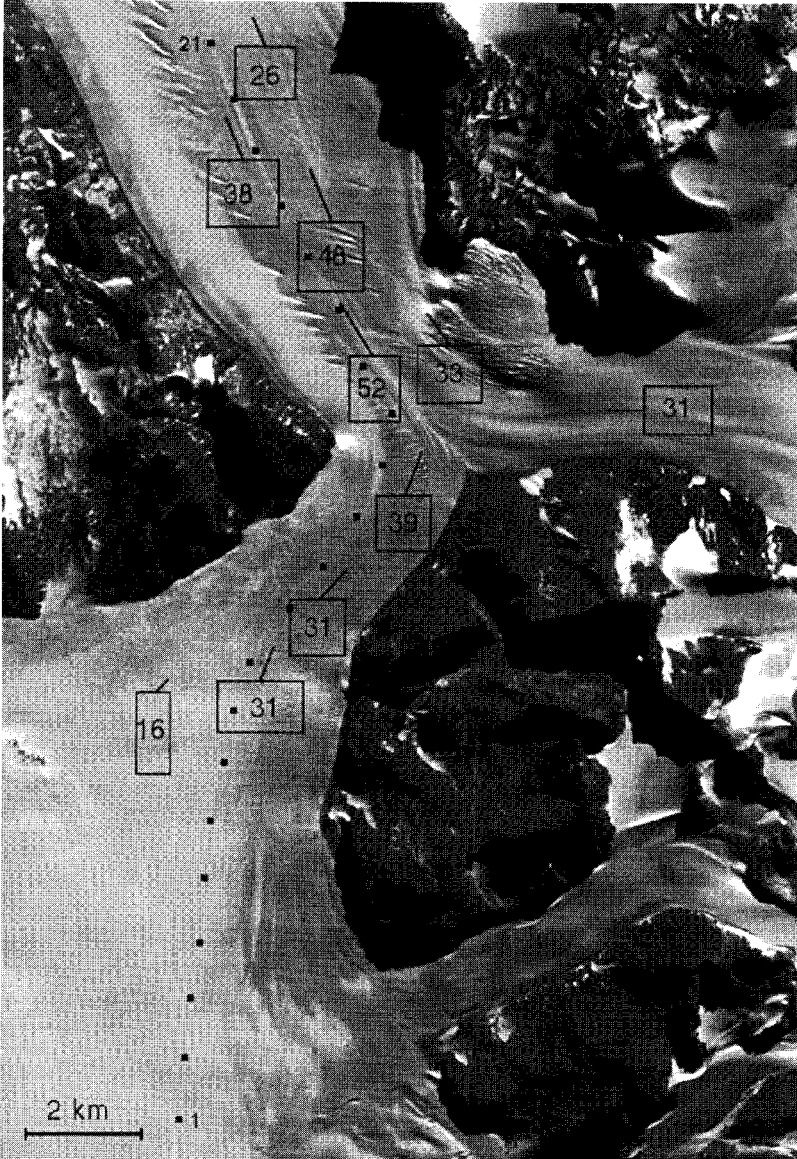


Figure 30: Mean surface velocity and direction for selected rectangular areas

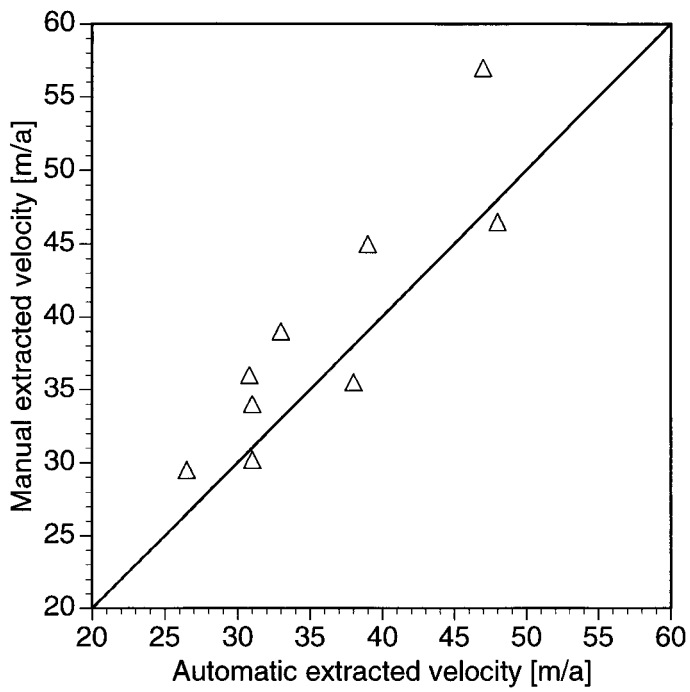


Figure 31: Comparison of automatic matched crevasse features with the 'point picking' method

## 4 DISCUSSION

### 4.1 ICE STREAM DYNAMICS

Payne (1995) showed a similar cyclic behavior with a thermo-mechanical ice sheet model, including a basal sliding mechanism of to the Budd sliding type 2 used in this paper. He found that the coupling of the ice flow field and the temperature evolution gives rise to limit cycles in the basal thermal regime of the ice sheet. These cycles are caused by the switching on and off of sliding as basal ice reaches the pressure melting point. Results of our work do not show this cyclic behavior for a sliding law in which the effect of basal water is not explicitly included. This is probably due to a lower tuning value in our experiments compared to the sliding law of Payne (1995). By comparing different basal motion laws it seems that those which depend on basal water are much more sensitive to this cyclic response, because they not only invoke an on and off switching when basal ice reaches pressure melting point, but the basal motion magnitude is also directly influenced by the amount of meltwater produced at the base.

The explanation of Payne (1995) on the limit cycle mechanism is slightly different from ours. He states that the oscillation is controlled by two sets of interactions: (i) the interaction of basal temperature with ice flow through the switching on and off of sliding and the additional heat generated by sliding and (ii) the interaction of ice flow and geometry through the influence of sliding on ice flow divergence and thickness, which cause a decrease in sliding (through a decrease in surface slope and hence basal shear stress) and a cooling at the base due to an increase in vertical heat diffusion (heat loss to the overlying ice). Whether the increase of diffusion is a result of an increase in advection is not clear, since Payne (1995) did not look at the process within the ice sheet, but only at the base.

The idea of self-oscillatory ice sheet systems based on thermodynamic principles, not necessary the same as described above, gained recently more interest as a possible explanation of Heinrich events in the Northern Atlantic. Heinrich events of the glacial North Atlantic are episodes of large ice-rafted debris deposition which are possibly associated with the onset of abrupt, irregular climate oscillations during the last glacial period (Heinrich, 1988; Broecker *et al.*, 1992). Recent studies (Bond *et al.*, 1992; Bond *et al.*, 1993) question the relation with climate oscillations and postulate that other mechanisms, such as internal ice-sheet dynamics, are responsible. MacAyeal (1994) presented a binge/purge mechanism: the growth phase occurs when the subglacial sediment is frozen and the Laurentide Ice Sheet is immobile on a rigid bed. The volume of the Laurentide Ice Sheet slowly grows during this phase according to the snow accumulation. The purge phase occurs when the basal sediment thaws and a basically lubricated discharge pathway (such as an ice stream) develops. The



volume of the ice sheet rapidly equilibrates to the reduced basal friction during this phase by dumping icebergs into the Labrador Sea. Besides this theoretical concept (kitchen–build oscillator as MacAyeal (1994) calls this) some scale models are able to explain a similar mechanism (Verbitsky and Saltzman, 1994).

Whether this kind of mechanism can be applied to Shirase Glacier is not clear. There is still no evidence on the basal characteristics of the glacier. One can only guess by looking at other large outlet glaciers draining large parts of the Antarctic ice sheet, such as Ice Stream B in West Antarctica. It is very likely that a soft bed and a sufficiently thick till layer will develop. The large deformation and basal velocities and the presence of a meltwater layer at the base probably account for relatively large erosion rates, hence the buildup of a till layer. Important to know is how far upstream this till layer is developed, what is its thickness and its strength. Basal motion can also originate from channel drainage along a hard bed or channels and cavities formed in a soft bed. Here, not the amount of water is important, but the normal pressure inside the conduits will play a decisive role (cfr. Röttlisberger–channels). Evidence for the existence of subglacial drainage channels is found along the Sôya Coast, at the edge of the present ice sheet.

Our experiments show that the oscillating behavior is independent of any basal motion law, as long as the basic hydrology in the ice sheet and its thermodynamics are taken into account and the glacier or stream moves sufficiently fast. Nevertheless, a precise knowledge on the basal characteristics will improve the validity of basal motion laws, since their present applicability is far from universal.

The experiments showed that there is no need for a massive drainage of ice in Lützow Holmbukta, as is the case with Heinrich events, to explain the large imbalance values observed in the drainage area. The ice sheet system remains stable under the present climatic conditions and the conditions reigning during the past 200,000 years. A runaway of ice is counteracted by the thermo-mechanical principle described in section 3.2 and a marine instability is unlikely to occur since most of the bedrock is lying above sea level.

## 4.2 PALEO ICE SHEET IN EAST DRONNING MAUD LAND

Reconstructing the glacial history of the Sør Rondane Mountains based on geomorphological findings alone is not evident, since only a few dated moraine heights exist. Nevertheless, many glacio-geological features in the Sør Rondane and elsewhere suggest that the present ice sheet in the mountains did hardly change over the last million years, as witnessed in the Dry Valleys region, Antarctica (Denton *et al.*, 1993).

With the modeling experiments we have tried to reconstruct the 'glacier transfer function' between the climate record and the geomorphological field observations. Our

results indicate that the present ice sheet in the vicinity of the mountains is close to its Last Glacial Maximum (LGM)<sup>2</sup> expansion, because of the large response time of the ice sheet to the climate signal and because the influence of grounding line movement (due to sea-level changes) is small inside the mountains and beyond (the coastal influence is dammed by the mountain range). Furthermore, our results indicate a different response to the climate signal for the inland ice sheet, the mountain area and the coastal area. Both conclusions are corroborated by field observations:

- The model results show a present-day ice sheet surface close to the maximum expansion, hence not necessarily small ice sheet fluctuations. A higher glacier stand of a few meters to a few tens of meters does not imply small glacier fluctuations either, since moraine deposits only witness higher glacier stands. The results shown in Table III are well in accord with the findings of Moriwaki *et al.* (1992): in the area polewards of the mountains the LGM surface lies only 10 m higher than the present ice surface, while the total amplitude of surface elevation changes during the last glacial–interglacial period yields more than 80 m.
- The regional (and time-lagged) difference in response of the ice sheet to the environmental change is also witnessed in the mountain range. In the southern part of the mountains an ice free valley (Viking Valley) exists with a bottom slightly lower than the surrounding ice surface. Tills on the valley floor suggest that the valley is ice free since perhaps the earliest Pleistocene. In the central part of the mountains moraines were found lying 3 m above the present surface (dated 36 ka BP) and in the northern part 40 m higher than the present surface (dated approximately 150 ka BP) (Moriwaki *et al.*, 1992).

Recent geomorphological investigations in other ice free oases bordering the East Antarctic ice sheet also suggest that the last glacial maximum ice sheet (LGM) was only slightly bigger than at present and it is very unlikely that it extended to the edge of the continental shelf. From data on the altitudes and ages of raised beaches from the Ross embayment and East Antarctica, Colhoun *et al.* (1992) infer a mean grounding line advance of 30 km. They also conclude that the contribution of the ice sheet to the world-wide sea-level drop should be lower than previous estimates.

In the Transantarctic Mountains, Denton *et al.* (1989b) observe a slight thickening near the polar plateau, notwithstanding substantial thickening at the mouth of the glaciers that end in the Ross Ice Shelf. The last glacial maximum profile of Taylor Glacier (Dry Valleys area) was not larger than now. The surface profile of Mill and Beardmore glaciers rises within 35–40 m near the polar plateau, confirming that the

---

<sup>2</sup>Like most authors we use the term 'last glacial maximum' (LGM) to denote the maximum expansion and size of the ice sheet that existed during the last glacial–interglacial period. Note however that LGM does not point at a specific moment in time.

central ice cap is hardly influenced by the grounding of outlet glaciers (Denton *et al.*, 1989a). Hatherton glacier rises 20-70 m above the present surface (Bockheim *et al.*, 1989). At the other side of the east Antarctic continent, in the Prince Charles Mountains near Lambert Glacier, Mabin (1992) finds that the profile of the last glacial maximum ice sheet was only 100 m above the present surface and he further rejects the idea of extensive grounding of the Amery Ice Shelf. In Lützow-Holmbukta, Enderby Land, the age and elevation characteristics of raised beaches suggest that there has been minimal Antarctic ice sheet expansion since the last glacial maximum (Hayashi and Yoshida, 1994).

Field evidence suggests little change and probably a slight lowering of McMurdo Dome inland from Taylor valley on the East Antarctic Plateau. Our experiments (Figure 26 on page 43) also suggest that the elevation of the polar plateau, near the ice divide, was lower during the last glacial maximum, a picture which is in agreement with the analysis of Lorius *et al.* (1984) and Jouzel *et al.* (1989). For central parts of Antarctica, the last glacial maximum ice sheet was thinner than the present ice sheet. Central parts of the ice sheet respond quickly to changes in the rate of snow accumulation (Whillans, 1981) and such a thinning is consistent with lower accumulation during the glacial period.

Less evidence is available on the timing of deglaciation. In the Ross Ice Shelf area, the recession of grounded ice sheet from the western Ross Embayment was underway at 13 ka BP and completed by 6600 a BP (Denton *et al.*, 1989b). However, this recession is probably triggered by the West Antarctic ice sheet. Colhoun (1991) states that deglaciation along the oases of the East Antarctic ice sheet between 60° and 120°E started around 10 ka BP, and that some of the oases had attained approximately their present sizes around 6-5 ka BP, while others (Bunger Hills oasis) remained even unglaciated during this period (Colhoun and Adamson, 1995).

As our experiments showed, thermo-mechanics have not only an effect on the surface elevation changes of the ice sheet, but also on the reaction time of the ice sheet to climatic change. Introducing bedrock heating increases the time lagged response, especially of the inland ice sheet. Another important factor in the timing of deglaciation is the interplay between the time lagged response of the ice sheet to warmer temperatures (which soften the ice), the increase in surface mass balance and the timing of sea-level changes during the glacial–interglacial transition.

## 5 CONCLUSION

In this study we examined the regional dynamic behavior of the East Antarctic ice sheet by carrying out a detailed numerical analysis of the ice sheet system in East Dronning Maud Land and Enderby Land between 20° and 40°E.

For this purpose we developed a flexible and multi-purpose flow line model allowing us to study the relevant glaciological processes in ice stream behavior on the one hand and capable of linking, on sound physical principles, the observed climatic signal from ice core data with the geomorphological data as observed in the ice free areas, on the other hand. With respect to the observed glaciological parameters we also developed a method for deriving glacier variations from sequential satellite images by an automatic matching technique.

The analysis itself focussed on the period of the last 200,000 years with special interest in the last glacial–Holocene transition and the present day dynamical situation:

- Since field evidence from Shirase Drainage Basin reports a rapid thinning of the ice sheet, model experiments were carried out to shed a light on the relevant physical processes responsible for ice stream behavior. Indeed, from preliminary experiments (Pattyn and Declerq, 1995a) it was found that the large thinning rate in Shirase Drainage Basin could not be explained as a response to the climate signal alone. Some other mechanism should account for this. By carrying out simulations with different basal boundary conditions, a thermally regulated cyclic behavior, related to the hydraulic conditions at the bed (water pressure, basal melting and meltwater flow) could be observed, giving rise to a partial disintegration of the ice sheet (Pattyn, 1996). Yet, the ice loss was confined to the stream area and did not influence the inland ice sheet near the Polar Plateau. The high imbalance values (in accord with observations) could be explained by the small period in the cyclicity, hence a large ice discharge was not necessary. Whether this mechanism applies to Shirase Glacier awaits future field work to disentangle the basal properties of this fast-flowing outlet glacier.
- Recent glacio-geological and geomorphological field evidences in the neighboring Sør Rondane Mountains point – as elsewhere in Antarctica – to a relative stable ice sheet cover during the last million years. This was confirmed by applying different model scenarios of the behavior of Gjølbreven, an outlet glacier of this mountain range. Results of the 'best fit' scenario, i.e. the model outcome which is closest to the field evidence, showed that the present ice sheet in the Sør Rondane is close to its maximum position of the last glacial–interglacial period. This proves that the ice sheet is out of phase with the climatic signal and explains the small observed differences in glacier stand between the present and

the maximum. However, over the last 200,000 years the glacier variations amount to 100–200 m. Our modeling experiments clearly indicate that both the position on the glacier (coastal, mountain and inland ice sheet) and the timing of the response is essential to make a comparison with field observations elsewhere.

## **ACKNOWLEDGEMENTS**

This paper forms a contribution to the Belgian Scientific Research Program on Antarctica (Federal Office for Scientific, Technical and Cultural Affairs (OSTC)), contract A3/03/002. The authors are deeply indebted to O. Watanabe, Y. Fujii and K. Moriwaki of the National Institute of Polar Research (NIPR), Tokyo, Japan and R. Naruse (University of Hokkaido) for helpful discussions on the dynamics of Shirase Glacier and on paleo-reconstructions of the ice sheet in Dronning Maud Land, and for supplying all data necessary for carrying out this study. We would also like to thank A. Payne for the many suggestions and discussions on ice stream dynamics. The SPOT image 151–688 (Figures 29 and 30) was reproduced by permission of SPOT IMAGE.

## References

- Ageta, Y., Nishio, F., Fujii, Y., and Moriwaki, K. 1995. Ice sheet surface. In Higashi, A., editor, *Antarctica, East Queen Maud Land, Enderby Land; Glaciological Folio*. Natl Inst. Polar. Res. (Tokyo).
- Alley, R.B., Blankenship, D.D., Rooney, S.T., and Bentley, C.R. 1989. Water-pressure coupling of sliding and bed deformation: III. application to Ice Stream B, Antarctica. *J. Glaciol.*, 35(119):130–139.
- Alley, R.B. 1989. Water-pressure coupling of sliding and bed deformation: I. water system. *J. Glaciol.*, 35(119):108–118.
- Bindschadler, R.A. and Scambos, T.A. 1991. Satellite-derived velocity field of an Antarctic ice stream. *Science*, 252:242–246.
- Bindschadler, R.A. 1983. The importance of pressurized subglacial water in separation and sliding at the glacier bed. *J. Glaciol.*, 29(101):3–19.
- Bockheim, J.G., Wilson, S.C., Denton, G.H., Andersen, B.G., and Stuiver, M. 1989. Late Quaternary ice-surface fluctuations of Hatherton Glacier, Transantarctic Mountains. *Quat. Res.*, 31:229–254.
- Bond, G., Heinrich, H., Broecker, W., Labeyrie, L., McManus, J., Andrews, J., Huon, S., Jantschik, R., Clasen, S., Simet, C., Tedesco, K., Klas, M., Bonani, G., and Ivy, S. 1992. Evidence for massive discharges of icebergs into the North Atlantic Ocean during the last glacial period. *Nature*, 360:245–249.
- Bond, G., Broecker, W., Johnsen, S., McManus, J., Labeyrie, L., Jouzel, J., and Bonani, G. 1993. Correlations between climate records from North Atlantic sediments and Greenland ice. *Nature*, 365:143–147.
- Broecker, W., Bond, G., Klas, M., Clark, E., and McManus, J. 1992. Origin of the Northern Atlantic's Heinrich events. *Clim. Dyn.*, 6:245–250.
- Brotchie, J.F. and Silvester, R. 1969. On crustal flexure. *J. Geophys. Res.*, 74(22):5240–5252.
- Budd, W.F. and Jenssen, D. 1987. Numerical modelling of the large-scale basal water flux under the West Antarctic ice sheet. In van der Veen, C.J. and Oerlemans, J., editors, *Dynamics of the West Antarctic Ice Sheet*, pages 293–320. D. Reidel (Dordrecht).
- Budd, W.F., Jenssen, D., and Smith, I.N. 1984. A three-dimensional time-dependent model of the West Antarctic ice sheet. *Ann. Glaciol.*, 5:29–36.
- Colhoun, E.A. and Adamson, D.A. 1995. A review of geomorphological research in bunger hills and implications for expansion of the East Antarctic ice sheet during the Last Glacial Maximum. *7th International Symposium on Antarctic Earth Sciences, 10–15 September 1995, Sienna (Italy)*, Abstracts:85.
- Colhoun, E.A., Mabin, M.C.G., Adamson, D.A., and Kirk, R.M. 1992. Antarctic ice vol-

- ume and contribution to sea-level fall at 20,000 yr BP from raised beaches. *Nature*, 358:316–318.
- Colhoun, E.A. 1991. Geological evidence for changes in the East Antarctic ice sheet (60–120E) during the last glaciation. *Polar Rec.*, 27(163):345–355.
- Denton, G.H. and Hughes, T.J. 1981. *The Last Great Ice Sheets*. J. Wiley (New York).
- Denton, G.H., Bockheim, J.G., Wilson, S.C., Leide, J.E., and Andersen, B.G. 1989a. Late Quaternary ice-surface fluctuations of Beardmore Glacier, Transantarctic Mountains. *Quat. Res.*, 31:183–209.
- Denton, G.H., Bockheim, J.G., Wilson, S.C., and Stuiver, M. 1989b. Late Wisconsin and early Holocene glacial history, Inner Ross Embayment, Antarctica. *Quat. Res.*, 31:151–182.
- Denton, G.H., Sugden, D.E., Marchant, D.R., Hall, B.L., and Wilch, T.I. 1993. East Antarctic ice sheet sensitivity to Pliocene climatic change from a Dry Valleys perspective. *Geografiska Annaler*, 75A(4):155–204.
- Fujii, Y. 1981. Aerophotographic interpretation of surface features and estimation of ice discharge at the outlet of the Shirase Drainage Basin, Antarctica. *Nankyoku Shiryô (Antarct. Rec.)*, 72:1–15.
- Fujita, S., Ikeda, N., Azuma, N., Hondoh, T., and Mae, S. 1991. Numerical estimation of 10,000 years later equilibrium ice sheet profile in the Shirase Drainage Basin, East Antarctica. *Nankyoku Shiryô (Antarct. Rec.)*, 35:12–29.
- Hayashi, M. and Yoshida, Y. 1994. Holocene raised beaches in the Lützow–Holm Bay region, East Antarctica. *Mem. Natl Inst. Polar Res., Spec. Issue*, 50:49–84.
- Heinrich, H. 1988. Origin and consequences of cyclic ice rafting in the Northeast Atlantic Ocean during the past 130,000 years. *Quat. Res.*, 29:142–152.
- Hindmarsh, R.C.A. 1993. Qualitative dynamics of marine ice sheets. In Peltier, W.R., editor, *Ice in the Climate System*, NATO ASI Series I (12), pages 67–99. Springer-Verlag (Berlin).
- Hollin, J.T. 1962. On the glacial history of Antarctica. *J. Glaciol.*, 4:173–195.
- Hutter, K. 1993. Thermo-mechanically coupled ice-sheet response — cold, polythermal, temperate. *J. Glaciol.*, 39(131):65–86.
- Huybrechts, P. and Oerlemans, J. 1988. Evolution of the East Antarctic ice sheet: a numerical study of thermo-mechanical response patterns with changing climate. *Ann. Glaciol.*, 11:52–59.
- Huybrechts, P. 1990. A 3-D model for the Antarctic ice sheet: a sensitivity study on the glacial-interglacial contrast. *Clim. Dyn.*, 5:79–92.
- Huybrechts, P. 1992. The Antarctic ice sheet and environmental change: a three-dimensional modelling study. *Berichte für Polarforschung*, 99:1–241.
- Jouzel, J. and Merlivat, L. 1984. Deuterium and oxygen 18 in precipitation: Modelling of the isotopic effects during snow formation. *J. Geophys. Res.*, 89(D7):11749–11757.

- Jouzel, J., Raisbeck, G., Benoist, J.P., Yiou, F., Lorius, C., Raynaud, D., Petit, J.R., Barkov, N.I., Korotkevitch, Y.S., and Kotlyakov, V.M. 1989. A comparison of deep Antarctic ice cores and their implication for climate between 65,000 and 15,000 years ago. *Quat. Res.*, 31:135–150.
- Jouzel, J., Barkov, N.I., Barnola, J.M., Bender, M., Chappellaz, J., Genthon, C., Kotlyakov, V.M., Lipenkov, V., Lorius, C., Petit, J.R., Raynaud, D., Raisbeck, G., Ritz, C., Sowers, T., Stievenard, M., Yiou, F., and Yiou, P. 1993. Extending the Vostok ice-core record of palaeoclimate to the penultimate glacial period. *Nature*, 364:407–412.
- Kameda, T., Nakawo, M., Mae, S., Watanabe, O., and Naruse, R. 1990. Thinning of the ice sheet estimated from total gas content of ice cores in Mizuho Plateau, East Antarctica. *Ann. Glaciol.*, 14:131–135.
- Kamiyama, K., Furukawa, T., Maeno, H., Kishi, T., and Kanao, M. 1994. Glaciological data collected by the 33rd Japanese Antarctic Research Expedition in 1992. *JARE Data Reports*, 194:1–67.
- Kennett, J.P. and Hodell, D.A. 1993. Evidence for relative climatic stability of Antarctica during the Early Pliocene: A marine perspective. *Geografiska Annaler*, 75A(4):205–220.
- Le Muer, E. and Huybrechts, P. 1996. A comparison of different ways of dealing with isostasy: Examples from modelling the Antarctic ice sheet during the last glacial cycle. *Ann. Glaciol.*, 23:in press.
- Lorius, C., Raynaud, D., Petit, J.R., Jouzel, J., and Merlivat, L. 1984. Late glacial maximum—Holocene atmospheric and ice thickness changes from Antarctic ice core studies. *Ann. Glaciol.*, 5:88–94.
- Lorius, C., Jouzel, J., Ritz, C., Merlivat, L., Barkov, N.I., Korotkevich, Y.S., and Kotlyakov, V.M. 1985. A 150,000-year climatic record from Antarctic ice. *Nature*, 316:591–596.
- Mabin, M.C.G. 1992. Late Quaternary ice-surface fluctuations of the Lambert Glacier. In Yoshida, Y., editor, *Recent Progress in Antarctic Earth Science*, pages 683–687. Terra Sci. Publ. (Tokyo).
- MacAyeal, D.R. 1994. Binge/purge oscillations of the Laurentide ice sheet as a cause of the North Atlantic Heinrich Events. *Paleoceanography*.
- Mae, S. and Naruse, R. 1978. Possible causes of ice sheet thinning in the Mizuho Plateau. *Nature*, 273:291–292.
- Mae, S. and Yoshida, M. 1987. Airborne radio echo-sounding in Shirase Glacier Drainage Basin, Antarctica. *Ann. Glaciol.*, 9:160–165.
- Mae, S. 1979. The basal sliding of a thinning ice sheet, Mizuho Plateau, East Antarctica. *J. Glaciol.*, 24(90):53–61.
- Mahaffy, M.W. 1976. A three-dimensional numerical model of ice sheets: Tests on the



- Barnes Ice Cap, Northwest Territories. *J. Geophys. Res.*, 81:1059–1066.
- Mitchell, A.R. and Griffiths, D.R. 1980. *The finite Difference Method in Partial Differential Equations*. J. Wiley (Chisester).
- Moriwaki, K. and Yoshida, Y. 1983. Submarine topography of Lützow–Holm Bay, Antarctica. *Mem. Natl Inst. Polar Res., Spec. Issue*, 28:247–258.
- Moriwaki, K., Hirakawa, K., and Matsuoka, N. 1991. Weathering stage of till and glacial history of the central Sør Rondane Mountains, East Antarctica. *Proc. NIPR Symp. Antarct. Geosci.*, 5:99–111.
- Moriwaki, K., Hirakawa, K., Hayashi, M., and Iwata, S. 1992. Late Cenozoic history in the Sør Rondane Mountains, East Antarctica. In Yoshida, Y., editor, *Recent Progress in Antarctic Earth Science*, pages 661–667. Terra Sci. Publ. (Tokyo).
- Nagao, M., Nakawo, M., and Higashi, A. 1984. Computer simulation of the ice sheet in the Shirase Basin, Antarctica. *Ann. Glaciol.*, 5:219–221.
- Naruse, R. 1979. Thinning of the ice sheet in Mizuho Plateau, East Antarctica. *J. Glaciol.*, 24(90):45–52.
- Nishio, F. and Uratsuka, S. 1991. Subglacial water layer and grounding line derived from backscattering coefficients of radio echo sounding in the Shirase Glacier and Roi Baudouin Ice Shelf, East Antarctica. *Proc. NIPR Symp. Polar Meteorol. Glaciol.*, 4:93–102.
- Nishio, F., Mae, S., Ohmae, H., Takahashi, S., Nakawo, M., and Kawada, K. 1989. Dynamical behavior of the ice sheet in Mizuho Plateau, East Antarctica. *Proc. NIPR Symp. Polar Meteorol. Glaciol.*, 2:97–104.
- Nishio, F., Uratsuka, S., and Ohmae, K. 1995. Bedrock topography. In Higashi, A., editor, *Antarctica, East Queen Maud Land, Enderby Land; Glaciological Folio*. Natl Inst. Polar. Res. (Tokyo).
- Nye, J.F. 1965. The flow of a glacier in a channel of rectangular, elliptic or parabolic cross-section. *J. Glaciol.*, 5:661–690.
- Oerlemans, J. 1982. A model of the Antarctic ice sheet. *Nature*, 290:770–772.
- Paterson, W.S.B. 1994. *The Physics of Glaciers*. Pergamon (Oxford), 3rd edition.
- Pattyn, F. and Declair, H. 1993. Satellite monitoring of ice and snow in the Sør Rondane Mountains, Antarctica. *Ann. Glaciol.*, 17:41–48.
- Pattyn, F. and Declair, H. 1995a. Numerical simulation of Shirase Glacier, East Queen Maud Land, Antarctica. *Proc. NIPR Symp. Polar. Meteorol. Glaciol.*, 9:87–109.
- Pattyn, F. and Declair, H. 1995b. Subglacial topography in the central Sør Rondane Mountains, East Antarctica: Configuration and morphometric analysis of valley cross profiles. *Nankyoku Shiryô (Antarct. Rec.)*, 39(1):1–24.
- Pattyn, F. 1992. Topographic mapping from SPOT in polar regions. *Int. Arch. Photogramm. Rem. Sens.*, 29(B4):472–476.
- Pattyn, F. 1996. Numerical modelling of a fast flowing outlet glacier: Experiments with

- different basal conditions. *Ann. Glaciol.*, 23:in press.
- Payne, A.J. 1995. Limit cycles in the basal thermal regime of ice sheets. *J. Geophys. Res.*, 100(B3):4249–4263.
- Press, W.H., Teukolsky, S.A., Vetterling, W.T., and Flannery, B.P. 1992. *Numerical Recipes in C: The Art of Scientific Computing*. Cambridge University Press (Cambridge), 2nd edition.
- Ritz, C. 1987. Time dependent boundary conditions for calculation of temperature fields in ice sheets. *IAHS Publ.*, 170:207–216.
- Ritz, C. 1989. Interpretation of the temperature profile measured at Vostok, East Antarctica. *Ann. Glaciol.*, 12:138–144.
- Rosenholm, D. 1985. Digital matching of simulated SPOT images. *Fotogrammetrisk Meddelanden*, 2(50):1–76.
- Röttlisberger, H. 1972. Water pressure in intra- and subglacial channels. *J. Glaciol.*, 11(62):177–203.
- Satow, K. and Kikuchi, T. 1995. The 10 m snow temperature in the ice sheet. In Higashi, A., editor, *Antarctica, East Queen Maud Land, Enderby Land; Glaciological Folio*. Natl Inst. Polar. Res. (Tokyo).
- Scambos, T.A. and Bindschadler, R. 1993. Complex ice stream flow revealed by sequential satellite imagery. *Ann. Glaciol.*, 17:177–182.
- Slater, J.G., Jaupart, C., and Galson, D. 1980. The heat flow through oceanic and continental crust and the heat loss of the earth. *Rev. Geophys. Space Phys.*, 18:289–311.
- Shackleton, N.J. 1987. Oxygen isotopes, ice volume and sea level. *Quat. Sci. Rev.*, 6:183–190.
- Takahashi, S. and Watanabe, O. 1995. Snow accumulation (surface mass balance). In Higashi, A., editor, *Antarctica, East Queen Maud Land, Enderby Land; Glaciological Folio*. Natl Inst. Polar. Res. (Tokyo).
- Thomas, R.H. 1973. The creep of ice shelves. *J. Glaciol.*, 12(64):45–53.
- Toh, H. and Shibuya, K. 1992. Thinning rate of ice sheet on Mizuho Plateau, East Antarctica, determined by GPS differential positioning. In Yoshida, Y., editor, *Recent Progress in Antarctic Earth Science*, pages 579–583. Terra Sci. Publ.
- Turcotte, D.L. and Schubert, G. 1982. *Geodynamics*. John Wiley (New York).
- Ungar, S.G., Merry, C.J., Irish, R., McKim, H.L., and Miller, M.S. 1988. Extraction of topography from side-looking satellite systems — a case study with SPOT simulation data. *Rem. Sens. Environ.*, 26:51–73.
- van der Veen, C.J. and Whillans, I.M. 1989. Force budget: I. theory and numerical methods. *J. Glaciol.*, 35(119):53–60.
- van der Veen, C.J. 1987. Longitudinal stresses and basal sliding: a comparative study. In van der Veen, C.J. and Oerlemans, J., editors, *Dynamics of the West Antarctic Ice*



- Sheet*, pages 223–248. D. Reidel (Dordrecht).
- van der Veen, C.J. 1989. A numerical scheme for calculating stresses and strain rates in glaciers. *Math. Geol.*, 21(3):363–377.
- Verbitsky, M.Y. and Saltzman, B. 1994. Heinrich-type glacial surges in a low-order dynamical climate model. *Clim. Dyn.*
- Walder, J.S. and Fowler, A. 1994. Channelized subglacial drainage over a deformable bed. *J. Glaciol.*, 40(134):3–15.
- Watanabe, O., Fujii, Y., Nishio, F., and Motoyama, H. 1992. Position, elevation, ice thickness and bedrock elevation of stations along the routes in East Queen Maud Land and Enderby Land, East Antarctica. *JARE Data Reports*, 180:1–143.
- Weertman, J. and Birchfield, G.E. 1982. Subglacial water flow under ice streams and West Antarctic ice sheet stability. *Ann. Glaciol.*, 3:316–320.
- Whillans, I.M. 1981. Reaction of the accumulation zone portions of glaciers to climatic change. *J. Geophys. Res.*, 86:4272–4282.
- Whillans, I.M. 1987. Force budget of ice sheets. In van der Veen, C.J. and Oerlemans, J., editors, *Dynamics of the West Antarctic Ice Sheet*, pages 17–36. D. Reidel (Dordrecht).
- Willaert, D. 1995. *Het Bepalen van Gletsjersnelheden in de Sør Rondane, Antarctica uitgaande van Sequentiële Satellietbeelden*. Master Thesis (VUB).

## A APPENDIX

Before attempting a derivation of the two-dimensional velocity field a new vertical co-ordinate, scaled to the local ice thickness, is introduced. This stretched dimensionless vertical co-ordinate is defined by  $\zeta = (H + h - z)/H$ , resulting in  $\zeta = 0$  at the ice surface and  $\zeta = 1$  at the base of the ice sheet. The vertical domain was sub-divided into 20 layers, with varying thickness so that  $\zeta_k = a_0 + a_1 k + a_2 k^2$ , for  $k = 1$  to 21 obeys a polynomial based on the fixed co-ordinates  $\zeta_1 = 0.0$ ,  $\zeta_{20} = 0.985$ , and  $\zeta_{21} = 1.0$ . The lowermost grid spacing thus is 0.015, gradually increasing towards the top of the ice column.

### A.1 DEFORMATION MODEL I

In the first model we consider that the deformation of ice is solely driven by shear stresses, i.e. all longitudinal deviatoric stresses and vertical resistive stresses are neglected. This limits the model use to cases where basal motion is relatively unimportant and requires large grid spacings so that small scale bedrock irregularities are smoothed out. This model configuration is generally applied in most large-scale ice sheet models (Mahaffy, 1976; Oerlemans, 1982; Huybrechts and Oerlemans, 1988). Consider  $\tau'_{xx} = 0$ ,  $R_{zz} = 0$  and introducing the scaled co-ordinates, Eq.(7) is written as

$$\tau'_{xz}(\zeta) = \zeta \tau_d \quad (38)$$

Assuming that  $\partial w/\partial z \ll \partial u/\partial x$ , the flow law Eq.(11) is integrated from the bottom to a height  $\zeta$  yielding an expression for the horizontal velocity field.

$$u(\zeta) = 2H\tau_d \int_{\zeta}^1 A(T^*) \zeta d\zeta - u(1) \quad (39)$$

with  $u(1)$  the basal velocity.

### A.2 DEFORMATION MODEL II

An overview of the arithmetic derivation of this model is given in Pattyn and Declair (1995a). The same simplifications for Model I apply, except that now the longitudinal deviatoric stress ( $\tau'_{xx}$ ) is taken into account, so that after vertical scaling Eq.(7) reads

$$\tau'_{xz}(\zeta) = \zeta \tau_d + 2 \frac{\partial}{\partial x} \left[ H \int_0^{\zeta} \tau'_{xx}(\zeta) d\zeta \right] + 2\tau'_{xx}(\zeta) \Delta_{\zeta} \quad (40)$$

with  $\Delta_{\zeta} = \partial(H + h)/\partial x - \zeta \partial H/\partial x$ . The horizontal velocity then yields

$$u(\zeta) = 2H \int_{\zeta}^1 A(T^*) (\tau_{xx}'^2(\zeta) + \tau_{xz}'^2(\zeta))^{\frac{n-1}{2}} \tau'_{xz}(\zeta) d\zeta + u(1) \quad (41)$$

We need furthermore an expression for  $\tau'_{xx}$ , which is obtained from the definition of the flow law

$$\left(\frac{\partial u}{\partial x}\right)_{\zeta} + \frac{1}{H} \frac{\partial u}{\partial \zeta} \Delta \zeta - A(T^*) \tau'_{xx}{}^3(\zeta) + A(T^*) \tau'_{xz}{}^2(\zeta) \tau'_{xx}(\zeta) = 0 \quad (42)$$

for ( $n = 3$ ). This equation has the form of  $a + bx + cx^3 = 0$ , for ( $x = \tau'_{xx}(\zeta)$ ). An efficient algorithm for one-dimensional root finding is the Newton–Raphson method using the derivative or a hybrid algorithm that takes a bisection step whenever Newton–Raphson would take a solution out of bounds. However, in some cases, Newton–Raphson fails and Laguerre's method, a general complex root finding algorithm, was applied (Press *et al.*, 1992). The calculation of the horizontal velocity field is performed iteratively based on the above described equations.

### A.3 DEFORMATION MODEL III

Finally, the third model description (Pattyn, 1996) incorporates all relevant stresses. However, the solution scheme is somewhat less straightforward and can basically be found in van der Veen (1989). Instead of writing an expression for the shear stress, the basic equation is written as a function of strain-rates. Making use of the flow law,  $\tau'_{ij} = A(T^*)^{-1/n} \dot{\epsilon}_e^{(1/n)-1} \dot{\epsilon}_{ij}$ , and substituting the scaled co-ordinate system, Eq.(7) is integrated from the bottom of the ice sheet to a height  $\zeta$ , yielding

$$\begin{aligned} \dot{\epsilon}_{xz}(\zeta) = & A(T^*)^{1/n} \dot{\epsilon}_e^{1-(1/n)} (\tau_b + (\zeta - 1)\tau_d) - \\ & - A(T^*)^{1/n} \dot{\epsilon}_e^{1-(1/n)} \frac{\partial}{\partial x} \left[ \int_{\zeta}^1 2HA(T^*)^{-1/n} \dot{\epsilon}_e^{(1/n)-1} \dot{\epsilon}_{xx}(\zeta) d\zeta' \right] + \\ & + 2\Delta_{\zeta} \dot{\epsilon}_{xx}(\zeta) + A(T^*)^{1/n} \dot{\epsilon}_e^{1-(1/n)} \Delta_{\zeta} R_{zz} - \\ & - A(T^*)^{1/n} \dot{\epsilon}_e^{1-(1/n)} \frac{\partial}{\partial x} \left[ \int_{\zeta}^1 HR_{zz}(\zeta) d\zeta' \right] \end{aligned} \quad (43)$$

where  $\tau_b = \tau'_{xz}(1) - (2\tau'_{xx}(1) + R_{zz}(1))\partial h/\partial x$ . Repeating the same arithmetic for Eq.(8), the vertical resistive stress yields

$$\begin{aligned} R_{zz}(\zeta) = & \sigma_n + \Delta_{\zeta} A(T^*)^{-1/n} \dot{\epsilon}_e^{(1/n)-1} \dot{\epsilon}_{xz}(\zeta) - \\ & - \frac{\partial}{\partial x} \left[ \int_{\zeta}^1 2HA(T^*)^{-1/n} \dot{\epsilon}_e^{(1/n)-1} \dot{\epsilon}_{xz}(\zeta) d\zeta' \right] \end{aligned} \quad (44)$$

where  $\sigma_n = R_{zz}(1) - \tau'_{xz}(1)\partial h/\partial x$ . An expression for the longitudinal strain rate is derived from the relation between strain-rates and velocity gradients and the incompressibility of ice, which, after some manipulation results in

$$\dot{\epsilon}_{xx} = \left[ \left(\frac{\partial u}{\partial x}\right)_{\zeta} + \Delta_{\zeta} \left(\frac{\partial w}{\partial x}\right)_{\zeta} - 2\Delta_{\zeta} \dot{\epsilon}_{xz} \right] / (1 - \Delta_{\zeta}^2) \quad (45)$$

Also needed are expressions for vertical velocity gradients,

$$\frac{\partial u}{\partial \zeta} = 2\dot{\epsilon}_{xz} - \left( \frac{\partial w}{\partial x} \right)_{\zeta} - \Delta_{\zeta} \dot{\epsilon}_{xx} \quad (46)$$

$$\frac{\partial w}{\partial \zeta} = -\dot{\epsilon}_{xx} \quad (47)$$

The main part of the numerical scheme consists of solving the balance equation for the shear strain-rate at general depth  $\zeta$ . Therefore, velocities at that depth layer and the velocities of the layer underneath need to be known. The integration starts at the bedrock ( $\zeta = 1$ ), conditioned by a basal velocity and which is governed by both basal motion mechanisms, ice stream and ice shelf flow. Furthermore, the basal velocity is influenced by the two-dimensional stress field and vice versa, so that linking of the two mechanisms should be performed dynamically. van der Veen (1989) offers a solution for the integration of the flow field starting from the bed. The numerical computation is however rather time consuming, and increases when eventually a basal boundary condition is linked to the flow field. However, by choosing good initial estimates to the basal drag and normal stress, convergence can be attained rather rapidly, even when basal velocity is influenced by the basal drag. The final flow field determination is stopped when the stress-free surface condition is fulfilled, i.e. Eq.(9) and (10).



RESEARCH CONTRACT A3/11/002

**CHEMICAL AND ISOTOPIC  
COMPOSITION OF ICE FROM  
ANTARCTIC ICE SHELVES :  
IMPLICATIONS FOR GLOBAL CHANGE**

R. SOUCHEZ<sup>1</sup>,  
J.-L. TISON and  
R. LORRAIN

DÉPARTEMENT DES SCIENCES DE LA TERRE  
ET DE L'ENVIRONNEMENT  
UNIVERSITÉ LIBRE DE BRUXELLES - C.P. 160/03  
Avenue F.D. Roosevelt, 50  
B-1050 Brussels  
Belgium

<sup>1</sup> Corresponding author E-mail : [glaciol@ulb.ac.be](mailto:glaciol@ulb.ac.be)





## TABLE OF CONTENT

<b>ABSTRACT</b>	<b>1</b>
<b>INTRODUCTION</b>	<b>2</b>
<b>MATERIALS AND METHOD</b>	<b>2</b>
<b>A CASE STUDY OF PROCESSES OCCURRING NEAR A GROUNDING LINE</b>	<b>4</b>
<b>Generalities</b>	<b>4</b>
<b><math>\delta D</math>-<math>\delta^{18}O</math> characteristics of basal ice</b>	<b>6</b>
<b>Texture-isotope relationships in the marine ice</b>	<b>9</b>
<b>Conclusion</b>	<b>15</b>
<b>A CASE STUDY OF ICE SHELF-OCEAN INTERACTION FOR A SMALL ICE SHELF</b>	<b>15</b>
<b>Generalities</b>	<b>15</b>
<b>Characteristics of Ross Sea Waters in the Terra Nova Bay area</b>	<b>17</b>
<b>Sea Water Characteristics in Front of Hell's Gate Ice Shelf</b>	<b>18</b>
<b>Marine ice characteristics</b>	<b>21</b>
<b>Evidence for dilution at the ice-ocean interface</b>	<b>25</b>
<b>Behaviour of the K/Mg ratio</b>	<b>29</b>
<b>"Orbicular" versus "Banded" frazil</b>	<b>37</b>
<b>Conclusion</b>	<b>41</b>
<b>GENERAL CONCLUSION</b>	<b>42</b>
<b>ACKNOWLEDGMENTS</b>	<b>43</b>
<b>REFERENCES</b>	<b>43</b>



## ABSTRACT

In the context of global warming, the question of the stability of Antarctic ice shelves is critical for predicting any sea level rise. Small ice shelves are likely to react more rapidly than large ones to a change in atmospheric and oceanic temperatures. Therefore, understanding their behaviour is a priority in Antarctic glaciological research.

The behaviour of ice shelves and floating ice tongues is dependent on their boundary conditions. At the ice-ocean interface, these boundary conditions can be appraised by studying the properties of marine ice forming accretions at the base.

In this study, attention is drawn on two case studies, both in the Terra Nova Bay area, Victoria Land.

- A. In the first case, marine ice is formed near the grounding line here defined as the limit between grounded ice and floating ice, either if the glacier goes afloat or becomes again grounded.

Two different types of marine ice have been found. Type 1 is bubble-and debris-free ice with properties which can be explained by intrusion of brackish water in open basal fissures. Closing of the fissures by progression of a freezing front from the sides is precluded and filling by frazil ice is favoured. Type 2 is made of thin clear ice and debris layers which are thought to have formed when a subglacial water-filled sediment enters into contact with sea water and is subjected to freezing under a double diffusion process. It is also stressed that, in a  $\delta D$ - $\delta^{18}O$  diagram, the alignment of marine ice samples on a mixing line does not, necessarily, imply a mixture of continental water and sea water in varying proportions.

- B. In the second case, extensive frazil ice accumulation occurs under the ice shelf. Different frazil ice types can be identified which have different crystallographic, isotopic and chemical characteristics.

Results from oceanic water sampling at various time periods clearly show the occurrence of ice shelf water (ISW) circulation mode 3. In this mode, tidal pumping allows seasonally warm waters of the coastal currents to make contact with the base of the ice shelf and to produce melting. The wide occurrence of orbicular frazil ice accreted at the bottom of the ice shelf is the result of circulation mode 1 i.e. deep thermohaline circulation. Banded frazil ice is probably generated by a double-diffusion process at the limit between ISW-mode 1 and ISW-mode 3, thus partially impeding the net melting loss due to circulation mode 3.

## INTRODUCTION

The stability of the Antarctic Ice Sheet and of sea level is controlled to a large extent by the behaviour of Antarctic ice shelves. Mass balance of ice shelves is dependent, not only on snow accumulation rates or ablation rates at their upper surface or on iceberg calving rates at their front, but also on thermodynamic processes occurring at their base, which control basal melting or marine ice accretion. These thermodynamic processes are determined by the temperature of both ice and sea water near the interface and by the speed of the ocean currents.

Small Antarctic ice shelves or ice tongues, with an ice thickness at their front of approximately one hundred meters or less, are likely to react more rapidly than thicker shelves to a temperature change because their base can be affected by a temperature increase of oceanic waters.

The aim of the present study is to deal with two case studies of small ice shelves which bring into light new factors involved in their behaviour.

## MATERIALS AND METHODS

Shallow ice cores were drilled with a CRREL 3 -in. ice auger from the downglacier part of Hells Gate Ice Shelf, either in continental ice or in marine ice (see dotted surface in figure 1). Ice coring was performed during two field campaigns : twenty-five cores were retrieved in 1989-90 and sixty in 1993-94, all of them being between one and two meters long. Moreover, a 45 m long core was also retrieved close to the front of the ice shelf in 1993-94. The cores were transferred to plastic bags and stored below  $-20^{\circ}\text{C}$  at the Terra Nova Bay station. Cores were maintained at this temperature until they reached the cold room laboratory in Brussels for analysis. The upper few cms of each ice core were discarded in order to avoid surficial effects. Vertical thin sections were made along the total length of each core to observe the different ice textures and to guide further sampling.

After scraping off 0.5 cm of the outside surface of each ice core, a 1 cm thick vertical slice was cut with a clean band saw (tested as not contaminated by the major cations analyzed) along its entire length. Each vertical slice was then subdivided into horizontal pieces at 0.5 cm interval. These were allowed to melt in polyethylene tubes and were analyzed for  $\text{Na}^+$ ,  $\text{K}^+$ ,  $\text{Mg}^{++}$  and  $\text{Ca}^{++}$  with a Varian-SpectrAA 300 atomic absorption spectrophotometer.

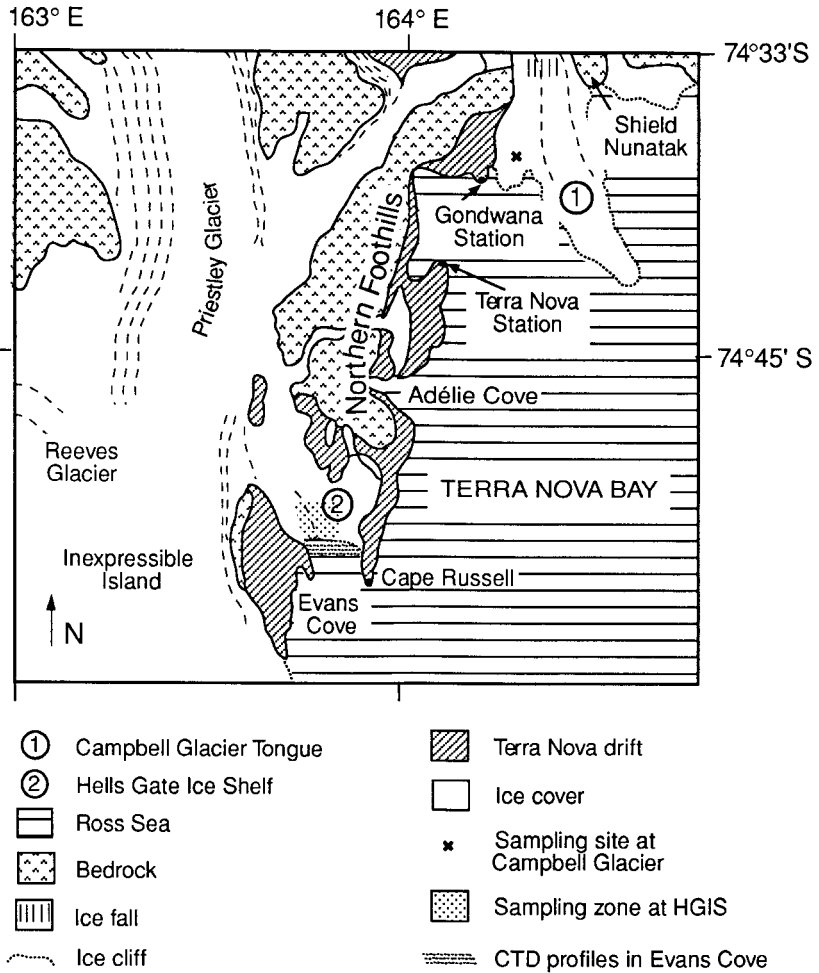


Fig. 1: Location map of the Terra Nova Bay area.

Samples were also taken from the ice cores for co-isotopic analyses of deuterium ( $\delta D$ ) and oxygen-18 ( $\delta^{18}O$ ). The sampling spots were selected after a careful examination of the thin sections between crossed polarizers and on the basis of the concentrations of dissolved solutes obtained by the chemical analyses. The small amounts of ice needed for the mass spectrometer measurements (3 ml) were collected by use of a microtome. Where the  $Na^+$  content of the ice was above

150 ppm, the samples were distilled under vacuum prior to isotopic analysis by a procedure proven to keep the isotopic signal undisturbed. Thirty samples of artificial sea water, produced by adding salt to distilled water of known isotopic composition, were run through the distillation apparatus, and the isotopic composition of the distillate was found to be identical in the limits of the precision of the mass-spectrometer measurements to the initial value. The measurements were performed at the Nuclear Research Center of Saclay (France). HDO and H<sub>2</sub><sup>18</sup>O concentrations are given in  $\delta$  units versus V.S.M.O.W. (Vienna Standard Mean Ocean Water) expressed in per mil. The accuracy of the measurements is  $\pm 0.5\%$  in  $\delta D$  and  $\pm 0.1\%$  in  $\delta^{18}O$ . A similar approach was followed for the Campbell Ice Tongue samples.

Additionally, 30 water samples were collected at the three most central stations near the Hells Gate Ice Shelf front at depths between 0 and 140 meters for oxygen-18 and salinity measurements. The samples were distilled under vacuum prior to isotopic analysis by the procedure already described above.

## **A CASE STUDY OF PROCESSES OCCURRING NEAR A GROUNDING LINE**

### **Generalities**

It is generally assumed that if the melting point is reached at the glacier base in the coastal region, subglacial meltwater loaded with sediments discharges into the sea at the grounding line. Zotikov (1986) has pointed out that if this subglacial meltwater reaches the sea, a layer of relatively fresh water will exist above normal sea water beneath the ice shelf. Since the freezing point of fresh water is higher than the freezing point of sea water, bottom freezing will probably occur and be responsible for a thickening of the ice shelf at or near the grounding line. However, the only drilling made at present of an ice shelf through its entire thickness (J9 on the Ross Ice Shelf) showed no evidence of fresh water in accretion, but rather adfreezing of sea ice (Zotikov et al., 1980). J9 is located along a flow line that connects with an ice stream. Accordingly, any fresh water flowing beneath the ice stream at the grounding line could potentially accrete as freshwater ice to the base of the Ross Ice Shelf. This, in fact, is not observed in the J9 core.

In order to preserve a body of relatively fresh water, the water column must be relatively calm and not influenced by tidal mixing which MacAyeal (1984) thinks

should be efficient near a grounding line. The presence of an inverted topography such as crevasses, domes or channels at the ice-ocean contact (Orheim, 1986 ; Hellmer and Jacobs, 1992 ; Tison et al., 1993) is a way to achieve this sheltering effect.

Marine ice of substantial thickness has been found at the base of some ice shelves (Oerter et al., 1992) and ice tongues (Gow and Epstein, 1972) or at coastal ice margins under an ice cap (Goodwin, 1993). In order to better understand phase changes at the ice shelf-ocean interface, different modes of water circulation have been described and various models of ice shelf-ocean interactions have been proposed in the literature (Jacobs et al., 1979 ; Lewis and Perkin, 1986 ; Jenkins and Doake, 1991 ; Nicholls et al., 1991 ; Hellmer and Jacobs, 1992).

An insight into the problem of determining the conditions necessary for freezing at the ice shelf-ocean interface near a grounding line can be gained by studying the isotopic properties of the marine ice, both in  $\delta D$  and  $\delta^{18}O$ . With this last perspective in mind, a field program was conducted in Campbell Glacier Tongue, a favourable site for such an investigation

Campbell Glacier Tongue is located in Terra Nova Bay area, northern Victoria Land, along the western margin of the Ross Sea.

Campbell Glacier has its accumulation zone in the Transantarctic Mountains; it flows in a NNW-SSE depression carved into the Precambrian and Paleozoic basement rocks (Carmignani et al., 1987). Being deviated by Mount Melbourne which is a Cenozoic volcano, it acquires a more or less north-south direction, and shows a steeper gradient. The presence of small rock outcrops at this level indicates that the base of the glacier is above sea level. Then, Campbell Glacier reaches the sea where it terminates as a protruding glacier tongue (Fig. 1).

The grounding line, usually defined as a line across the glacier where it first goes afloat, is thought to be located just south of the zone with the steeper gradient (Frezzoti, 1993). Radio-echo-sounding fails to detect it. The reflector is characterized by a weak energy contrast. This could be due to a change in the physical characteristics of the ice, the electromagnetic energy being absorbed because of the conductivity of a lower ice unit. Precise radio-echo-sounding is moreover difficult to perform in this crevassed area. Although the precise depth of the grounding line is not known, an approximate value can be given. A bathymetric survey in front of the ice tongue (Angrisano, 1989) gives a depth of about 160 m for the sea bottom. Overdeepening under the Campbell Glacier Tongue is a possibility but the grounding line depth should be around this value. The sampling site is about 3 km downglacier from the presumed position of the grounding line. An



extended definition of the grounding line is considered here. In such a definition, a grounding line is the limit between grounded ice and floating ice, either if the glacier goes afloat or becomes grounded again as for example in the case of a pinning point.

The role of katabatic winds in the Campbell Glacier trough is much reduced. The winds are relatively weak so that the entire glacier is accumulating snow on its surface and, even at the terminus of the floating tongue, a substantial part of the ice cliff is made of ice derived from snow deposited on the tongue. As a result, there is no upward movement of ice and therefore marine ice, if present at the bottom, is not likely to outcrop at the terminus of the floating tongue. However, the south-western part of the ice tongue near Gondwana Station has impinged on bedrock promontories or protuberances. Consequently, basal ice containing debris layers is visible and can be sampled. At the sampling site (Fig. 1), a stacked sequence, a few meters thick, dipping 60° towards the center of the glacier tongue shows two distinctive types of ice interbedded with bubbly glacier ice. A first type located in the upper part of the basal sequence consists of bands of bubble-free ice with a thickness of the order of a few centimeters. The second type, located in the lower part of the basal sequence, shows bands of thin clear ice layers and layers of fine debris sometimes appearing folded with a few occasional pebbles. The proportion of bubbly glacier ice layers is much lower in this case. Debris consists mainly of quartz grains with rounded shapes and smooth edges (60%), volcanic glasses with elongated bubbles (30%) and lithic fragments. A few sponge spicules and shell fragments are also present. The heavy minerals mainly consist of pyroxenes (80%) indicating a major volcanic component and a few olivine, garnet and epidote minerals. The SEM (X-ray energy dispersion probe) analysis of the volcanic glass gives a dispersion in a SiO<sub>2</sub> versus alkali diagram similar to that of rocks from the nearby Shield Nunatak complex (Worner et al., 1989), thus suggesting a local origin.

### **δD-δ<sup>18</sup>O characteristics of basal ice**

An insight into the problem of the formation of these two ice types can be gained by a combined isotopic study of the ice, both in δD and δ<sup>18</sup>O. Indeed, if only a single isotopic ratio is considered, the effects of freezing, isotopic exchange with clay minerals or mixing cannot be distinguished.

Bubbly glacier ice derived from snow of coastal origin and snow fallen in the Terra Nova Bay area have δD values more negative than -130‰ and δ<sup>18</sup>O values

more negative than -17‰. Together with bubbly glacier ice from the continental interior with lower  $\delta$ -values, they are aligned, in a  $\delta D$ - $\delta^{18}O$  diagram, on a precipitation line with the equation  $\delta D = 7.92 \delta^{18}O + 2.76$  ;  $r = 0.997$  ( $n = 41$  samples).

Basal ice with an isotopic composition less negative than -130‰ in  $\delta D$  and -17‰ in  $\delta^{18}O$  cannot be considered as unmodified glacier ice. Basal ice samples have been plotted as open symbols on figure 2. They fit quite well a straight line with equation  $\delta D = 7.86 \delta^{18}O + 0.29$ ;  $r = 0.998$  ( $n = 71$  samples). The large range of isotopic values reaching values close to those obtained by freezing normal sea water and the slope of the line preclude a simple freezing process. Indeed, if equation (1) from Jouzel and Souchez (1982) is used to compute the  $\delta$ -range between 1 % and 99 % freezing of a closed water reservoir, the range obtained is much less than the observed one. For an open reservoir, the range in  $\delta$ -values in the ice would be even smaller. Enrichment by isotopic exchange with clay minerals is able to produce important isotopic shifts but on a much lower slope (Souchez et al., 1990) and is therefore also precluded in this case.

A simulation has been conducted in order to test if this alignment of data of basal ice from the Campbell Glacier Tongue could correspond to a mixing line. The local sea water has been sampled at 30 m depth ; its  $\delta D$  value is -3.23‰ and its  $\delta^{18}O$  value -0.69‰. In the simulation (black symbols in figure 2), this local sea water is mixed in varying proportions with the melt of each glacier ice sample collected in the area. It is assumed that no fractionation occurs during melting of ice. Three mixing ratios have been used : 99% sea water (black squares), 50% sea water (black triangles) and 1% sea water (black dots). The  $\delta$ -values of the ice resulting from freezing of the mixtures have been calculated for deuterium and for oxygen 18, using the equation  $\delta_s = a (1000 + \delta_w) - 1000$  where  $a$  is the equilibrium fractionation coefficient and  $\delta_w$  the  $\delta$  value of the mixed water. The equilibrium fractionation coefficient for deuterium is taken as 1.0208 (Arnason, 1969) and for oxygen 18 as 1.003 (O'Neil, 1968). The points representing these various computations have a distribution which is very close to the points representing the samples of basal ice. Therefore the straight line on which the basal ice samples are aligned can be considered as a mixing line and, consequently, the basal ice samples as marine ice. Let us note here that if a 2‰ higher equilibrium fractionation coefficient for deuterium is considered for sea water, a possibility that might exist (Beck and Munnich, 1988), the fit would be even better.



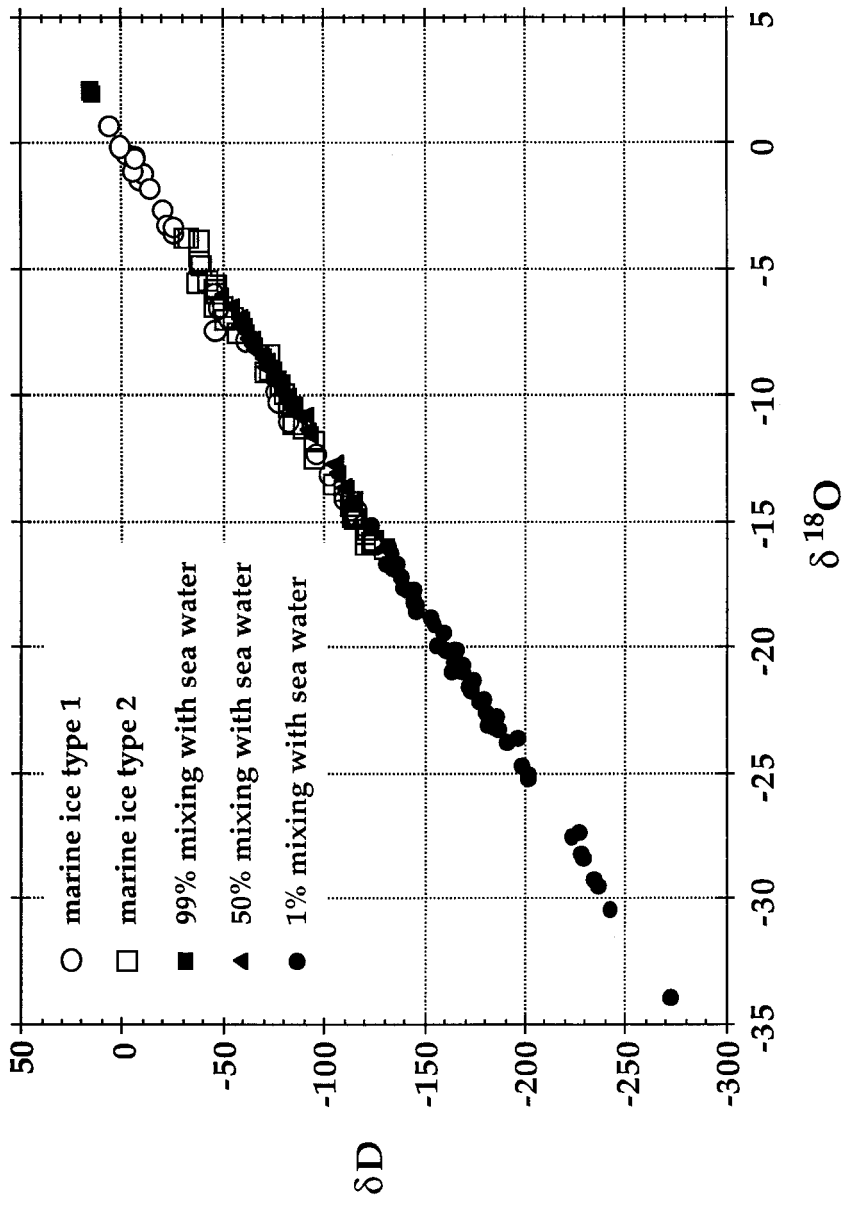


Fig. 2 :  $\delta D$ - $\delta^{18}O$  relationship in basal marine ice from Campbell Glacier Tongue compared to a mixing computer simulation (see text)

As discussed below, the presence of a mixing line does not however necessarily imply a mixture of continental water and sea water in varying proportions beneath the floating glacier.

### **Texture-isotope relationships in the marine ice**

Common features to all marine ice samples in this study can be deduced from a careful examination of figure 3. Clear ice layers always display the less negative  $\delta$ -values and a gradual change to values typical of glacier ice occurs as one proceeds towards the boundaries of these layers. Very often, transitional  $\delta$ -values occur within a single crystal layer which is bubble-free in its inner part and contains bubbles in its outer part (Fig. 3). The crystal size in this layer is similar to the one for unmodified glacier ice.

Major differences however exist between the marine ice in the upper part of the basal sequence (type 1) and that occurring in the lower part (type 2).

In the upper part, the center of the clear ice layers consists of very small crystals (sometimes with a thin line of tiny particles) where the maximum  $\delta D$  values vary between -30‰ and +6‰, thus approaching values observed in frozen sea water (Fig. 3a to c). They form the group of marine ice samples in the upper right corner of figure 2. As developed below, these characteristics can be understood if intrusion of brackish water has taken place in fissures freshly open at the base of the floating glacier, with subsequent ice formation.

The area at the bottom of a floating glacier or ice shelf close to the grounding line is a favourable site for the formation and opening of basal crevasses. Bottom crevasses have been recorded by Orheim (1986) on the Riiser-Larsenisen by radio-echo-sounding. Hellmer and Jacobs (1992) indicate that bottom crevasses are common near grounding lines where tidal bending occurs. They also explain the filling of bottom crevasses with marine ice by an ice pump mechanism driven by the pressure dependence of the freezing point. This ice pump mechanism could readily fill a 200 m-high crevasse with marine ice, a probable reason for the rapid disappearance of bottom crevasses. Jezek and Bentley (1983) believe that most bottom crevasse fields are associated with rapid grounding or ungrounding of ice. The crevasses reported by all these authors have dimensions of meters. The type 1 marine ice inclusions studied in this paper are only centimeters wide. Possibly, these fissures could exist in the same situations but remain undetected by radio-echo-sounding. They might have formed at a larger scale and subsequently subjected to strain thinning.



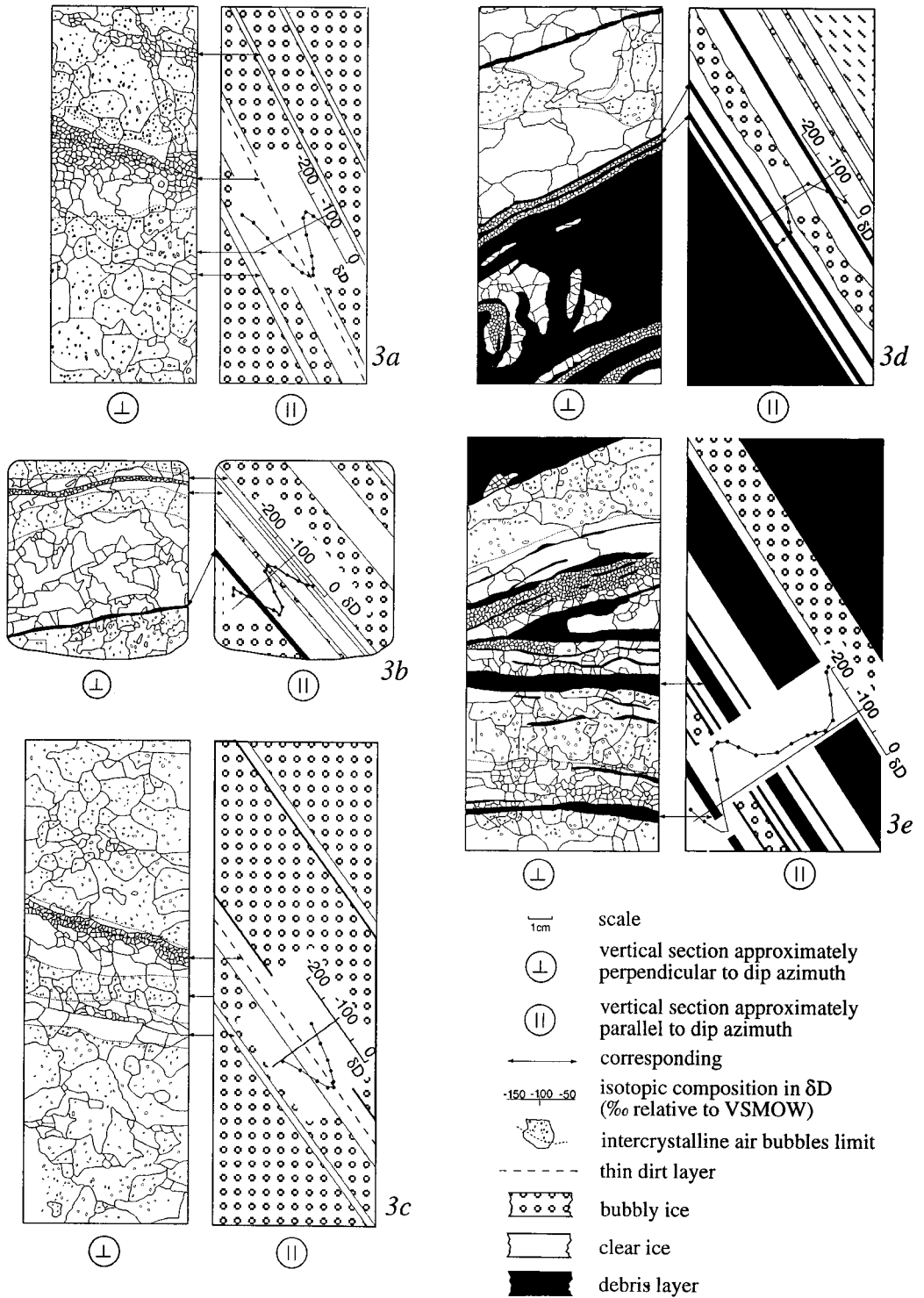


Fig. 3 : Detailed textural properties and  $\delta D$  profiles in selected ice cores from the basal ice of Campbell Glacier Tongue

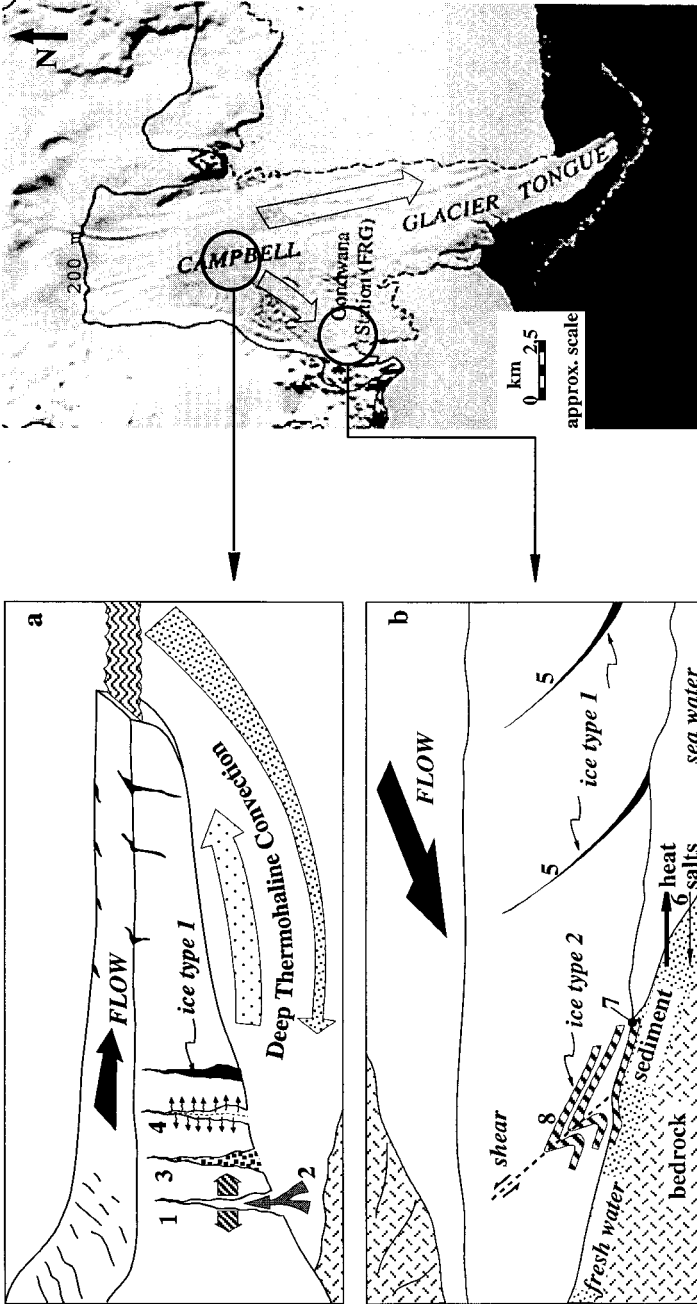
Strain thinning could explain the presence of very small crystals in the center of the fissure as a consequence of grain fracturation. However, the  $\delta$ -values in the center of the fissure are so weakly negative that an overwhelming contribution of sea water is required. If present, the grain fracturation must thus have occurred after the formation of marine ice in the fissure.

This raises the possibility that larger crystals might have originally filled the fissure. Such large crystals could have been congelation ice due to ice growth from the sides of the fissure. Migration of a freezing front from the sides of the fissure towards its center as a consequence of the heat sink provided by the cold ice surrounding the crack must thus be investigated. There is no indication, in the large crystals present in the fissure, of the occurrence of brine layers which are a diagnostic feature for congelation ice. On the other hand, geometric selection of crystals during growth in the liquid phase cannot be detected in the thin sections examined. More important, the isotopic distribution of  $\delta$ -values in the fissure is a strong argument against such a process. Indeed, if a freezing front is progressing into water, the first ice formed -in this case, the ice closest to the sides of the fissure- will have the less negative  $\delta$ -values since the maximum enrichment of heavy isotopes in the ice compared to the initial water is produced there. With the development of freezing, the residual water becomes impoverished in heavy isotopes (Souchez and Jouzel, 1984). The successive frozen layers will thus be more and more negative. Such an isotopic distribution is not present; a reverse distribution is displayed with less negative  $\delta$ -values in the center of the fissure and more negative  $\delta$ -values towards the sides.

Frazil ice formation processes yield other ways to produce ice crystals from brackish water (Weeks and Ackley, 1986). Frazil ice can be produced by turbulence but such a process is not likely to occur here in the confined space of the fissure. Frazil ice can also be produced by a mechanism of double diffusion (heat and salt) involving the existence of two water masses with contrasted temperatures and salinities, both at their pressure melting point. Clearly, this is not possible here. Finally, frazil ice crystals could be formed in adiabatically raising water as a consequence of the pressure dependence of the freezing point. Although we cannot prove that this process is effective here, we consider that the filling of the fissure by frazil ice is the best explanation with the information at hand.

The frazil ice crystals were perhaps originally bigger and their size reduced by grain fracturation. Figure 4a is a sketch illustrating the processes involved. Recrystallization must have occurred as indicated by the presence of ice crystals which are bubble-free in their inner part and bubbly in their outer part at the glacier





**Marine ice type 2**

6. double diffusion process between fresh continental meltwater and sea water through the sediment ...
7. ...initiates freezing
8. shearing resulting from compression on the obstacle where impingement occurs eventually forms folded layers of marine ice

**Marine ice type 1**

1. opening of the fracture when ungrounding
2. filling with brackish water
3. frazil ice formation
4. isotopic diffusion to the sides of the fracture
5. strain thinning further downstream

Fig. 4: Sketches illustrating the processes involved in the formation of type 1 marine ice (a) and type 2 marine ice (b). The scale of the features is enlarged for clarity.

ice - frazil ice contact. Diffusion of isotopes along the pathway represented by water films at the ice crystal limits during recrystallization must certainly be taken into account. It probably explains the gradual decrease in  $\delta$ -values from the center of the fissure towards the sides in this type of marine ice. Clearly, in this case, the alignment of the samples on a mixing line does not reflect the mixing of two water masses.

In the lower part of the basal sequence, the type 2 marine ice with thin clear ice and debris layers (Fig. 3d to e) exhibit a range in  $\delta D$  values of -110‰ to -30‰, indicating a greater influence of continental meltwater. These characteristics can be explained if a water-filled sediment at the glacier-ocean-rock contact is subjected to freezing because of the difference in freezing points between continental meltwater and sea water. In this process, thermal diffusivity being higher than salt diffusion, the water-filled sediment loses heat more rapidly than it gains salt. Moreover, heat can diffuse through both liquid and solid fractions, but salt only through the liquid. The water within the sediment will have an isotopic composition dependent on the variable contribution of continental meltwater versus sea water. This is reflected in the shift in  $\delta$ -values of type 2 marine ice on the mixing line. Diffusion effects must also be considered for the transitional  $\delta$ -values between adjacent layers.

The presence of these thin clear ice layers between the debris layers with such a specific isotopic signature requires basal freezing. If basal freezing is to occur, the sea water must itself be at the freezing point which is not the case for surface waters reaching the bottom of ice shelves (Lewis and Perkin, 1986). This implies melting and the removal of basal ice in other regions. Although we have no measurements of water temperatures and salinities near the grounding line, the complexity of this contact zone in three dimensions makes the process plausible. In the case of type 2 marine ice at Campbell Glacier, it is clear that it forms where the glacier runs aground further downstream at shallower depths. Figure 4b is a sketch showing the processes involved. Mechanical incorporation of the ice and debris layers into the ice shelf is certainly a possibility at this location. An investigation of the marine ice properties, like the one conducted in this study, is able to give some clues to the formation processes but gives no indication of the transfer mechanisms. As shown in figure 3d and 3e, small scale folding can be invoked to explain the multiple-layered structure.

It is not known if the continental meltwater component has been produced at the glacier bed by melting due to geothermal and frictional heat or if it has been able to find its way to the bed from the surface. The geothermal heat flux does not seem to be abnormally high : geothermal anomalies have only been found in the



top part of the Mount Melbourne volcanic edifice but not in the lower Campbell Glacier area (Rossi, 1991).

As the ice was raised to the surface when it impinged on bedrock promontories or protuberances, the possibility that pressure melting and regelation occurred should be discussed. Although it is not possible to prove that this process has not taken place, the type of debris included in the ice makes it unlikely as the initial accretion mechanism. It could have occurred as a post-depositional process. However, it has been shown earlier (Souchez et al., 1988) that pressure melting and regelation does not significantly modify the isotopic properties of the ice submitted to this process.

The presence of shell fragments and sponge spicules in the debris layers raises the possibility that the debris originated from the Terra Nova drift which mantles the eastern flank of the Northern Foothills in the coastal region from Cape Russell in the South to the Campbell Glacier Tongue further North (Orombelli et al., 1990). Shell fragments and worm tubes of mixed ages are common in Terra Nova drift but not sponge spicules. Near Adelie Cove (see Fig. 1), this drift is commonly ice cored and hummocky. The ice cores are made of bubbly glacier ice with  $\delta^{18}\text{O}$  values reaching -35‰ and bands of bubble-free ice reaching  $\delta^{18}\text{O}$  values of +2‰. Such highly different values of  $\delta^{18}\text{O}$  characterize samples collected in a vertical sequence of a few decimeters in the same ice core. The similarity with type 1 marine ice might indicate the presence of a former grounding line at proximity. In this hypothesis, the buried ice could have been partially formed near a fossil grounding line of a late Wisconsin Campbell Glacier advancing onto the Ross sea continental shelf. It is now above sea level because of isostatic rebound. The type 2 marine ice consisting in debris and clear ice layers with its specific isotopic signature has never been found in the ice cores from Terra Nova drift. It is thus quite unlikely that reworking of Terra Nova drift could explain the layered structure of type 2 marine ice at Campbell Glacier Tongue.

With the extended definition of the grounding line in mind, one can thus consider that the two types of marine ice here studied were formed near a grounding line. Type 1 was probably formed closer to the center line of the glacier tongue than type 2. Their superposition (type 1 over type 2) results from impingement on bedrock protuberances. Unfortunately, ice fabrics of the marine ice types do not give additional information on their formation processes. Indeed, on a Schmidt diagram, ice crystal c-axes form a small girdle indicative of horizontal compression against an obstacle. The ice fabrics thus reflect the impingement on bedrock protuberances and no remnant of the original fabric is preserved.

## Conclusion

Two types of marine ice accreted at the base of a floating glacier near its grounding line have thus been distinguished. In both cases, the ice samples are aligned in a  $\delta D$ - $\delta^{18}O$  diagram on a mixing line. Freezing of brackish water in basal open fissures conducive to frazil ice production and consolidation followed by isotopic diffusion along grain boundaries is identified as the most plausible mechanism for formation of type 1 marine ice. Freezing of a water-filled sediment at the ice-ocean-bedrock contact as a consequence of double diffusion effects is considered as the most likely process for formation of type 2 marine ice.

## A CASE STUDY OF ICE SHELF-OCEAN INTERACTION FOR A SMALL ICE SHELF

### Generalities

This case study is conducted on the Hells Gate Ice Shelf (HGIS) reaching the sea in Terra Nova Bay near Cape Russell (Fig. 1). This ice shelf extends from north to south for 16.6 km with a maximum width of 9.8 km. It is composed of three main sectors (western, central, eastern) separated by two medial moraines stretching from north to south. Echo sounding profiles, performed about 1.5 km inland from the ice front, show a maximum ice shelf thickness between 60 and 70 m (Souchez et al., 1991). Further upstream, the ice shelf quickly thickens to about 160-180 meters (Tobacco, personal communication). Large scale morphological patterns, marine ice outcropping patterns and ice foliation patterns suggest a complex dynamical behaviour where several individual ice flows of variable thicknesses meet together, and side effects considerably affect the flow patterns in some areas (Tison et al., in press). The moraines separating the different sectors contain rock fragments, shells and worm tubes. As pointed out by Baroni (1988), the debris was incorporated into the ice by bottom freezing of sea water around Vegetation Island, north of Inexpressible Island. This small rock outcrop acts as a pinning point of the ice shelf and is situated near its upstream boundary. Baroni (1988) gave an uncalibrated  $^{14}C$  age of  $2495 \pm 160$  years BP (GX - 14084) for the older shells reaching the surface of HGIS. This allowed him to propose an ablation rate of about  $10 \text{ cm y}^{-1}$  due to very strong and frequent katabatic winds blowing from the polar plateau. As

a result of this ablation, marine ice progressively replaces glacier ice downstream of Vegetation Island as confirmed by a  $\delta^{18}\text{O}$  shift from strongly negative to positive values (Baroni et al., 1991 ; Souchez et al., 1991).

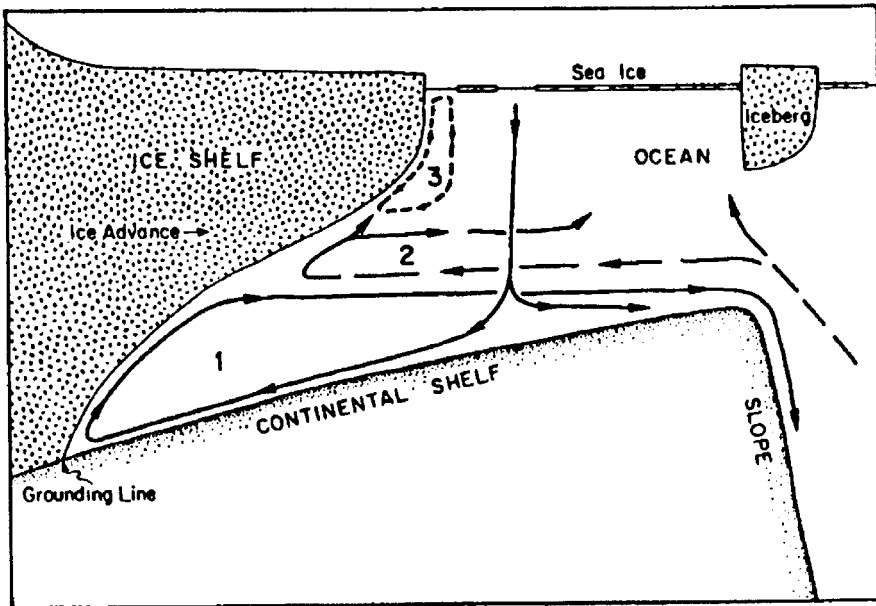


Fig. 5 : Sketch showing the three main circulation modes at the base of an ice shelf.

It should be noted that, in this figure, lateral components of the water movements are not taken into account.

In a recent attempt to estimate the impact of melting of ice shelves on the mass balance of Antarctica, Jacobs et al. (1992) clearly summarized the three different modes through which ocean circulation affects sub-ice-shelf melting (Fig. 5). In mode 1, deep thermohaline convection occurs in the large sub-ice-shelf cavities where High Salinity Shelf Water (HSSW) melts the inland base of the ice shelf to form the very cold but relatively fresh Ice Shelf Water (ISW). This mode is believed to be responsible for both melting and freezing processes (marine ice formation) beneath large parts of the major antarctic ice shelves (Filcher-Ronne, Ross and Amery ice shelves). Circulation mode 2 provides melting through inflows of "warm" intermediate-depth waters from the slope-front region. Inflow can either fill most of the sub-ice cavity -and therefore sustain important melting- (Potter and Paren, 1985) or be restricted in area, and even have much of its heat recirculated to

the open sea (Jacobs, 1991). Finally, circulation mode 3 associated with relatively shallow ice shelf bases and walls within 100 km of the ice front, leads to high melting rates due to tidal pumping and to the seasonally warmer water of the coastal currents (Jacobs et al., 1985). Jacobs et al. (1992 - Table I) reckoned that the net melt from ice shelf bases in the Antarctic reaches  $544 \text{ Gt year}^{-1}$ , an amount only slightly lower than ice shelf surface accumulation ( $616 \text{ Gt year}^{-1}$ ). The share of areas located within 100 km of the ice front and of ice shelf walls is estimated at  $192 \text{ Gt year}^{-1}$ , i.e. about 35% of the total net loss. In their calculations, Jacobs et al. (1992) have taken into account that part of the melting from circulation mode 1 is balanced by marine ice accretion due to cooling of ISW plumes to the in-situ freezing point. Models estimates were provided by Hellmer and Olbers (1989, 1991) and Jenkins and Doakes (1991), and are constantly in the process of refinement (Jenkins and Bombosch, 1995 ; Bombosch and Jenkins, 1995).

### **Characteristics of Ross Sea Waters in the Terra Nova Bay area**

The physical and chemical characteristics of Ross Sea Water, particularly in the Terra Nova Bay area, have been extensively studied during several oceanological cruises, and have given a better perception of the general circulation patterns [see, for example, Jacobs et al. (1970-1985), Stocchino and Lusetti (1990), Boldrin and Stocchino (1990), Stocchino and Manzella (1991), Fabiano et al. (1991), Dini and Stenni (1995)].

The surficial circulation in the Ross Sea consists of a cyclonic gyre (Klepikov and Grigor'yev, 1966) flowing northward along the Victoria Land coast. The deep circulation is controlled by the relatively warm Circumpolar Deep Water (CDW) which flows southward on the continental shelf, interacting with the Ross Ice Shelf barrier. This movement helps in confining the High Salinity Shelf Water (HSSW), formed in the Western Ross Sea, in the inverted depressions of the Shelf and, particularly, in those of Terra Nova Bay.

The most important feature of Terra Nova Bay is probably the perennial polynyas. Their existence is tentatively linked to the combined action of the katabatic winds, which shift eastward the newly formed sea ice, and of the Drygalsky Ice Tongue which is sheltering the area from the northward drifting of Ross Sea pack ice (Bromwich and Kurtz, 1984). The presence of the polynyas could be responsible for the upwelling of warmer and saltier waters detected by Stocchino and Manzella (1991) during the summer, especially in the coastal areas.

The structure of the water column away from the front of ice shelves and ice tongues is generally simple (Boldrin and Stocchino, 1990 ; Stocchino and Manzella, 1991 ; Dini and Stenni, 1995) : a surface layer about 50 meters thick, ascribed to Antarctic Surface Water (AASW) rests on a saltier and colder layer of High Salinity Shelf Water (HSSW) extending down to the Shelf floor. The AASW shows variable physical and chemical characteristics owing to the different processes ongoing: mainly surface freezing and interactions with meltwater from continental and sea ice. Nevertheless, this water mass has generally relatively high temperature values (around 0°C, with maxima reaching 2°C - Boldrin and Stocchino, 1990) and is delimited downward by a sharp thermocline (Stocchino and Manzella, 1991).

### **Sea Water Characteristics in Front of Hell's Gate Ice Shelf**

Figure 6 plots  $\delta^{18}\text{O}$  against salinity for the water samples from three stations near HGIS front [40 (●), A4 (▲) and B4 (⊕)], and compare them to selected data sets from the literature for the Southern Ocean. Figure 7 shows  $\delta^{18}\text{O}$  individual profiles compared to temperature and density profiles. All waters, including surface waters that might reflect mixing of ocean water with melted continental ice or with snow blown by katabatic winds, show salinities in accordance with ice shelf waters, but their isotopic signature is quite original, even occasionally reaching positive values. The only possible way of producing these signatures is by mixing ocean water with the melt of marine ice (+1.64 to +3.26 ‰ in  $\delta^{18}\text{O}$  - Tison et al., 1993). As seen in the individual profiles of figure 7, the more positive values occur below AASW, therefore precluding significant inputs of marine ice meltwater coming from the surface of HGIS. The wedge of lighter water must be associated with a process of melting of marine ice at the ice shelf-ocean interface, some distance inland from the front.

CTD profiles showing basal melting effects from tidal pumping of warm summer surface waters (AASW) under the Ekström Ice Shelf (Southeastern Weddell Sea) have recently been described by Fahrback et al. (1994). Repeated CTD profiles during a 12 hours period about 8 km inshore from the edge of the ice shelf reveal a three-layered water column under the 200 meters thick ice shelf. The top 10-20 meters layer, in contact with the base of the ice-shelf, shows continuous increase of temperature and salinity, and is seen as the result of active melting at the base of the ice shelf. The intermediate layer about 50 m thick shows a temperature maximum while salinity steadily increases with depth. Depth of the

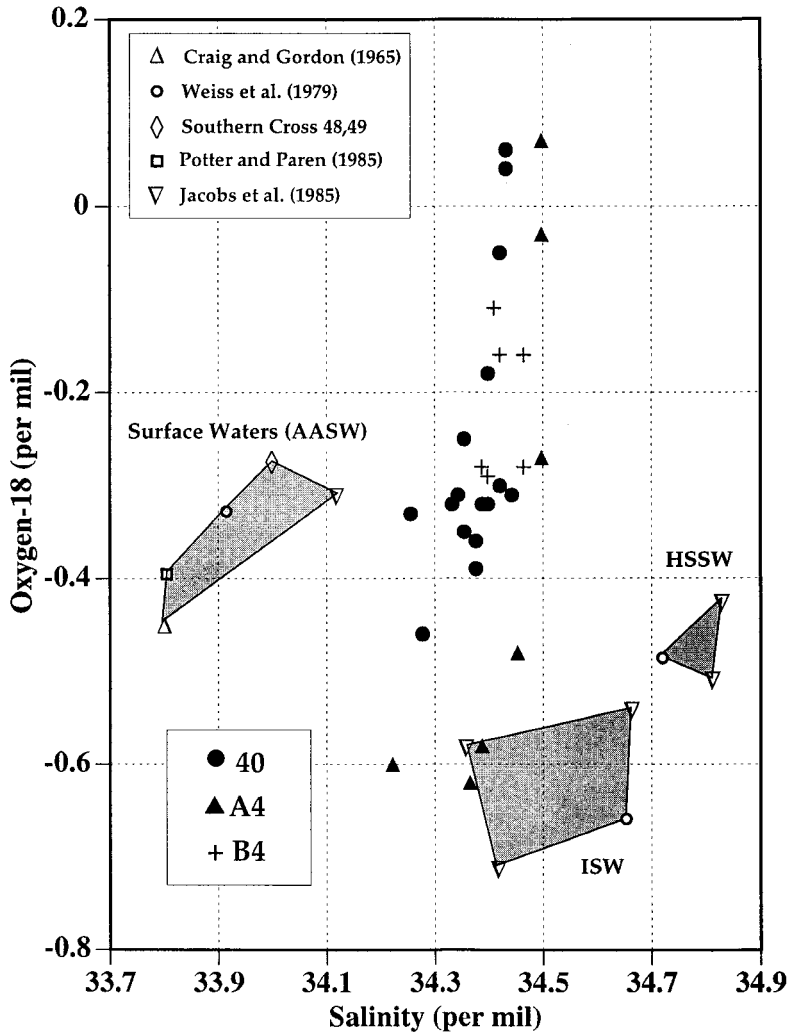


Fig. 6 :  $\delta^{18}\text{O}$  (‰) against salinity (‰) from stations 40 (●), A4 (▲) and B4 (+), compared to selected data sets from the literature for the southern ocean. Data from Southern Cross stations 48 (68°00'S, 170°07'W) and 49 (69°29'S, 169°57'W) are converted from deuterium measurements using the relationship  $\delta\text{D} = 8.3 \delta^{18}\text{O} - 0.8$  (Weiss et al., 1979)

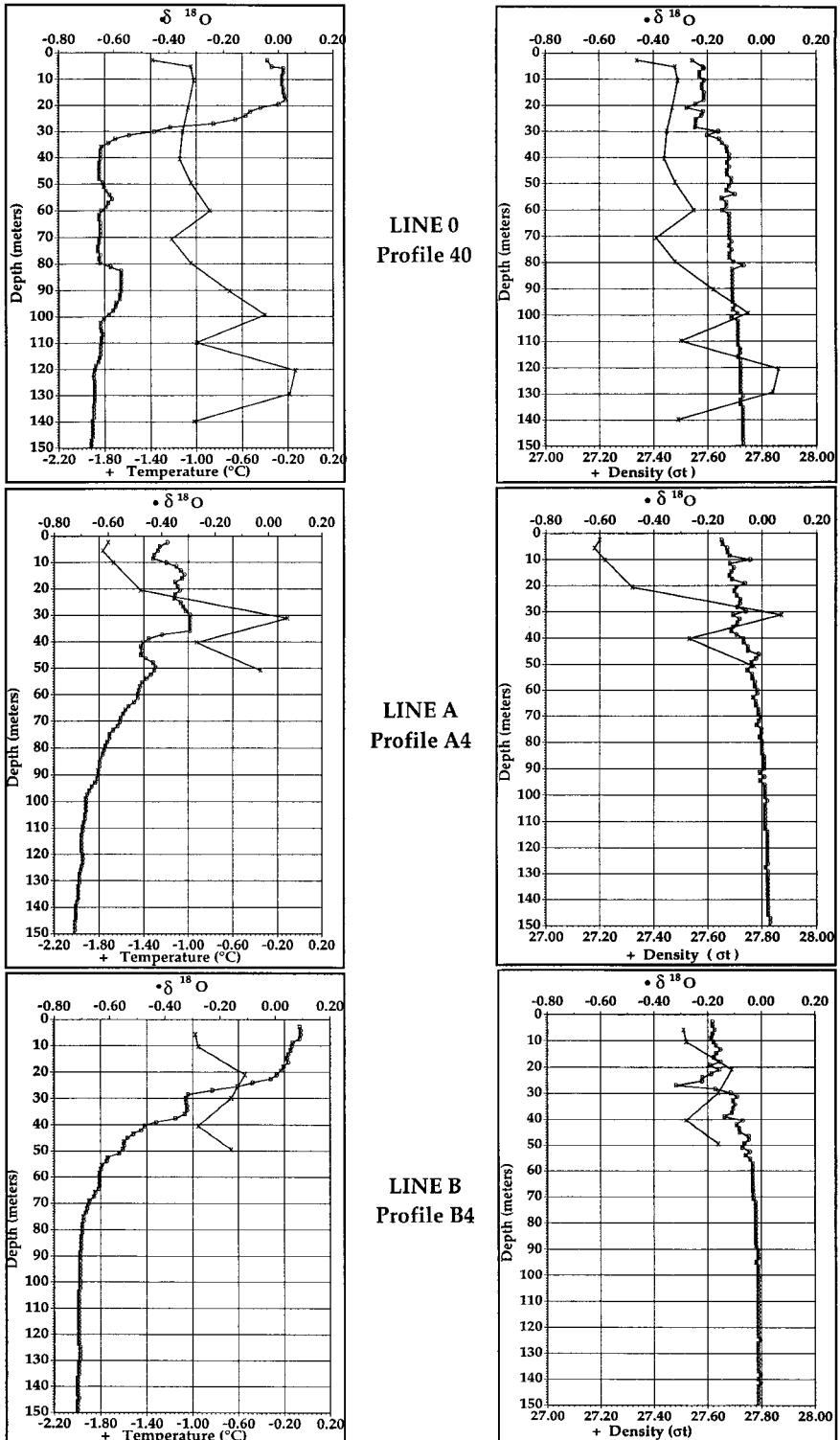


Fig. 7:  $\delta^{18}\text{O}$  (‰) profiles for stations 40, A4 and B4, compared to temperature (left) and density (right) profiles

maximum temperature changes significantly during the tidal cycle. This layer is thought to originate from surface water of the open ocean, and to be responsible for an important part of the melting at the base of the ice shelf. The lower layer, where temperature steadily increases again and also salinity (but with a lower gradient), is shown to result from Warm Deep Water intrusion. The two upper layers described above could be considered as analogs to the ISW-mode 3, successive temperature maxima corresponding to the piling up of ISW-mode 3 inputs from different sources under the ice shelf.

### **Marine ice characteristics**

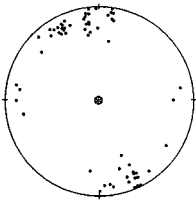
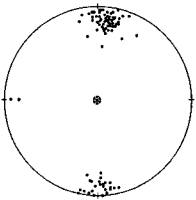
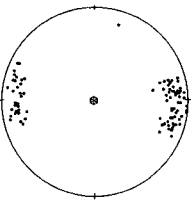
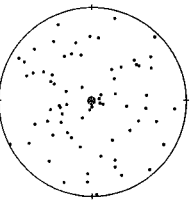
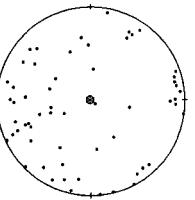
Table I summarizes the overall characteristics of the various marine ice types from HGIS. Most of the data used for making Table I are listed in Ronveaux (1992). Continental ice from inland and fast sea ice from the front of the ice shelf are also briefly described for comparison. All marine ice samples from the ice cores fall into four major textural categories : columnar ice, platelet ice, orbicular granular ice and banded granular ice.

Columnar ice (a texture typical of congelation ice formed by the progression of a freezing front in a liquid water reservoir) and platelet ice are easily recognized by distinctive differences in their textural characteristics (Weeks & Ackley, 1986 ; Lange, 1988). They are a minor component of the Hells Gate Ice Shelf's environment. These two ice types, as underlined by Souchez et al. (1991), are intimately associated and spatially located at the boundary of the continental glacier ice. The same authors presented the isotopic values of marine ice from HGIS on a  $\delta D/\delta^{18}O$  diagram (their Fig. 2) where congelation ice is situated in an intermediate position between sea water samples from the front of the ice-shelf (20-200 m depth) and frazil ice samples. Platelet ice does not differ significantly from the other frazil ice types in this environment. This is illustrated by the isotopic ranges given in Table I. Both ice types show mean salinity values just below 1.5‰, comparable to the lower values observed at the base of a first-year sea ice cover in Breid Bay (Tison and Haren, 1989) and slightly lower than the minimum values (Gow et al., 1987) in the Weddell Sea ice floes. Low salinity values are to be expected when marine congelation ice forms under a thick continental ice cover at very slow freezing rates, and with a maximum salt rejection by the growing ice. The three last lines of Table I give the value of the K/Mg ratio (K and Mg being expressed in  $\text{meq l}^{-1}$  for charge and weight compatibility). This ratio has been chosen since it is unlikely to be affected by salt precipitation in the HGIS



ICE TYPES	GLACIER ICE	FAST ICE		MARINE ICE	
		CONGE- LATION ●	FRAZIL ○	CONGELATION ▲	PLATELET △
<b>CORE # (Fig. 1)</b>	5,12,13,21,22,6 Top	7,9	7,9	6-Middle	6-Bottom
<b>CRYSTAL SIZE</b>	1-2 cm	l = 2-3 cm w = 0.5-1cm	0.2-0.5 cm	l = 4-5 cm w = 1.5-2 cm	l = 2-4 cm w = 0.5-1 cm
<b>ICE FABRIC</b> (vertical plane)	1 strong maximum near the shear zone (core 5) to small girdle or weaker maximum away from the shear zone (12, 21, 22)	—	—	—	—
<b>INCLUSIONS</b> Bubbles	YES : mainly spherical (0.5 mm in diameter), sometimes tubular according to flow. Intracrystalline and at grain boundaries.	YES : associated with brines inclusions	YES	YES : associated with brines inclusions	YES : few spherical
<b>INCLUSIONS</b> Particulate matter	NO	NO	NO	NO	NO
<b>ISOTOPES</b> # samples	8	3	1	4	3
$\delta D$ (‰)	max - 150.9 min - 245.0	11.6 11.0	10.5	16.0 9.8	23.3 16.1
$\delta^{18}O$ (‰)	max - 19.76 min - 31.71	1.74 1.14	1.45	2.02 1.14	2.51 2.08
<b># samples</b> <b>mean salinity (‰)</b>	—	11 1.33	19 1.19	27 1.35	31 1.42
<b>Na</b> (ppm)	max — min — mean —	508.50 273.50 407.99	523.00 202.10 366.69	589.50 197.60 415.94	618.00 281.10 435.43
<b>K</b> (ppm)	max — min — mean —	17.32 8.78 12.91	14.72 8.41 11.63	24.08 6.77 17.95	24.23 10.38 17.29
<b>Ca</b> (ppm)	max — min — mean —	15.95 6.74 11.24	16.29 6.02 11.38	21.76 8.15 17.09	20.41 3.89 15.98
<b>Mg</b> (ppm)	max — min — mean —	52.10 25.55 37.85	45.65 22.60 34.32	70.80 18.60 51.32	81.05 27.70 48.60
$\Sigma 4$ (meq l <sup>-1</sup> )	max — min — mean —	27.64 14.56 21.75	27.41 11.66 19.64	30.77 14.87 26.16	31.71 22.37 25.22
<b>K/Mg</b>	max — min — mean —	0.109 0.102 0.106	0.116 0.100 0.106	0.130 0.099 0.110	0.111 0.089 0.099

Table I : Textural, ice fabric, isotopic and chemical characteristics of the different ice types studied. The symbols representing the different ice types in the top row of the figure are also used in figure 8.

MARINE ICE				
■ FRAZIL BANDED RECTANGULAR	□ FRAZIL BANDED WAVE-LIKE	● FRAZIL ORBICULAR FINE	○ FRAZIL ORBICULAR MEDIUM	○ FRAZIL ORBICULAR COARSE
Part of : 2,3,24,25	Part of : 1,2,3,16,17,25	4 + Part of : 24	18 + Part of : 24	23 + Part of : 1,2,3,16,17,24,25
l = 0.2-0.4 cm w = 0.05-0.2 cm	l = 0.1-0.4 cm w = 0.05-0.1 cm	0.1-0.2 cm	0.2-0.7 cm	0.7-2 cm
				
CORE 2	CORE 24	CORE 4	CORE 18	CORE 23
NO	YES : few	NO	NO	NO
NO	NO	YES FOR CORE 4 : - sponge tests - echinoderm spicules - crustaceous faeces showing peritrophic membrane	YES FOR CORE 18 : cfr core 4 + worm tubes fragments	NO
<b>23</b>	<b>25</b>	<b>13</b>	<b>10</b>	<b>7</b>
19.9	22.1	24.5	21.9	24.3
16.7	15.0	16.0	15.5	15.7
2.76	3.02	3.26	3.19	2.92
1.86	1.64	1.82	1.90	2.12
<b>176</b>	<b>173</b>	<b>95</b>	<b>136</b>	<b>163</b>
0.19	0.36	0.03	0.03	0.14
235.80	801.00	35.42	52.85	229.50
7.34	17.50	5.35	2.76	1.74
57.13	109.79	10.69	8.81	41.65
9.33	26.64	1.20	3.61	5.39
0.17	0.60	0.17	0.05	0.10
2.24	3.85	0.34	0.34	1.60
4.34	21.21	1.50	2.48	6.77
0.15	0.58	0.06	0.01	0.01
1.70	2.66	0.51	0.41	1.41
19.52	72.10	4.38	8.68	15.84
0.24	1.07	0.27	0.03	0.03
6.29	10.79	0.86	0.74	4.93
9.68	36.35	1.80	3.22	11.19
0.36	0.91	0.11	0.13	0.09
2.79	4.20	0.54	0.49	2.36
0.289	0.256	0.259	0.628	1.287
0.056	0.046	0.063	0.064	0.058
0.119	0.114	0.162	0.316	0.324

environment. Indeed, Richardson (1976), in his study of the phase relations in sea ice as a function of temperature, indicates that  $\text{CaCO}_3 \cdot 6\text{H}_2\text{O}$  is the first salt to precipitate from sea water at a temperature close to the freezing point and that  $\text{Na}_2\text{SO}_4 \cdot 10\text{H}_2\text{O}$  and  $\text{CaSO}_4 \cdot 2\text{H}_2\text{O}$  soon follow, at temperatures of  $-8^\circ\text{C}$  and  $-10^\circ\text{C}$  respectively. Marine ice subjected to such a range of temperatures, as is probably the case for the HGIS when it is progressively brought up to the surface by ablation, is likely to show a greater variability in the ratios of elements forming salts under freezing conditions. Following Richardson (1976), concentrations in K and Mg ions in sea water at sub-freezing temperatures, under quasi equilibrium conditions, do not change until the temperature falls to  $-34^\circ\text{C}$ . This is confirmed by the observations of Cragin et al. (1986) in brine layers infiltrating the Mc Murdo ice shelf and progressively submitted to lower temperatures. However, Meese (1989, 1990) showed from dilution curves for sea ice from Southern Beaufort Sea that Mg is slightly enriched (1-2%) with regards to sea water and K slightly depleted (1-2%). These slight fluctuations, attributed to precipitation of Mg and to differential mobility (with regard to Cl) of K, will possibly explain a slight decrease in the K/Mg ratio. This ratio in congelation ice (0.110) and platelet ice (0.099) from HGIS is close to the one in standard sea water (0.096), thereby confirming the absence of significant fractionation with regards to sea water for these ice types. This is also the case for the congelation (0.106) and frazil ice (0.106) in fast ice formed in front of the ice shelf.

The contrast between orbicular and banded granular ice (Table I) is based on textural characteristics following the terminology proposed respectively by Lange (1990) and Gow et al. (1987). According to previous studies (Weeks and Ackley, 1986 ; Gow et al., 1987) a granular ice texture may either result from the transformation of the snow cover at the sea-ice surface, or from the accretion of loose ice crystals initially formed in the water column by various processes and subsequently floating up to aggregate at the ocean-atmosphere interface or under a pre-existing ice-water interface. Since the first genetic process is precluded, for obvious reasons in the case of marine ice, the genetic term of frazil ice will be used in the following text for the granular ice at HGIS. Orbicular frazil consists of crystals, roughly isometric and convex, with rounded grain boundaries. It occurs in three major size classes at HGIS (fine = 0.1 to 0.2 cm, medium = 0.2 to 0.7 cm and coarse = 0.7 to 2 cm). Banded frazil shows small rectangular crystals 0.2 - 0.4 cm in length and 0.05 - 0.2 cm in width, more or less aligned parallel to the local ice-water interface. Under crossed polarizers, some samples display a "wave-like" texture underlined by areas of uniform colors indicating a strong c-axes

concentration in a single maximum. Occasionally, the crystals are arranged in a vortex fashion. Generally, the textural contrast between orbicular and banded frazil ice is reinforced by the ice-fabric, the dirt content, and the major ions chemistry. Banded frazil shows strong c-axes concentrations while, in orbicular frazil, c-axes are random. Particulate matter, mainly organic, only occurs in the orbicular frazil, and the mean chemical content in major cations of this ice type is lower than for the banded frazil. Finally, while the K/Mg ratio in both the banded and the orbicular frazil show evidence of chemical sorting effects, these obviously are stronger in the latter ice type.

### **Evidence for dilution at the ice-ocean interface**

In interpreting the chemical and isotopic results from frazil ice, one must keep in mind that they are in fact the integration of a sequence of three processes :

- 1) formation of individual ice crystals in the water column under favorable temperature/salinity conditions
- 2) accretion of loose frazil crystals at the base of the ice shelf
- 3) consolidation of the accreted loose frazil to form a solid body of ice, under a temperature gradient.

During these three processes, the isotopic and chemical signals will be more or less affected, depending on variables such as characteristics of the parent water for the individual frazil ice crystals, the growth rate of the individual crystals, the characteristics of the host waters where the ice crystals accrete, the porosity of the loose frazil (porosity is used here in the meaning of White (1991), i.e., the % of water present in a volume of saturated frazil ice), the freezing rate of the accreted loose frazil and the possible post-or syn-genetic desalination. Uncertainties on the values of these parameters make it difficult to infer the characteristics of the parent and host waters from the observed chemical and isotopic signals of the consolidated frazil ice. However, hypotheses can be suggested on some of these parameters :

- Desalination processes of sea ice has been extensively described by several authors (Weeks and Ackley, 1986 ; Cox and Weeks, 1986 ; Cox and Weeks, 1988). Formulations have been proposed to estimate desalination rates through either of the three major mechanisms involved: brine pockets migration, brine expulsion and brine drainage. Since these equations require the knowledge of parameters such as the temperature profile along the ice shelf thickness or the brine volume and salinity in the marine ice, the

quantification of similar processes was not possible at HGIS. However, such an attempt has recently been made for the marine ice observed at the base of the Filchner-Ronne Ice Shelf where these data were available (Eicken, personal communication), and it is shown by these authors that the calculated desalination rates are several orders of magnitude too low to explain the salinity values of the marine ice they observed. Although the Filchner-Ronne Ice Shelf is considerably thicker than HGIS at the B13 sampling site (239 m - Oerter et al., 1992), these results seem to indicate that the active desalination processes described in sea ice must be of minor importance for marine ice several tens of meters thick. Furthermore, the tight packing of the ice crystals in frazil ice from HGIS and the lack of any visible gaseous or liquid inclusions (brine layers, brine pockets) or of cracking disruption, do not support the existence of an efficient process of brine pocket migration or brine expulsion. A process similar to brine drainage must however probably occur during the consolidation phase of the accreted loose frazil. The rejection of salts as frazil consolidates in the upper layers will produce denser interstitial waters, possibly initiating a convective process that will bring the low salinity water from the basal layers (where it originates, as discussed below) to the interior parts where the ice growth takes place.

- A narrow range of values for the porosity of a loose frazil ice mixture at or near the water surface can be obtained from various sources. Laboratory investigations on freshwater frazil ice (White, 1991), where porosities were calculated from the measured weight of a known volume of saturated frazil ice for twenty samples, measuring  $0.3 \text{ dm}^3$ , gave average values of  $67 \pm 13\%$ . Similar measurements in natural frazil ice ranged between 43% and 48% and were close to those deduced from borehole dilution tests ( $43.6 \pm 3.2\%$  - White, 1991). Salinity can also be used as an indirect method to determine frazil ice porosity. For the simple experiments described in the next section, individual dry distilled ice crystals of various sizes were poured into an experimental reservoir of natural sea water until saturation was achieved. Since the individual ice crystals can be considered as pure ice, the ratio between the salinity of the sea water and the salinity of the mixture provides an estimate of the porosity of the latter. Porosity values between 43% (fine submillimetre sized crystals) and 52% (coarse centimetre sized crystals) were obtained. A similar approach can be used with natural samples : freshly formed pancake ice from the Weddell sea studied by Eicken and Lange (1989) show maximum salinities of about 15‰ which, if compared to a normal sea

water salinity of 34.8‰, gives a minimum porosity of 43.1%. However, some buoyancy pressure related effect should be considered in the case of frazil occurring under the ice shelf at some depth, the upper layers being mechanically "squeezed" by the deviatoric stress exerted by the lower layers. Since this effect is difficult to quantify, especially if the total thickness of frazil ice accreted is not known, a value of 40% porosity will be considered in this case, bearing in mind that this value might eventually be overestimated.

- The freezing rate of the accreted loose frazil must be quite similar to that of congelation ice formed under comparable ice shelf thicknesses. Since it is very slow, isotopic and chemical fractionation in the freezing host water must occur very close to equilibrium. The equilibrium fractionation coefficients for  $\delta D$  and  $\delta^{18}O$  are well documented, and usually taken as  $\alpha = 1.0208$  and  $\beta = 1.003$  respectively, although the possibility of a 2‰ higher  $\alpha$  value might exist for platelet ice formed in high salinity sea water (Beck and Munnich, 1988). Values for the effective chemical distribution coefficient ( $k_{eff} = \text{concentration in the ice} / \text{concentration in the liquid away from the interface}$ ) are found in the Antarctic literature on sea ice (Gow et al., 1987 ; Souchez et al., 1988 ; Lange, 1988, for example). The lowest one ( $k_{eff} = 0.04$ ) was observed (Souchez et al., 1988) in congelation ice at the bottom of a first year sea ice cover in Breid Bay (Princess Ragnhild Coast ) and can thus be considered as the closest value to the thermodynamic equilibrium coefficient. Using the mean salinity of our congelation ice at the base of HGIS ( $S_i = 1.35\%$ ), an effective distribution coefficient of 0.04 can be calculated. However, as discussed below, it should be noted that these values of  $k$  are only valid for congelation ice formed in undiluted sea water ; as indicated by Gross (1968), the value of  $k_0$  (equilibrium distribution coefficient) can indeed differ strongly from dilute solution to sea water due to different interface morphologies.
- The freezing rate of individual frazil ice crystals is much more difficult to estimate. Indeed, the validity of isotopic equilibrium fractionation for stable isotopes of oxygen and hydrogen is probably strongly dependent on the degree of supercooling. To our knowledge, no experimental or field data are available on this subject for frazil formed by double diffusion or supercooling due to adiabatic upward movement of sea water. However, the situation is different for the major cations since individual crystals growing from a liquid reservoir are believed to be made of pure ice, impurities being concentrated at grain boundaries. Thus, one may consider that the chemical signal in the

resulting unconsolidated frazil ice is independent of the chemical characteristics of the parent water in which the individual crystals originate, and exclusively reflects the characteristics of the host water where the crystals accrete.

Using a porosity of 40%, an equilibrium chemical distribution coefficient ( $k_0$ ) of 0.04, and the observed frazil ice salinities of Hells Gate (Table II), it is possible to reconstruct the salinity of the host water by studying the salinity of the different frazil ice types [ $S_{\text{host water}} = S_{\text{frazil ice}} / (k_{\text{eff}} \times \text{porosity})$ ]. This salinity increases from 1.9‰ for the host water derived from the mean salinity of fine and medium orbicular frazil ice to 8.8‰ for the coarse orbicular, 12‰ for the banded rectangular and 22.5‰ for the banded wave-like frazil. Such salinities have never been observed in large scale oceanographic salinity measurements below or in front of ice-shelves in the Terra Nova Bay (Boldrin and Stocchino, 1990).

Table II : Reconstructed salinities for the "host water" of the different types of frazil.

Type of frazil	Orbicular Fine	Orbicular Medium	Orbicular Coarse	Banded rectangular	Banded Wave-like
Mean salinity (‰)	0.03	0.03	0.14	0.19	0.36
Host water salinity (‰) with $k_0=0.04$ and porosity=40%	1.9	1.9	8.8	12.0	22.5

Thermodynamic considerations suggest that the salinity values for the interstitial water in the loose orbicular frazil are underestimated. Indeed, if, following Doake (1976), we consider the phase diagram relating temperature to salt concentration of a system consisting of salt, water and ice, and if we also consider that the system is allowed to reach equilibrium, a salinity of 1.9‰ for the solution in contact with the ice is only possible for water temperatures of the order of  $-0.1^\circ\text{C}$ . As indicated before, the maximum water temperatures observed in front of the ice shelf, at depths compatible with its base, are  $-0.5^\circ\text{C}$ . In the phase diagram, such a temperature value corresponds to a salinity of about 9‰ on the liquidus. Reducing drastically the porosity of the loose frazil to half its value, to emphasize the potential squeezing effect at depth, would still underestimate by 50% the minimum possible salinity for the host water of the fine and medium grained orbicular frazil. On the other hand, to obtain a salinity of 9‰ for this host water, using a porosity of 40%,

one must use a  $k_0$  value of 0.008 in the calculations above. This lower value of  $k_0$  is comparable to the one obtained by Gross et al. (1977) in experiments to determine solute distribution at the ice-water phase boundary. Indeed, a  $k_{\text{eff}}$  of 0.004 was observed in a monosaline solution of NaCl with a concentration of about 10‰ (1.8  $10^{-1}$  M). The underestimation of the host water salinity for the orbicular frazil is thus most probably due to the combination of two factors: a possible lower porosity due to frazil ice compaction (at least in its higher levels) and the dependency of the  $k_0$  value on the global salinity of the freezing solution. Chemical sorting effects, that cannot be explained by simple mechanical means, favour the latter process, as discussed in the next section.

The scientific rationale used to determine the host water properties from the chemical signal cannot be followed using the isotopic characteristics of frazil ice since, with a porosity of 40%, the observed values will be a combination of fractionation processes both during the genesis of individual crystal (poorly known) and during the consolidation of the loose matrix. A considerable amount of frazil samples show isotopic values which are higher than the one obtained by applying the maximum possible fractionation shift of 3‰ in  $\delta^{18}\text{O}$  to the local parent sea water value of -0.6‰. Indeed, as seen in Table I, the maximum values in  $\delta^{18}\text{O}$  for all frazil ice types are higher than 2.4‰. This implies that, at least for the samples showing values higher than 2.4‰, dilution by marine ice meltwater, with an isotopic signal more positive than normal sea water, has occurred. Moreover, even for the samples with a  $\delta^{18}\text{O}$  lower than 2.4‰, dilution by meltwater from marine ice must be the most frequent case. The large dilution factors of sea water by meltwater, deduced from the salinity data discussed above, preclude glacier ice as a source since the very negative  $\delta^{18}\text{O}$  values of the latter would result in much lower  $\delta^{18}\text{O}$  values in frazil ice than those observed (see Table I).

### **Behaviour of the K/Mg ratio**

The apparent contradiction between the chemical characteristics of frazil ice and the results of large scale oceanographic profiles suggests that syn- or post-genetic processes affect the characteristics of the frazil ice. In this regard, the behaviour of the K/Mg ratio is worth considering in more detail to assess this.

Figure 8 shows K/Mg -  $\Sigma 4$  (sum of the four major cations in meq  $l^{-1}$ ) diagrams for the different ice types from Hells Gate. Fast ice (Fig. 8a) and congelation ice and platelet ice (Fig. 8b), with  $\Sigma 4 > 10$  meq  $l^{-1}$ , show sea water ratios and thus no significant fractionation. Banded frazil ice (Fig. 8c), with most of  $\Sigma 4 < 10$  meq  $l^{-1}$ ,



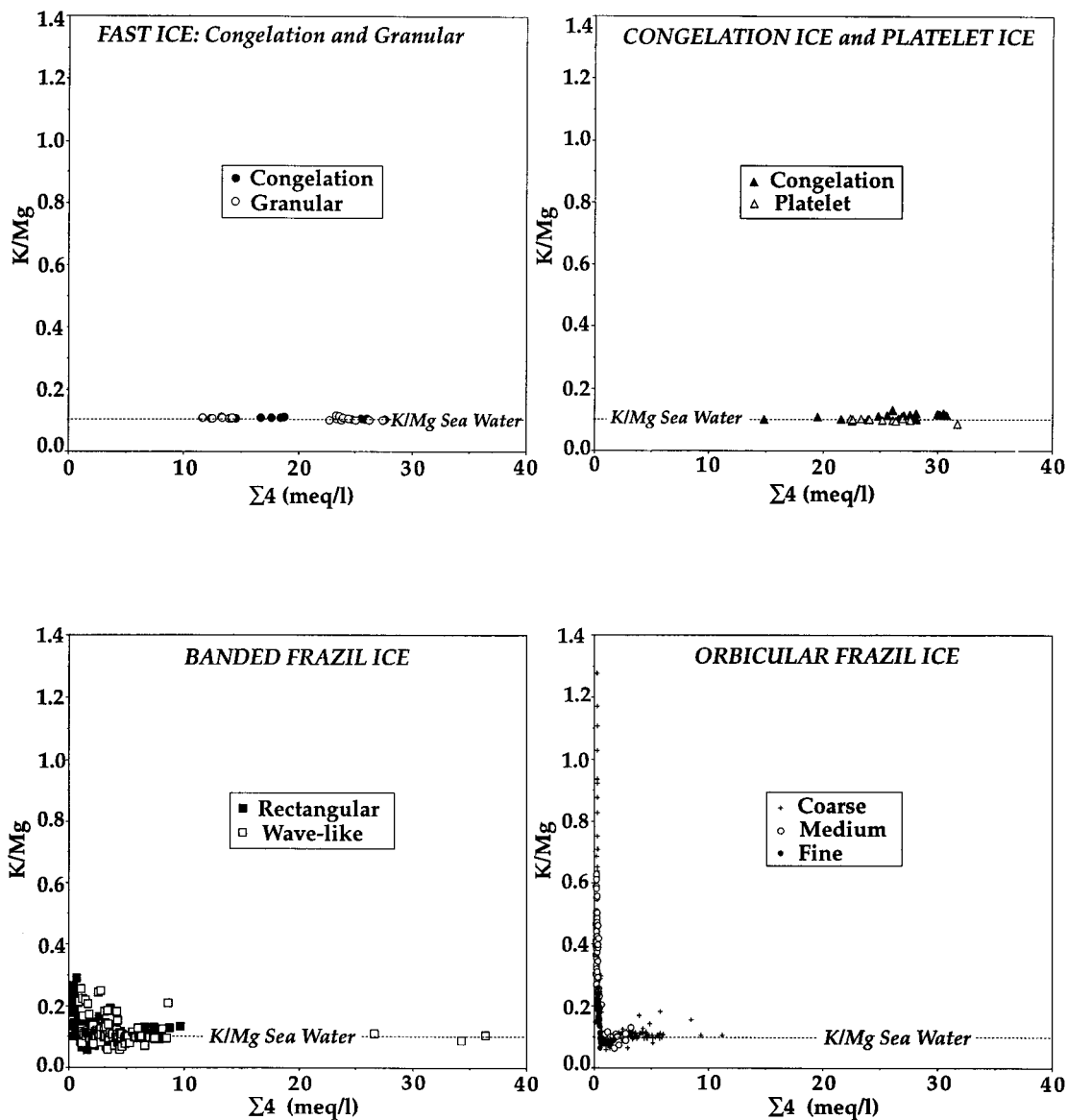


Fig. 8 : Relationship between the K/Mg ratio (calculated in  $\text{meq l}^{-1}$ ) and the sum of the four cations in  $\text{meq l}^{-1}$  ( $\Sigma 4 = [\text{Na}] + [\text{K}] + [\text{Ca}] + [\text{Mg}]$ ) for different ice types from Hells Gate Ice Shelf.

shows a basic population with ratios close to sea water, combined with an increasing proportion of samples with K/Mg values between 0.100 and 0.300, as the total salinity ( $\Sigma 4$ ) decreases. The 45 m long core drilled near the ice shelf front consists almost entirely of banded frazil. It also shows limited chemical fractionation by contrast with a few occurrences of orbicular frazil present at the top of the core. Finally, orbicular frazil (Fig. 8d), with  $\Sigma 4 < 10 \text{ meq l}^{-1}$ , shows the same trend as banded frazil for the "fine" size population. Some of the "medium" and "coarse" size frazil ice show much higher K/Mg values for the low salinity ( $\Sigma 4$ ) samples with the high ratios ( $> 0.300$ ) are attributable to the homogeneous cores (core 18 for the medium frazil and core 23 for the coarse frazil). When orbicular frazil occurs as discrete layers, a few cm thick, in alternation with the banded frazil, it shows higher salinities ( $\Sigma 4$ ) and lower K/Mg ratios. In one of these homogeneous cores (core 23) there seem to be a depth dependency of K/Mg, with higher values of the ratio occurring higher in the core (Fig. 9).

Can such characteristics be understood in terms of the melting events that produce the host water or in terms of the freezing processes that consolidate the frazil? Elements of answers to these questions can be gained from the following two sets of simple experiments :

- Melting fresh-water ice in a sea water reservoir above its freezing point

Four experiments were performed in a cold room with thermostatic equipment controlling the ambient temperature to  $\pm 0.2^\circ\text{C}$ . For each experiment, an insulated Plexiglass cylinder 13 cm high and with an internal diameter of 30 cm was partially filled with natural sea water at a negative temperature above its freezing point. The wall of the cylinder is equipped with a series of sampling holes designed to prevent water losses from the reservoir during sample extraction with narrow syringes and to allow a vertical resolution of about 0.5 cm. A cylindrical ice sample 30 cm in diameter and about 4 cm thick made from distilled water and brought to the same temperature as the sea water was placed in this water and allowed to melt. Prior to this, an inverted channel 2 cm deep had been cut along the diameter of the sample. During the 28 hours from the beginning of the experiment, water sampling was performed at different time intervals. Results from a typical run are given in Table III for a sea water temperature of  $-0.5^\circ\text{C}$  (a value observed in the summer at the level of the base of the HGIS) and an initial salinity of 30.76‰ (calculated from conductivity measurements). The values correspond to four representative time intervals : 30 minutes, 4, 24 and 28 hours. Dilution obviously occurs near the interface and reaches salinity values of about 22‰,

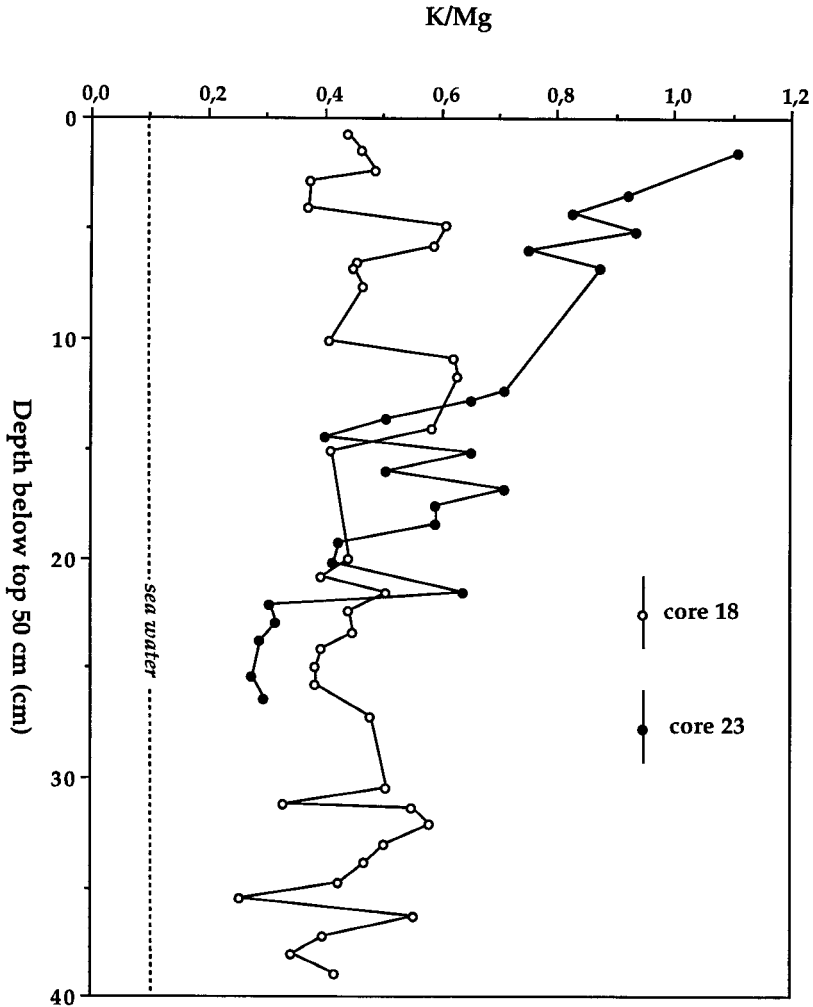


Fig. 9 : Evolution of the K/Mg ratio with depth in two homogeneous ice cores containing only medium-grained frazil (core 18) and coarse-grained frazil (core 23).

Table III : Salinity versus depth at different time intervals in a typical run of melting a fresh-water ice sample in a sea water reservoir above its freezing point

Depth (cm)	0 h 30		4 h 00		24 h 00		28 h 00	
	In or just under the channel	Along a vertical out of the channel	In or just under the channel	Along a vertical out of the channel	In or just under the channel	Along a vertical out of the channel	In or just under the channel	Along a vertical out of the channel
+ 3.45	24.77	-	21.77	-	23.27	-	22.77	-
+ 4.00	Interface position (out of the channel) at the beginning of the experiment							
+ 4.42	28.63	29.76	26.42	27.86	24.91	25.17	25.39	25.77
+ 4.93	30.66	30.06	28.86	28.72	25.77	26.43	26.77	26.99
+ 6.08	30.71	30.76	29.85	30.66	28.38	29.26	28.86	29.76
+ 7.13	30.76	30.76	30.76	30.72	30.76	30.10	30.76	30.32
+ 7.95	-	30.76	30.76	30.76	30.76	30.76	30.76	30.76
+ 8.53	-	30.76	30.76	30.76	30.76	30.76	30.76	30.76



which are comparable to those predicted for the host water of the wave-like banded frazil (Table II). Initially the values show the convergence of diluted waters in the inverted channel cut at the ice-water interface. Later, the dilution front penetrates further down in the reservoir, more rapidly below the inverted channel than under the flat interface and then, given the small size of this experimentally closed system, the effect gradually fades out. Figure 10 shows the evolution of the K/Mg ratio with depth for the same time intervals. In the channel (Fig. 10b) the value increases steadily in the zone affected by dilution, reaching 125% of its initial value in the sea water. This enhancement of the K/Mg ratio is the result of selective diffusion from normal sea water to the melted ice, which favors K enrichment with regards to Mg. The process has previously been demonstrated by Ben-Yaakov (1972) in a specially designed experimental device. Ions from sea water were allowed to diffuse into a dilute solution through a porous glass diaphragm and, after three days, K/Mg ratio could attain more than 200% of its original value in sea water. It is worth noting that, outside the channel in the experiment shown in figure 10a, there is an initial lowering of the K/Mg ratio as diffusion occurs from the flat interface area to the inverted channel. Later on, diffusion from the bottom of the reservoir increases the K/Mg ratio close to the flat interface above the standard sea water value.

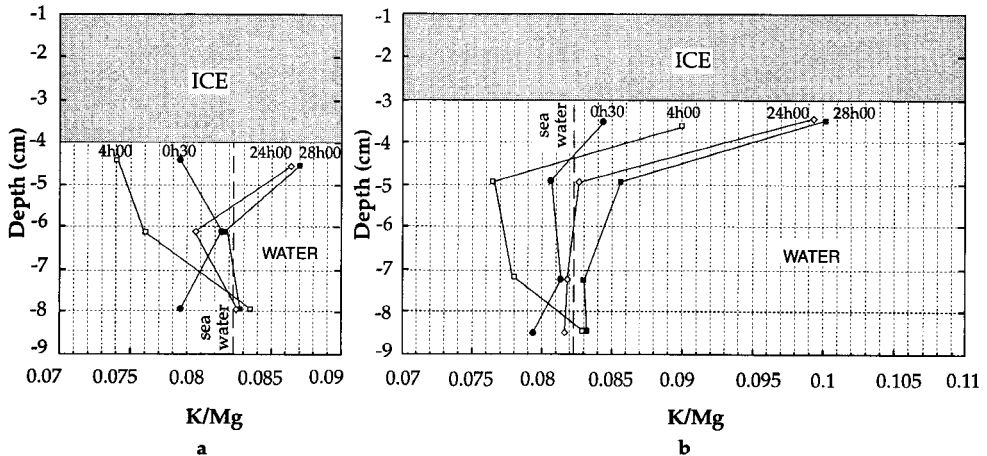


Fig. 10 : Evolution of the K/Mg ratio with depth during the experiment of the melting fresh water "iceberg" floating on sea water (see text for explanation) :

- a. profile out of the inverted channel
- b. profile in and just below the inverted channel

- Freezing of a loose frazil ice matrix

Another set of four experiments were performed, in the same cold room, where individual fresh-water ice crystals were poured to saturation into a sea water reservoir at negative temperature. The mixture was then frozen from top to bottom using a metallic plate, cooled with the aid of ethanol temperature bath. The results of two of these experiments are shown in figures 11a and 11b, respectively, for fine grained (submillimetre sized crystals - porosity 43%) and coarse grained (centimetre sized crystals - porosity 51.6%) artificial frazil. In both experiments, ice crystals, sea water and the cold room were at  $-1^{\circ}\text{C}$ . Global salinities and K/Mg ratios are shown in each diagram. Freezing rates varied between  $2.8 \cdot 10^{-6} \text{ m sec}^{-1}$  and  $0.5 \cdot 10^{-6} \text{ m sec}^{-1}$  for the fine grained experiment and between  $4.2 \cdot 10^{-6} \text{ m sec}^{-1}$  and  $0.7 \cdot 10^{-6} \text{ m sec}^{-1}$  for the coarse grained. Both experiments give similar results. Three zones are clearly seen along the vertical (I =  $0-1 \cdot 10^{-2} \text{ m}$  ; II =  $1-5$  or  $6 \cdot 10^{-2} \text{ m}$  ; III = below  $5$  or  $6 \cdot 10^{-2} \text{ m}$ ). In the top 1 cm, salinity abruptly decreases from values a few ‰ lower than the initial sea water to values between 5‰ and 8‰, depending on the grain size. This is probably the expression of the extremely rapid freezing rate allowing poor cationic expulsion from the solidifying loose ice matrix. The K/Mg ratio falls from values nearly 50% higher than its value in sea water to values slightly lower than those in sea water. The probable explanation for this is the existence of a melting stage when the ice crystals were poured into the sea water, which was about  $0.9^{\circ}\text{C}$  above its freezing point. This would have resulted in selective diffusion of K and Mg from the main part of the reservoir to the top, where less dense water accumulates. Between 1 and 6 cm, salinity stabilizes around 9.5‰ in the fine grained matrix and 6‰ in the coarse grained. It can be seen on figure 11 that, for freezing rates lower than  $2.8 \cdot 10^{-6} \text{ m sec}^{-1}$ , the K/Mg ratio drops slightly below the one of the host sea water. Since the cold wave did not reach depths greater than 6 centimeters at the end of the experiment, the matrix was still rather loose and, therefore, the K/Mg ratio returns to its initial value at the bottom of the reservoir.

These experiments have shown that selective diffusion from normal sea water to fresh meltwater produced at the interface will favour an increase of the K/Mg ratio near this interface. Diluted waters may converge in inverted depressions at the ice-ocean interface. In the case where such irregularities affect the interface, flat undisturbed areas could temporarily show K/Mg ratios lower than standard sea water, providing an alternative explanation to the precipitation sorting effect

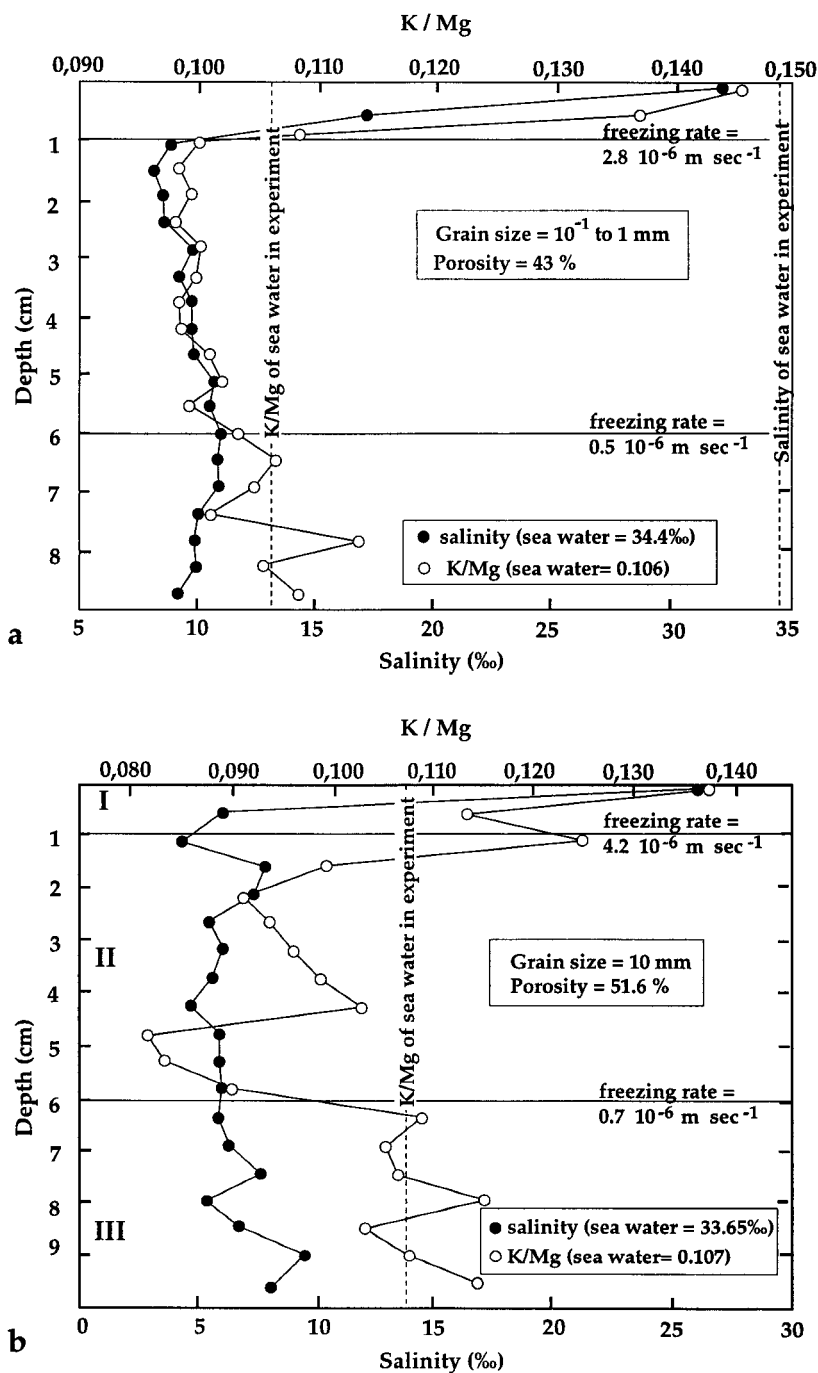


Fig. 11 : Evolution of salinity and K/Mg ratio with depth during a typical experiment of freezing loose artificial frazil from top to bottom (see text for explanation)  
 a. fine-grained frazil      b. coarse-grained frazil

discussed earlier. Experimental observations in a closed system and after periods of a few days, indicate a maximum increase of the ratio of about 200%. On the contrary, freezing of a loose matrix of individual ice crystals in sea water will not favour the increase of the K/Mg ratio and will even lower it slightly for freezing rates below  $2 \cdot 10^{-6} \text{ m sec}^{-1}$ . This probably reflects the progressively overwhelming effect of the faster diffusion of K, from the enriched boundary layer at the interface to the bulk reservoir, as the freezing rate decreases.

### **"Orbicular" versus "Banded" frazil**

Careful examination of Table I demonstrates the obvious textural contrast between orbicular frazil and banded frazil accompanied by a contrast of the ice fabric, debris content and chemistry. It is therefore tempting to see if these characteristics signal different generation and evolution processes.

Banded frazil ice show strong c-axes concentrations in a maximum perpendicular to the crystal elongation, which is subhorizontal in the core. This suggests crystal growth in interface flowing conditions where differential shear favours rotation of the crystals parallel to the local ice-ocean interface. Local vortex structures in the wave-like frazil also suggest a transition from laminar to turbulent flow on some occasions. On isotopic grounds, the host water where the frazil accretes must result from partial dilution of normal sea water by marine ice melt. Souchez et al. (1991) show that percolation of surface meltwater through tide cracks to the underside of the ice shelf (a mechanism invoked by Gow and Epstein, 1972, for the Koettlitz Glacier Tongue in McMurdo Sound, Antarctica) is precluded for HGIS, and they suggest that the source in this case is the melting of congelation ice formed upstream of the zone of influence of descending "warm" (above local freezing point) waters. However, another possibility, compatible with the isotopic results, is that the "source" marine ice for the melt could have been frazil that was also formed upstream of the zone of influence of these warm water plumes. As congelation or frazil ice accumulated at the base of the ice shelf and made its way downstream it would possibly come into contact with sea water above its local freezing point (Souchez et al., 1991). Given the order of magnitude of difference between heat and salt diffusion, meltwater from either congelation or frazil ice itself will form and find its way downstream through (or with) the loose frazil ice matrix, progressively diluting the interstitial sea water. The salinity contrast with the normal sea water at the frazil/ocean interface will set up differential diffusion of K and Mg, raising the K/Mg ratio of this interstitial water. This transformation process of a pre-



existing loose frazil layer will result in considerable inhibition of the mixing by convection between the fresh interstitial water and the normal sea water below, thus allowing the selective diffusion process to occur on a larger time scale. It would also make it easier to understand why no low salinity values were observed by the oceanographers in the free water column. Furthermore, when comparing banded rectangular to banded wave-like frazil, the latter shows stronger c-axis concentration, higher salinities, a lower K/Mg ratio and limited occurrence of vortices. All these observations converge to demonstrate enhanced interface flow conditions resulting in stronger mixing between the loose frazil and the underlying free ocean water.

The c-axes pattern in medium and coarse orbicular frazil is strikingly different from the one of the banded frazil (Table I). The obvious lack of preferential orientation in orbicular frazil suggests an accretion process in calm conditions with no effect of any interfacial flow or/and an increasing effect of recrystallization after deposition, as one would infer from the larger size of the crystals in these frazil ice types compared to other ice types. The case of the fine orbicular frazil in core 4, as shown by the ice fabric is peculiar (Table I). It is, in fact, an intermediate case between the banded and orbicular type, since, at the bottom of the core, the small crystals tend to show a slight elongation along the vertical. It also shows a strong concentration of c-axes as the banded frazil does, but rotated by nearly 90°. The spatial location of core 4 easily explains these features. It is at the fringe of the shear zone where the western and central sector meet. There, ice layers are brought into a sub-vertical position, and initially horizontal layering can be rotated close to the vertical.

When the orbicular frazil a few cm thick occurs sandwiched between two banded frazil layers, the chemical characteristics of the two types of frazil are similar, thereby indicating that these are the expression of the host water, while the texture reflects different interfacial flow conditions. Orbicular frazil is also the only kind of frazil ice from the HGIS that eventually contains particulate matter inclusions. These mainly consist of sponge tests and crustacean faeces, sometimes showing peritrophic membrane, and occasionally echinoderm spicules and worm tubes fragments (G. Houvenaghel, personal communication). One out of 15 samples also contained two diatom fragments. The dominance of fragments of benthic origin indicates the proximity of the sea floor for the waters where the frazil ice formed. It also confirms the efficiency of the scavenging effect of rising frazil ice crystals on suspended matter, as was experimentally demonstrated by Reimnitz et al. (1990). Particulate matter in orbicular frazil ice has also been observed in larger

ice shelves such as the Filchner-Ronne (Oerter et al., 1992) and the Amery ice samples (kindly provided by N.W. Young), especially close to the interface between continental and marine ice.

When the orbicular frazil occurs as medium to coarse grained in thicker homogeneous sequences, it shows minimum salinity values and maximum K/Mg ratios. The shifts in the K/Mg ratio observed in medium and coarse grained orbicular frazil are much higher than those observed experimentally in closed systems. This calls for an open system process, where successive melting events can occur in a strongly individualized frazil ice body. The subglacial topography of the ice shelf provides sheltered inverted depressions where frazil ice will accumulate and remain protected from mixing with ocean waters for a longer period of time. Radio-echo-soundings and aerial photographs both show evidence of such channels or domes, possibly filled with marine ice at HGIS. The central sector of the ice shelf exhibits a transversely undulating interface at a depth between 25 and 50 m, though it is occasionally more shallow than 20 m (Souchez et al., 1991). This reflector is characterized by an energy contrast markedly lower than that found in the western part. Detection of the ice-water interface is thereby inhibited. Nevertheless, if the contrast is one between continental and marine ice, this undulating interface must represent a "fossil" ice-water interface. Lenses of marine ice penetrating into the glacier ice can be considered as the surface expression of the discontinuity observed in radio-echo-sounding profiles. Several processes can be held responsible for the genesis of the inverted channels or domes at the base of the ice shelf: groove-type scarring at the grounding line (Musil, 1989), merging of different floating ice streams with different discharges, folding where a minor ice stream is buttressed by a major one. Thanks to the sheltering role of these inverted channels and domes, and because of the strong mechanical damping effect of the significant thickness of loose frazil ice that accumulate into them, successive inputs of warm ocean water at the frazil/open ocean water interface will repeat the melting events. Enhanced dilution and migration of low salinity waters in the highest parts of the inverted depressions will increase the shifts in the K/Mg ratio. In some cases (Fig. 9 - core 23), the profile of the K/Mg ratio shows decreasing values with depth, suggesting that the chemical sorting is stronger in older frazil, further away from the ice-ocean interface.

Table IV compares the proportion (%) of the different ice types in the cores sampled on a longitudinal transact in the central sector, where the situation is technically less disturbed (cores 21 - 25). Orbicular frazil is typical of the upstream zone of marine ice while the banded frazil is dominant closer to the ice-shelf front.

Results from the textural analyses of the sixty shallow cores retrieved in 1993-94 clearly confirm this special differentiation of the main marine ice types (Lorrain et al., in press). Although dynamic factors might slightly complicate the overall picture, orbicular marine ice is stratigraphically located above banded (rectangular) marine ice (Fig. 12), which results in most of the banded facies outcropping either closer to the ice shelf front or, if further upstream, at the limit of major glacier fluxes. As a further argument, most of the 45 m deep ice core, which is located near the ice shelf front, is made of banded rectangular consolidated frazil. Orbicular frazil is however present, but restricted to limited quantities in the topmost six meters of the core. In the western sector, where the sequence is complicated by shearing and folding, there is evidence that the orbicular frazil was formed further upstream (closer to the grounding line or to the pinning point of Vegetation Island), since it is rich in benthic particulate matter, while banded frazil is devoid of any solid inclusions. This spatial distribution pattern is another favourable factor, increasing the period for diffusion processes in the case of the orbicular frazil.

Table IV : Proportion of the different ice types in the 5 cores of the longitudinal transect in the central sector

ICE CORE	ICE TYPES					
	GLACIER ICE	ORBICULAR FRAZIL			BANDED FRAZIL	
		Fine	Medium	Coarse	Rectangular	Wave-like
21	100%	-	-	-	-	-
22	100%	-	-	-	-	-
23	-	-	-	100%	-	-
24	-	25%	11.5%	7.7%	53.9%	1.9%
25	-	-	-	5.1%	91%	3.9%

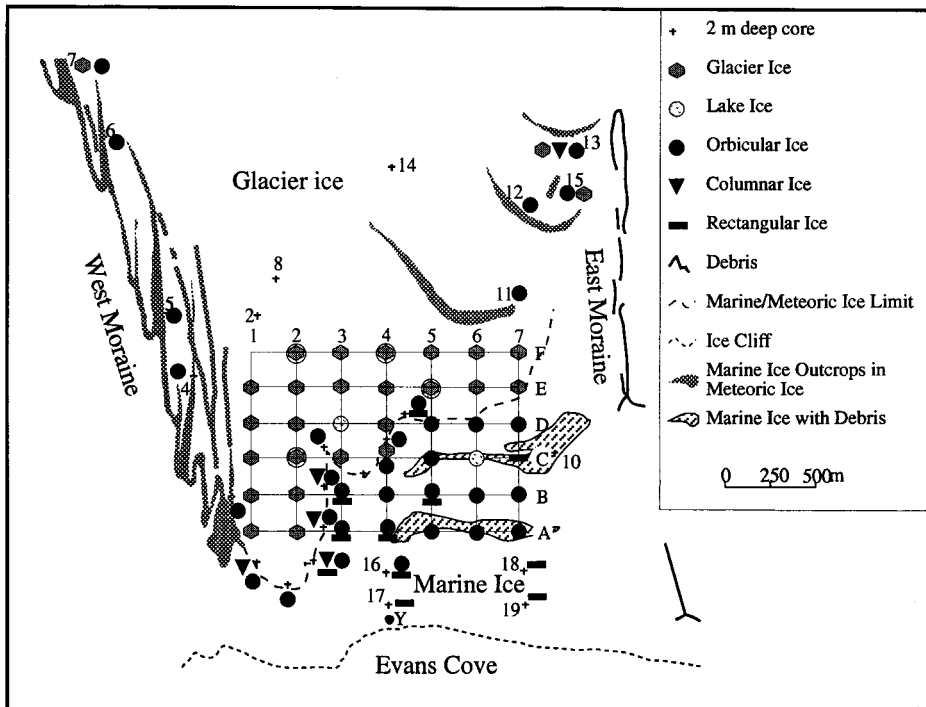


Fig. 12 : Types of ice from sub-surface samples at Hells Gate Ice Shelf

Finally, the results of the melting experiments provide a possible explanation for the minor population of frazil ice showing K/Mg ratios lower than 0.099 (Fig. 8c and 8d) that could represent the freezing-in of loose frazil layers close to the free water interface being submitted to preferential K/Mg depletion.

## Conclusion

Comparison of the textural, isotopic and chemical characteristics of frazil ice at the base of HGIS provide us with new information.

First, medium to coarse grained orbicular frazil accretes upstream in relation to ISW-mode 1 circulation and eventually piles up as thick units in inverted channels or domes where the subglacial topography is favourable. As these frazil ice bodies (or congelation ice) enter the zone of influence of warm oceanic waters, they are subjected to melting. This produces isotopically heavy waters that

progressively dilute the interstitial sea water of the loose frazil, initiating chemical differentiation that is preserved in the frazil matrix. These diluted waters will converge in the highest parts of the inverted depressions, where they are further protected from mixing. Further downstream, the remaining ice will recrystallize resulting in the final crystal sizes and fabrics of medium and coarse grained solid frazil.

Banded frazil ice is formed by another process. It is probably generated by a double-diffusion mechanism at the limit between ISW-mode 1 and ISW-mode 3. This makes the net melting loss due to circulation mode 3 difficult to appraise.

## **GENERAL CONCLUSION**

Global warming is likely to affect Antarctic ice shelves. Small ice shelves with an ice thickness at their front of one hundred meter or less will most probably react more rapidly.

The behaviour of ice shelves is dependent on their boundary conditions. At the ice-ocean interface, a change in these conditions can result either in basal melting or in accretion of marine ice. Melting at the base will tend to destabilize an ice shelf while marine ice accretion will have the opposite effect. An increase in temperature of oceanic water near an ice shelf is not necessarily conducive to basal melting. The conditions required for marine ice formation at the base of ice shelves need to be more thoroughly studied.

The crystallographic, isotopic and chemical properties of marine ice sampled in favourable conditions reveal its origin. Such an approach is followed in two case studies in Terra Nova Bay, Victoria Land.

Results from Campbell Ice Tongue indicate that freezing at or near the grounding line might be more prevalent than previously thought. In Hells Gate Ice Shelf, orbicular frazil ice is accreted upstream in relation to ISW-mode 1 circulation and banded frazil ice is generated by a double-diffusion mechanism at the limit between ISW-mode 1 and ISW-mode 3.

The study of the properties of marine ice is thus a powerful tool to gain a better insight into the problem of ice shelf-ocean interactions.

## ACKNOWLEDGMENTS

The "Programma Nazionale di Ricerche in Antartide" (PNRA) is gratefully acknowledged for having supported the field work at Terra Nova Bay. Thanks are also due to M. Stievenard and J. Jouzel from LMCE, Saclay, for the isotopic analyses. This paper is a contribution to the Belgian Antarctic Programme (Science Policy Office). J.-L. Tison is Research Associate at the National Fund for Scientific Research (Belgium).

## REFERENCES

- Angrisano, G. 1989. Carta batimetrica Mare di Ross-Baia Terra Nova. Istituto Idrografico della Marina, Genova.
- Arnason, B. 1969. Equilibrium constant for the fractionation of deuterium between ice and water. *J. Phys. Chem.* 73 : 3491 - 3494.
- Baroni, C. 1988. The Hells Gate and Backstairs Passage ice shelves (Victoria Land, Antarctica). *Memorie della Società Geologica Italiana* 34 : 103 - 128.
- Baroni, C., Stenni, B. and Lacumin, P. 1991. Oxygen isotopic composition of ice samples from the Hells Gate and Backstairs Passage ice shelves (Victoria Land, Antarctica) : Evidence of bottom freezing. *Memorie della Società Geologica Italiana* 46 : 45 - 48.
- Beck, N. and Munnich, K.O. 1988. Freezing of water : isotopic fractionation. *Chem. Geol.* 70 : 168.
- Ben-Yaakov, S. 1972. Diffusion of sea water ions - I. Diffusion of sea water into a dilute solution. *Geochimica and Cosmochimica Acta* 36 : 1395 - 1406.
- Boldrin, A. and Stocchino, C. 1990. On the hydrological characteristics of Terra Nova Bay. *Oceanographic Campaign 1987-88 Data Report*. University of Genova, Genova : 11 - 57
- Bombosch, A. and Jenkins, A. 1995. Modeling the formation and deposition of frazil ice beneath Filchner-Ronne Ice Shelf. *J. Geophys. Res.* 100 (C4) : 6983 - 6992.
- Bondesan, A., Capra, A., Gubellini, A. and Tison, J.-L. (in press). On the use of static GPS measurements to record the tidal response of a small antarctic ice shelf (Hells Gate Ice Shelf - Victoria Land). *Geog. Fis. Din. Quat.*

- Bromwich, D.H. and Kurtz, D.D. 1984. Katabatic wind forcing of the Terra Nova Bay polynya. *J. Geophys. Res.* 89 (C3) : 3561 - 3572.
- Carmignani, L., Ghezzi, C., Gosso, G., Lombardo, B., Meccheri, A., Montrasio, M., Pertusati, P.C. and Salvini, F. 1987. Geological Map of the area between David and Mariner glaciers, Victoria Land, Antarctica, *Mem. Soc. Geol. It.* : 33.
- Cragin, J.H., Gow, A.J. and Kovacs, A. 1986. Chemical fractionation of brine in the McMurdo Ice Shelf, Antarctica. *J. Glaciol.* 32 : 307 - 313.
- Craig, H. and Gordon, L.I. 1965. Deuterium and oxygen 18 variations in the ocean and marine atmosphere, In: *Proceedings of a Symposium on Marine Chemistry*, Occ. Publ. 3-1965, Schink D. and Corliss J. (Eds.), University of Rhode Island : 277 - 374.
- Crary, A.P. 1966. Mechanism for fjord formation indicated by studies of an ice-covered inlet, *Geol. Soc. Am. Bull.* 77 : 911 - 930.
- Dini, M. and Stenni, B., 1995. Oxygen isotope characterization of Terra Nova Bay seawater (Ross Sea, Antarctica) : submitted.
- Doake, C.S.M. 1976. Thermodynamics of the interaction between ice shelves and the sea. *Polar Record* 18 112 : 37 - 41.
- Goodwin, I.D. 1993. Basal ice accretion and debris entrainment within the coastal ice margin, Law Dome, Antarctica. *J. Glaciol.* 39 : 157 - 166.
- Eicken, H. and Lange, M.A. 1989. Development and properties of sea ice in the coastal regime of the Southeastern Weddell Sea. *J. Geophys. Res.* 94 (C6) : 8193 - 8206;
- Fabiano, M., Povero, P., Catalano, G. and Benedetti, F. 1991. Hydrological data collected during the biological, chemical and geological sampling in Terra Nova Bay. *Nat. Sc. Com., Ocean. Camp. 1989-90, Data Rep.* : 35 - 71.
- Fahrbach, E., Nixdorf, U., Oerter, H. and Rohardt, G. 1994. Tidal induced melting of the Ekström Ice Shelf in the Southeastern Weddell Sea. *F.R.I.S.P. Report N°8, A.W.I.-Bremerhaven* : 48 pp.
- Foldvik, A., Gammelsrod, T., Slotsvik, N. and Torresen, T. 1985. Oceanographic conditions on the Weddell Sea Shelf during the German Antarctic Expedition 1979-1980. *Polar Research* 3 : 209 - 226.
- Frezzotti, M. 1993. Glaciological study in Terra Nova Bay, Antarctica, inferred from remote sensing analysis. *Annals Glaciol.* 17 : 63 - 71.
- Gow, A.J. and Epstein, S. 1972. On the use of stable isotopes to trace the origins of ice in a floating ice tongue. *J. Geophys. Res.* 77 (33) : 6552 - 6557.

- Gow, A.J., Tucker, W.B. and Weeks, W.F. 1987. Physical properties of summer sea ice in the Fram Strait, June-July 1984. CRREL Report : 87 - 16.
- Gross, G.W. 1968. Some effects of trace inorganics on the ice/water system : ch. 3. In Gould, R.F., ed., Trace inorganic in water. American Chemical Society, Advances in Chemistry Series 73, Washington D.C.: 396 pp.
- Gross, G.W., Wong, P.M. and Humes, K. 1977. Concentration dependent solute redistribution at the ice-water phase boundary. III. Spontaneous convection, chloride solutions. *The Journal of Chemical Physics* 67 (11) : 5264 - 5274.
- Hellmer, H.H. and Olbers, D.J. 1989. A two-dimensional model for the thermohaline circulation under an ice shelf. *Antarct. Sci.* 1 (4) : 325 - 336.
- Hellmer, H.H. and Olbers, D.J. 1991. On the thermohaline circulation beneath the Filchner-Ronne ice shelves. *Antarct. Sci.* 3 (4) : 433 - 442.
- Hellmer, H.H. and Jacobs, S.S. 1992. Ocean interactions with the base of Amery Ice Shelf, Antarctica. *J. Geophys. Res.* 97 : 20305 - 20317.
- Jacobs, S.S., Amos, A.F. and Bruckhausen, P.M. 1970. Ross Sea oceanography and Antarctic Bottom Water formation. *Deep Sea Res.* 17 : 935 - 962.
- Jacobs, S.S., Gordon, A.L. and Ardal, J.L. 1979. Circulation and melting beneath the Ross Ice Shelf. *Science* 203 : 439 - 443.
- Jacobs, S.S. and Fairbanks, R.G. 1985. Origin and evolution of water masses near the antarctic and continental margin: evidence from  $H_2^{18}O/H_2^{16}O$  ratios in sea water. In: "Oceanology of the Antarctic Continental Shelf", Jacobs S.S. (Ed), A.G.U., Antarctic Research Series 43 : 59 - 85.
- Jacobs, S.S., Helmer, H.H., Doake, C.S.M., Jenkins, A. and Frolich, R.M. 1992. Melting of ice shelves and the mass balance of Antarctica. *J. Glaciol.* 38 (130) : 375 - 387.
- Jenkins, A. and Doake, C.S.M. 1991. Ice-ocean interaction on Ronne Ice Shelf, Antarctica. *J. Geophys. Res.* 96 : 791 - 813.
- Jenkins, A. and Bombosch, A. 1995. Modeling the effects of frazil ice crystals on the dynamics and thermodynamics of Ice Shelf Water plumes. *J. Geophys. Res.* 100 (C4) : 6967 - 6981.
- Jezek, K.C. and Bentley, C.R. 1983. Field studies of bottom crevasses in the Ross Ice Shelf, Antarctica. *J. Glaciol.* 29 (101) : 118 - 126.
- Jouzel, J. and Souchez, R. 1982. Melting -refreezing at the glacier sole and the isotopic composition of the ice. *J. Glaciol.* 28 (98) : 35 - 42.
- Klepikov, V.V. and Grigor'yev, Yu. A. 1966. Water circulation in the Ross Sea. *A.G.U.* 6 : 52 - 54.



- Lange, M.A. 1988. Basic properties of Antarctic sea ice as revealed by textural analysis of ice cores. *Annals of Glaciology* 10 : 95 - 101.
- Lange, M.A. 1990. Development and physical properties of sea ice in the Weddell Sea, Antarctica. In *Sea Ice Properties and Processes*. CRREL Monograph 90-1 : 22 - 40.
- Lewis, E.L. and Perkin, R.G. 1986. Ice pumps and their rates. *J. Geophys. Res.* 91 : 11.756 - 11.762.
- Lorrain, R., Tison, J.-L., Bondesan, A., Ronveaux, D. and Meneghel, M. (in press) Preliminary results from 60 shallow cores and from one 45-m deep marine ice core at Helles Gate Ice Shelf, Victoria Land, Antarctica. *Terra Antarctica*.
- MacAyeal, D.R. 1984. Thermohaline circulation below the Ross Ice Shelf : a consequence of tidally induced vertical mixing and basal melting. *J. Geophys. Res.* 89 : 597 - 606.
- Meese, D.A. 1989. The chemical and structural properties of sea ice in the Southern Beaufort Sea. CRREL Report : 89-25.
- Meese, D.A. 1990. The chemical and structural properties of sea ice in the Southern Beaufort Sea. In Ackley, S.F. and Weeks, W.F. editors, *Sea ice properties and processes*. CRREL Monograph 90-1 : 32 - 34.
- Musil, G.J. 1989. On the underside scarring of floating ice sheets. *Annals of Glaciology* 12 : 118 - 123.
- Nicholls, K.W., Makinson, K. and Robinson, A.V. 1991. Ocean circulation beneath the Ronne ice shelf. *Nature* 354 : 221 - 223.
- Oerter, H., Eicken, H. and Miller, H. 1991. The physical properties of the marine ice under the Filchner-Ronne-Shelfeis : some preliminary results. In Miller, H. and Oerter, H. eds. *Filchner Ronne Ice Shelf Programme Report n° 5*. Bremerhaven, Alfred Wegener Institute for Polar and Marine Research : 13 - 24.
- Oerter, H., Kipfstuhl, J., Determann, J., Miller, H., Wagenbach, D., Minikin, A. and Graf, W. 1992. Ice-core evidence for basal marine shelf ice in the Filchner-Ronne Ice Shelf. *Nature* 358 : 399 - 401.
- O'Neil, J.R. 1968. Hydrogen and oxygen isotope fractionation between ice and water. *J. Phys. Chem.* 72 : 3683 - 3684.
- Orheim, O. 1986. Glaciological research on Riiser-Larsenisen and nearby ice-shelves in Antarctica, *Norsk Polarinstittut Skrifter* 187 : 5 - 22.
- Orombelli, G., Baroni, C. and Denton, G.H. 1990. Late Cenozoic glacial history of the Terra Nova Bay region, Northern Victoria Land, Antarctica, *Geografia Fisica e Dinamica Quaternaria* 13 : 139 - 163.

- Potter, J.R. and Paren, J.G. 1985. Interaction between ice shelf and ocean in George VI Sound, Antarctica. In: " Oceanology of the Antarctic Continental Shelf ", Jacobs S.S. (Ed.), A.G.U., Antarctic Research Series 43 : 35 - 58.
- Reimnitz, E., Kempema, E.W., Weber, W.S., Clayton, J.R. and Payne, J.R. 1990. Suspended-matter scavenging by rising frazil ice as observed in tank experiments. In Ackley, S.F. and Weeks, W.F. editors, Sea ice properties and processes. CRREL Monograph 90-1 : 97 - 100.
- Richardson, C. 1976. Phase relationships in sea ice as a function of temperature. *J. Glaciol.* 17 : 507 - 519.
- Ronveaux, D 1992. The dynamics of a small antarctic ice shelf as indicated by an ice composition study. Ph.D dissertation, Université Libre de Bruxelles : 391 pp. (Unpublished.)
- Rossi, A. 1991. Preliminary survey of the underground thermal regime in the area around Terra Nova Bay, Victoria Land, Antarctica, *Mem. Soc. Geol. It.* 46 : 457 - 461.
- Souchez, R. and Jouzel, J. 1984. On the isotopic composition in  $\delta D$  and  $\delta^{18}O$  of water and ice during freezing. *J. Glaciol.* 30 (106) : 369 - 372.
- Souchez, R., Lorrain, R., Tison, J.-L. and Jouzel, J. 1988a. Co-isotopic signature of two mechanisms of basal-ice formation in Arctic outlet glaciers. *Ann. Glaciol.* 10 : 163 - 166.
- Souchez, R., Tison, J.-L. and Jouzel, J. 1988b. Deuterium concentration and growth rate of Antarctic first-year sea ice. *Geophys. Res. Lett.* 15 (12) : 1385 - 1388.
- Souchez, R., Lemmens, M., Lorrain, R., Tison, J.-L., Jouzel, J. and Sugden, D. 1990. Influence of hydroxyl-bearing minerals on the isotopic composition of ice from the basal zone of an ice sheet. *Nature* 345 : 244 - 246.
- Souchez, R., Meneghel, M., Tison, J.-L., Lorrain, R., Ronveaux, D., Baroni, C., Lozej, A., Tabacco, I. and Jouzel, J. 1991. Ice composition evidence of marine ice transfer along the bottom of small Antarctic ice shelf. *Geophys. Res. Lett.* 18 (5) : 849 - 852.
- Stocchino, C. and Lusetti, C. 1990. Prime osservazioni sulle caratteristiche idrologiche e dinamiche di Baia Terra Nova (Mare di Ross-Antartide). *Ist. Idr. della Marina, Genova, F.C.* 1132, 55 pp.
- Stocchino, C. 1991a. Mare di Ross - Baia Terra Nova - Carta Batimetrica - 1:50000. Istituto Idrografico della Marina, 2a Edizione - Genova, Febbraio 1991.

- Stocchino, C. and Manzella, G., 1991b. Analisi delle correnti marine di Baia Terra Nova (Mare di Ross-Antartide) CNR, Area della Ricerca di Genova, 56 pp.
- Tison, J.-L. and Haren, J. 1989. Isotopic, chemical and crystallographic characteristics of first-year sea ice from Breid Bay (Princess Ragnhild Coast - Antarctica). *Antarct. Sci.* 1 : 261 - 268.
- Tison, J.-L., Ronveaux, D. and Lorrain, R. 1993. Low salinity frazil ice generation at the base of a small antarctic ice shelf. *Antarct. Sci.* 5 (3) : 309 - 322.
- Tison, J.-L., Bondesan, A., Delisle, G., Lozej, A., Merlanti, F. and Janssens, L. (in press). A dynamical approach to explain ice structures and complex morainic genesis on a partially grounded ice shelf (Hells Gate Ice Shelf - Victoria Land, Antarctica). *Terra Antarctica*.
- Tison, J.-L., Lorrain, R., Bondesan, A., Stiévenard, M., Bouzette, A. and Ronveaux, D., 1995b. Ice shelf water and marine ice production In the frontal zone of Hell's Gate Ice Shelf (Antarctica) : Implications on mass balance -b) the marine ice view : submitted.
- Weeks, W.F. and Ackley, S.F. 1986. The growth, structure and properties of sea ice. In Untersteiner N. ed, *The Geophysics of Sea Ice*, Nato Asi Series, Series B 146 : 9 - 164. Plenum Press, New York.
- Weiss, R.F., Ostlund, H.G. and Craig, H. 1979. Geochemical studies of the Weddell Sea. *Deep Sea Res.* 26 (10A) : 1093 - 1120.
- White, K.D. 1991. Determining the intrinsic permeability of frazil ice - Part 1. Laboratory investigations. CRREL Report 91-23 : 15 pp.
- Worner, G., Viereck, L., Hertogen, J. and Niephaus, H. 1989. The Mount Melbourne volcanic field (Victoria Land, Antarctica) II. Geochemistry and magma genesis, *Geol. Jb.*, Zotikov, I.A. 1986. The thermophysics of glaciers : 275pp., Reidel, Dordrecht.
- Zotikov, I.A., Zagorodnov, V.S. and Raikovsky, J.V. 1980. Core drilling through the Ross Ice Shelf (Antarctica) confirmed basal freezing. *Science* 207 (4438) : 1463 - 1465.
- Zotikov, I.A. 1986. *The thermophysics of glaciers*, 275pp., Reidel, Dordrecht.

